

Utah State University

DigitalCommons@USU

---

All Graduate Theses and Dissertations

Graduate Studies

---

5-1997

## Studies of Mid-Latitude Mesospheric Temperature Variability and Its Relationship to Gravity Waves, Tides, and Planetary Waves

Kenneth C. Beissner  
*Utah State University*

Follow this and additional works at: <https://digitalcommons.usu.edu/etd>



Part of the [Physics Commons](#)

---

### Recommended Citation

Beissner, Kenneth C., "Studies of Mid-Latitude Mesospheric Temperature Variability and Its Relationship to Gravity Waves, Tides, and Planetary Waves" (1997). *All Graduate Theses and Dissertations*. 4687.  
<https://digitalcommons.usu.edu/etd/4687>

This Dissertation is brought to you for free and open access by the Graduate Studies at DigitalCommons@USU. It has been accepted for inclusion in All Graduate Theses and Dissertations by an authorized administrator of DigitalCommons@USU. For more information, please contact [digitalcommons@usu.edu](mailto:digitalcommons@usu.edu).



STUDIES OF MID-LATITUDE MESOSPHERIC TEMPERATURE VARIABILITY  
AND ITS RELATIONSHIP TO GRAVITY WAVES, TIDES, AND PLANETARY WAVES

by

Kenneth C. Beissner

A dissertation submitted in partial fulfillment  
of the requirements for the degree

of

DOCTOR OF PHILOSOPHY

in

Physics

Utah State University  
Logan, Utah

1997

Copyright © Kenneth C. Beissner 1997

All Rights Reserved

## ABSTRACT

Studies of Mid-Latitude Mesospheric Temperature Variability and Its Relationship  
to Gravity Waves, Tides, and Planetary Waves

by

Kenneth C. Beissner, Doctor of Philosophy

Utah State University, 1997

Major Professor: Dr. Vincent B. Wickwar  
Department: Physics

Temperature observations of the middle atmosphere have been carried out from September 1993 through July 1995 using a Rayleigh backscatter lidar located at Utah State University (42°N, 111°W). Data have been analyzed to obtain absolute temperature profiles from 40 to 90 km. Various sources of error were reviewed in order to ensure the quality of the measurements. This included conducting a detailed examination of the data reduction procedure, integration methods, and averaging techniques, eliminating errors of 1–3%. The temperature structure climatology has been compared with several other mid-latitude data sets, including those from the French lidars, the SME spacecraft, the sodium lidars at Ft. Collins and Urbana, the MSISE90 model, and a high-latitude composite set from Andenes, Norway. In general, good agreement occurs at mid-latitudes, but areas of disagreement do exist. Among these, the Utah temperatures are significantly warmer than the MSISE90 temperatures above approximately 80 km, they are lower below 80 km than any of the others in summer, they show major year-to-year variability in the winter profiles, and they differ from the sodium lidar data at the altitudes where the temperature profiles should overlap. Also, comparisons between observations and a physics based global circulation model, the TIME-GCM, were conducted for a mid-latitude site. A photo-chemical model was developed to predict airglow intensity of OH based on output from the TIME-GCM. Many discrepancies between the model and observations were found, including a modeled summer mesopause too high, a stronger summer inversion not normally observed by lidar, a fall-spring asymmetry in the OH winds and lidar temperatures but not reproduced in the

TIME-GCM equinoctial periods, larger winter seasonal wind tide than observed by the FPI, and a failure of the model to reverse the summertime mesospheric jet. It is our conclusion these discrepancies are due to a gravity wave parameterization in the model that is too weak and an increase will effectively align the model calculations with our observations

(186 pages)

## ACKNOWLEDGMENTS

This work was completed with valuable assistance from many people. I would first like to thank Dr. Vincent Wickwar for his help and patience as I tried to sort through the various ideas and tons of data before coming up with the right mix of both. It was a wonderful (most of the time) learning experience. Secondly, I would like to acknowledge my appreciation to the Air Force for providing me with this exceptional opportunity in life.

I also wish to acknowledge the rest of the lidar team at USU: Steve Collins and John Maloney for keeping the lidar running, and Mike Howsden and Ian Monson for their help in processing the OH data. Finally, I would like to thank Jill Marshall for coming to my rescue in the last few days before the defense, and the entire faculty, staff, and numerous graduate students of the USU Physics Department for their help, understanding, and encouragement through this journey I began just a few short years ago.

I would like to thank Pat Espy for taking the time to discuss the intricacies of modeling OH emissions. These talks were invaluable and helped further my understanding of the processes involved. Many thanks to Ray Roble and Ben Foster for making the TIME-GCM output available for my use in this dissertation. It was an essential element of the final product.

And of course, I must express my appreciation to my family for their wonderful support and to Colleen, Gracie, and Bart for their incredible patience and general cheerful presence during these years at Utah State. I realize there were times that they had to sacrifice the good life just so I could get through this successfully. Finally, thanks to my faithful little cat who proofread my manuscript while sitting on my shoulder.

I am looking forward to the next stage.

Kenneth C. Beissner

## CONTENTS

	Page
ABSTRACT .....	iii
ACKNOWLEDGMENTS .....	v
CONTENTS .....	vi
LIST OF TABLES .....	viii
LIST OF FIGURES .....	ix
CHAPTER	
1. INTRODUCTION .....	1
1. Statement of Problem .....	1
2. Background .....	1
3. Summary .....	8
2. MIDDLE ATMOSPHERE .....	11
1. Radiative Processes .....	11
2. Zonal Mean Wind Structure .....	12
3. Theory of Wave Dynamics .....	18
4. Gravity Wave Spectra .....	21
3. ATMOSPHERIC WAVES .....	23
1. Wave Characteristics .....	23
2. Gravity Waves .....	25
3. Planetary Waves .....	30
4. Atmospheric Tides .....	33
4. DERIVING TEMPERATURES FROM A LIDAR .....	39
1. Rayleigh Lidar .....	39
2. Photons to Temperature .....	46
3. Systematic Errors .....	51
4. Statistical Uncertainty .....	64
5. Observations .....	69
5. MESOSPHERIC TEMPERATURE PROFILES .....	70
1. Introduction .....	70
2. Mid-Latitude Comparisons .....	70
3. Summer Comparisons Between 50 and 70 km— Validation or Long-Term Trends .....	74

4. Summer Temperature Fluctuations in the Lower Mesosphere .....	81
5. Relative Minimum Near 75 km in Summer— A Possible Zonal Difference.....	82
6. Low MSISE90 Temperatures Between 80–90 km.....	85
7. Annual Temperature Cycles in the Stratopause and Upper Mesosphere .....	88
8. Variability of the Winter Temperature Profiles .....	91
9. Possible Zonal Differences.....	95
10. High-Latitude Comparison .....	96
11. Summary and Conclusions .....	100
6. COMPARISON OF OBSERVATIONS AND MODEL CALCULATIONS .....	106
1. Introduction.....	106
2. Observations and Data Analysis .....	110
3. Model Calculations of Temperature and Winds .....	113
4. OH Intensity Model .....	114
5. Results .....	123
6. Discussion .....	144
7. Conclusion .....	156
7. SUMMARY .....	159
REFERENCES .....	164



## LIST OF TABLES

Table	Page
1 Rayleigh Lidar Facility .....	42
2 Observation Summary .....	69
3 Monthly Averaged Temperatures Above USU .....	70
4 Geophysical Variability of the Temperatures .....	75
5 Temperature Adjustments for Solar Activity and Long-Term Trends .....	79
6 Comparison of Stratopause Annual Temperature Variations—44 to 49 km .....	90
7 Comparison of Upper Mesospheric Annual Temperature Variations—84 to 85 km .....	90
8 Thermally Averaged Einstein Coefficients $A_{ul}(T)$ .....	119
9 OH( $v$ ) Production/Loss Reaction Rate Constants .....	122

## LIST OF FIGURES

Figure	Page
1 Standard vertical temperature profile of the mid-latitude atmosphere [based on U.S. Standard Atmosphere, 1976].	2
2 Height-latitude cross section of mean zonal temperature (C) for solstice conditions [COSPAR International Reference Atmosphere, Akademie-Verlag, 1972].	13
3 Height-latitude cross section of mean zonal wind ( $\text{ms}^{-1}$ ) for solstice conditions. W and E designate westerly (from the west) and easterly (from the east) direction [COSPAR International Reference Atmosphere, Akademie-Verlag, 1972].	16
4 Schematic showing the approximate altitude profiles of the mean zonal winds for summer and winter. Also shown are the permitted phase speeds for gravity waves propagating into the mesosphere and their estimated breaking levels. [Brasseur and Solomon, 1984].	28
5 A schematic diagram of the USU lidar system.	40
6 Dynamic range of backscattered USU lidar signal. Note the exponential decay of photon counts with height. Initially the chopper is shut and the signal level is low. As the chopper opens, there is a weak Rayleigh signal—weak because the PMT is in low gain. At 30 km, the gain is increased by a factor of 1000, and there is very good signal to approximately 90 km. Between 100 and 450 km is an extended region where we measure the background level.	44
7 The difference in temperature as a function of height for three separate situations. a) A plot of the difference between a temperature profile incorporating a height dependent mean molecular mass and one without, b) the difference when the variation of $m$ is accounted for in the backscatter ratio only, c) the difference when one plot fully incorporates the altitude variation of $m$ in both backscatter and mean mass.	55
8 The difference between two temperature profiles illustrating the pole to equator latitudinal variation of gravity.	58
9 Determination of initial temperature.	61
10 Example of the difference between monthly profile derived from summed photocounts vs. that derived from averaged nightly profiles. While the difference for March is within the signal error at the top of the profile, the profile for August is obviously outside the error.	63
11 Comparisons of monthly-averaged mesospheric temperatures. The USU results are given by a solid curve. The other results are identified in the figure and discussed in the text.	71
12 Temperature comparisons between 50 and 70 km for the period May–August. Refer to the labels in each part of the figure and to the discussion the text.	76
13 Daily temperature variations in summer near the tropopause and lower mesosphere. All-night temperature profiles for seven days from July 1995 between 40 and 65 km, with the data starting at 43 km. An increment of 15 K has been added to each successive curve starting with the second curve from the left.	82

14	The relative temperature minimum between 65 and 78 km in June and July. Two figures showing USU, French, and MSISe90 temperature curves from 60 to 80 km .....	84
15	Daily temperature curves for June and July between 60 and 80 km. Two figures showing USU, French, and MSISe90 temperature curves from 60 to 80 km .....	84
16	The September temperature profile initiated with Ft. Collins temperatures and with MSISe90 temperatures. The results show that the MSISe90 model temperatures are too cold near 85 km at mid-latitudes. ....	88
17	The annual variation in monthly averaged temperatures and the annual averaged temperature for USU. This shows an 18 K variation near the stratopause and a 45 K variation in the upper mesosphere, with a minimum variation near 62 km. At lower altitudes, the temperatures are hotter in summer than in winter. At higher altitudes, they are hotter in winter. ....	89
18	Average temperatures for January 1994 and 1995 and for February 1994 and 1995. The inversion later is at a higher altitude and the variation greater in 1995 than in 1994. ....	94
19	Short-term winter temperature variations—averages from 1–4 and 20–23 January 1995. The variability in 2–3 weeks is comparable to the observed interannual variability .....	95
20	Comparison of mid- and high-latitude temperatures. The high-latitude temperatures are adapted from <i>Lübken and von Zahn</i> [1991]. ....	99
21	Profiles of the species of interest calculated by the TGCM at 7 UT for winter .....	115
22	Temperature profiles for the four seasons. Each season contains three profiles, a 1-month (dashed line) and a 3-month (solid line) average from the USU lidar observations from 40 km to near 90 km, and a reference curve (dotted line) from the TGCM empirical model. All temperature curves portray local midnight conditions (7 UT). ....	124
23	Comparison of TIME-GCM seasonal temperature profiles with profiles from USU lidar, the MSISe90, and NASA-GSFC model. ....	127
24	Nighttime hourly average, winter mean temperature values at six different altitudes between 55–80 km. The three curves: 1-month average, 3-month average, and TGCM values, for a 50 K temperature range. ....	129
25	Nighttime hourly average, summer mean temperature values at six different altitudes between 55–80 km. The three curves: 1-month average, 3-month average, and TGCM values, for a 50 K temperature range. ....	130
26	Nighttime hourly average, fall mean temperature values at six different altitudes between 55–80 km. The three curves: 1-month average, 3-month average, and TGCM values, for a 50 K temperature range. ....	131
27	Nighttime hourly average, spring mean temperature values at six different altitudes between 55–80 km. The three curves: 1-month average, 3-month average, and TGCM values, for a 50 K temperature range. ....	132

28	Time dependence of seasonally averaged meridional and zonal components of winds for each season shown as 1-month average (x's), 3-month average (solid line), and TGCM seasonal mean (dashed). Component winds for each season were extracted from the TGCM at 87 km and compared with the OH hourly-averaged, seasonal-mean meridional and zonal wind components .....	135
29	Comparisons of the hourly-mean, seasonal average OH (6,2) intensities from the FPI and model curves based on the TGCM driven model. The left side y-axis is in units of photons/sec for the FPI data while the right side y-axis is in Rayleighs/m <sup>2</sup> for the model calculations. ....	139
30	Calculated OH (9-6) densities based on the TGCM species concentrations. ....	142
31	Time dependence of seasonally averaged meridional and zonal components of winds for each season shown as 1-month average (x's), 3-month average (solid line), and TGCM seasonal mean (dashed). Component winds for each season were extracted from the TGCM at 92 km and compared with the OH hourly-averaged, seasonal-mean meridional and zonal wind components .....	143

## CHAPTER I

### INTRODUCTION

#### 1. Statement of Problem

The lower atmosphere ( $< 3$  km) is indirectly coupled with the upper atmosphere ( $> 100$  km) through the wind and temperature structure, chemical transport, and the influence of gravity waves, tides, and planetary waves. Originating from tropospheric sources such as convection, wind shears, and flow over topography, these gravity waves propagate upward into the middle atmosphere where they may transfer momentum and dissipate their energy at these higher altitudes. These actions contribute to the momentum and thermal budgets of these altitudes and ultimately lead to a substantial influence on the general circulation of the atmosphere. While the physics that govern the atmosphere are the same throughout, the relative importance of the many processes varies from region to region. As a result, the atmospheric state varies significantly with altitude as well as from place to place and time to time.

The coupled nature of the atmosphere is further demonstrated by the interdependence between the composition, dynamics, and energetics among the layers. As the waves and tides influence the temperature and circulation, the winds and temperatures affect the composition through chemical reaction rates that are strongly temperature dependent and the variability of the atmospheric density, especially with regard to three-body reactions. An awareness of the temperature structure of this region is essential for development of self-consistent atmospheric models. Such models are potentially important tools for understanding how the joint action of thermal and mechanical forcing produces the temperature and wind structure observed in the mesosphere.

#### 2. Background

Fundamentally, the atmosphere may be divided vertically into layers or "spheres" defined according to their thermal characteristics. Upward from the surface these layers are the *troposphere*, *stratosphere*, *mesosphere*, and *thermosphere* as represented in Figure 1. The upper boundaries, or

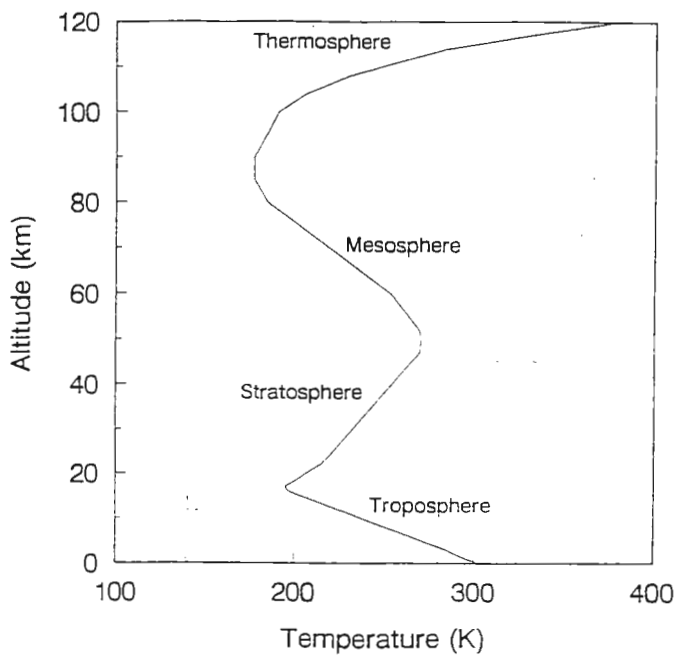


**Figure 1.** Standard vertical temperature profile of the mid-latitude atmosphere [based on U.S. Standard Atmosphere, 1976].

transition zones, of each of these layers are the tropopause, stratopause, mesopause, and thermopause, respectively. The troposphere is the lowest layer and is characterized by a mean temperature lapse rate of 6 K/km resulting from radiative and adiabatic cooling effects of the earth-air interface via small-scale convection. Above the tropopause is the stratosphere where absorption of ultra-violet (UV) solar radiation by ozone causes the temperature to increase with altitude up to the top of the layer, near 50 km. Above the stratopause, in the mesosphere, the temperature generally decreases with increasing altitude, due to a decrease in the ozone heating rate balanced by radiative cooling, primarily from  $\text{CO}_2$ . Indeed, this defines the mesosphere as a distinct region, since in both adjoining regions (the stratosphere and the thermosphere) the temperature increases with altitude. At the mesopause, temperatures drop to the lowest values in the atmosphere reaching 130–150 K at 85–90 km in the polar region. Beyond the mesopause, in the thermosphere, the kinetic temperature increases rapidly as collisions between molecules decrease with altitude reaching a near-constant exospheric temperature at an altitude of several hundred kilometers.

Turbulent mixing or eddy diffusion keeps the atmospheric constituents well mixed below ~100 km so that the mean molecular weight varies little with height. Above 110 km, molecular diffusion is more effective than eddy diffusion and the mean molecular weight of the region varies considerably with altitude as atmospheric constituents separate according to their respective masses. At this altitude, the density of atomic oxygen increases at the expense of  $\text{O}_2$  as a result of photo-dissociation.

The term "middle atmosphere" refers to the collective region bounded by the thermosphere above and the troposphere below. Sometimes referred to as the "ignorosphere," the middle atmosphere is not as well understood as the other regions of the atmosphere for a couple of reasons: lack of attention and lack of adequate coverage by available observational techniques.

Lacking the wide attention given the troposphere, ionosphere, and thermosphere, the middle atmosphere has not been studied as extensively in the past as these other regions. The troposphere has always been of interest in that the bulk of the atmospheric mass and water vapor lies there. The presence of water vapor, together with the thermo- and hydrodynamic processes occurring in this region, produce what we think of as weather. The ionosphere, so called due to the large number of ions in the region, is a

key region influencing radio frequency (RF) propagation, and the thermosphere has a major influence on the ionosphere and on satellites orbiting within this region via the drag induced by the density of the region. The middle atmosphere went largely unnoticed prior to the 50's and 60's. However, only in the last few decades has interest in the middle atmosphere increased, initiated primarily due to the global change problem and fears that we may be adversely affecting the ozone layer [Andrews *et al.*, 1987].

As atmospheric models became more sophisticated due to the incorporation of more complex chemical and dynamical processes, the void in the middle atmospheric regions was often filled by interpolation and extrapolation using the small amount of data available. This created a limiting factor in modeling efforts. As the studies continued, the effect of gravity wave activity throughout the region became apparent [Hines, 1960]. Gravity waves were found to have a unique affect on this region through their ability to generate turbulence [Hodges, 1967] and transport momentum between layers [Jones and Houghton, 1971]. The interaction of these waves with the mean background wind flow and with other waves results in an exchange of energy and momentum between altitudes. This interaction subsequently affects not only the energy balance in this region, but also the density, temperature, and wind structure. Today, the middle atmosphere's temperature, composition, and dynamics are considered to be significantly influenced and altered by gravity waves due to their ability to transport energy and momentum into the region from lower altitudes, and, when dissipated, to accelerate the mean flow [Bretherton, 1969, Jones and Houghton, 1971]. Gravity waves are believed to play a large role in the interdependence of the troposphere, the middle atmosphere, and the lower thermosphere via wave propagation, interaction with the mean flow, and dissipation within the stratosphere and mesosphere [Houghton, 1978; Lindzen, 1981; Matsuno, 1982; Holton, 1982, 1983; Garcia and Solomon, 1985]. The acknowledgment of the complex photochemical and dynamic interactions has increased the need for observations in this region.

However, the middle atmosphere has historically been a difficult area in which to conduct long-term global scale observations and collect reliable data with temporal and spatial resolution sufficient to properly study phenomena other than the largest scale events. The lower atmosphere has been



continuously studied over many years through meteorological programs, but systematic study of the middle atmosphere has only been conducted for the past 20–25 years. Therefore, while a fairly large body of theory exists on the middle atmosphere and limited observations have been useful in defining the large-scale wind and temperature structure, generally it is poorly known observationally and remains a data sparse region. Understanding the dynamics and chemistry of the middle atmosphere regions requires that observations of the state variables (temperature, density, winds, and composition) be made over extended periods of time. While other regions of the atmosphere are more accessible to observation, the middle atmosphere is notoriously inaccessible to in situ measurements, so most studies have come from remote sensing techniques. Any attempt at a definitive study of the middle atmosphere requires an accurate and continuous set of observations covering the full altitude range with measurement resolution within the time and length scale of the smallest phenomena being observed. The sampling rate must be adequate to resolve the temporal variation of atmospheric processes such as the seasonal and diurnal cycles, the multi-day propagation of planetary waves, and the variable activity of gravity waves from their intrinsic periods (a few minutes) to many hours. This suggests a profile extending up to at least 80 km and time and space scales on the order of tens of minutes and hundreds of meters, respectively, for any study at gravity wave scales.

Some of the earliest measurements of geophysical phenomena of the middle atmosphere used balloons which could ascend to 30 km. While balloon observations still occur on a regular basis, the limitations imposed by their poor temporal resolution and altitude restrictions are substantial. Aircraft provide excellent spatial and temporal resolution, but sample only along the flight track, and cannot sample high altitudes above 30 km.

With the development of rocket technology during the past 50 years, the use of rocketsondes, Pitot static tubes, rocket-launched falling spheres [Philbrick *et al.*, 1985], and measurements of acoustic signals from grenades [Theon *et al.*, 1972] gives scientists the ability to investigate density and temperature profiles up to 90 km. Rocketsondes provide good vertical profiles below 60 km but accuracy problems arise at higher altitudes due to their high speed [Hauchecorne *et al.*, 1991]. Although evidence

of gravity wave effects have been observed by these techniques. sampling occurs only at selected times and at a very few locations providing only a "snapshot" profile with sparse geographical and temporal coverage, creating a serious analysis problem in any effort to study systematically the temporal dynamics of the relevant atmospheric processes.

Environmental satellites are uniquely capable of providing a global view of the temperature field. Middle atmospheric temperatures have been measured by both infrared (IR) nadir sounders and limb scanning spectrometers, e.g., the Stratospheric Sounding Unit, on-board NOAA satellites, and microwave imaging, e.g., UARS. Observations of middle atmospheric temperatures obtained by *Barnett and Corney* [1985a] from Nimbus 6 satellite's nadir viewing pressure modulated radiometer (PMR) were used as the base of the CIRA 86 atmospheric model, providing latitudinal, longitudinal, and seasonal variations of the temperature up to 65 km. This climatology has been complemented with the Solar Mesospheric Explorer (SME) global observations of the UV limb radiance [*Clancy and Rusch*, 1989; *Clancy et al.*, 1994]. As useful as they are, satellite radiometers need periodic calibrations by ground measurements and observations are impeded with low horizontal and vertical resolutions and a viewing window that limits the local time of the observation.

Radar became more popular in view of its greater temporal and spatial resolution, but radars have their own limitations. Early incoherent scatter radars were not powerful or sensitive enough to provide useful data much below the thermosphere. Other radar methods are capable of monitoring the velocity field over a comparatively limited range of heights, e.g., 1–30 for stratosphere-troposphere (ST) radar and 60/80–110 km for MF (daytime/nighttime) radar [*Meek et al.*, 1985; *Vincent and Fritts*, 1987; *Manson and Meek*, 1988; *Reid and Vincent*, 1987] and 80–100 km for the meteor wind radar (MWR) method [*Avery*, 1990]. A blind spot remains for the 30–60 km region.

None of these techniques are capable of providing high-resolution, accurate density and temperature measurements needed for detailed studies of climatological atmospheric fluctuations. Thus there still exists a significant lack of observational data over the entire altitude range to provide detailed information on wave characteristics or origins.

With Raleigh lidar, the ability to measure vertical soundings of middle atmospheric molecular density from Rayleigh scattering of a laser makes it possible to determine an absolute temperature profile of the middle and upper stratosphere, and of the mesosphere, in a region inaccessible to existing radar techniques and balloon platforms. Numerous experiments using laser-based measurements of Rayleigh backscattered radiation have been used to measure atmospheric densities and temperatures. The Rayleigh-scatter lidar technique is capable of deriving temperature profiles with a good vertical resolution from 10 km to almost 100 km [e.g., *Hauchecorne and Chanin*, 1980; *Chanin and Hauchecorne*, 1981; *Shibata et al.*, 1986; *Jenkins et al.*, 1987; *Mitchell et al.*, 1991; *Wilson et al.*, 1991; *Hauchecorne et al.*, 1991; *Keckhut et al.*, 1993; *Meriwether et al.*, 1994; *Whiteway et al.*, 1995; *Wickwar et al.*, 1997a; this work], which frequently compare favorably with those found by other techniques [*Lübken and von Zahn*, 1991; *Keckhut et al.*, 1993; *Ferrare et al.*, 1995].

As the technology of the Rayleigh backscatter lidar technique evolves, its capability increases. Larger telescopes have enabled the maximum altitude to be pushed from near 80 km to near 100 km [*Meriwether et al.*, 1994] and downward from 30 km into the region of Mie scattering and absorption by observing vibrational Raman scattering [*Keckhut et al.*, 1990] from  $N_2$  and rotational Raman scattering from  $N_2$  [*Nedeljkovic et al.*, 1993; *Chanin et al.*, 1994]. Lidar observations have been extended into the daytime [*Gille et al.*, 1991]. Observations of the Doppler shift of the backscattered spectrum have enabled scientists to deduce the neutral winds, even in the hole in the MST radar altitude coverage between 30 km and 65 km [*Chanin et al.*, 1989a; *Tepley et al.*, 1991; *Tepley*, 1994; *Chanin et al.*, 1994; *Rees et al.*, 1997].

With the capability of resolving temporal and spatial atmospheric fluctuations continuously within the 30–90 km altitude range, the application of lidar has become increasingly useful in the study of atmospheric dynamics, allowing observation of geophysical phenomena such as atmospheric gravity waves [*Gardner et al.*, 1989; *Mitchell et al.*, 1991; *Adriani et al.*, 1991; *Wilson et al.*, 1991; *Meriwether et al.*, 1994; *Whiteway et al.*, 1995], tidal variations [*Gille et al.*, 1991], stratospheric warmings and planetary waves [*Hauchecorne and Chanin*, 1982, 1983], mesospheric inversions [*Hauchecorne et al.*,

1987; *Whiteway et al.*, 1995], the oscillation of the 27-day solar cycle [*Keckhut and Chanin*, 1992], climatology [*Chanin et al.*, 1985, 1990; *Hauchecorne et al.*, 1991; *Keckhut et al.*, 1993], the quasi-biennial oscillation (QBO) [*Chanin et al.*, 1989b], and the influence of the 11-year solar cycle [*Chanin et al.*, 1987; *Keckhut and Chanin*, 1989].

The middle atmosphere contains some of the more interesting chemistry and dynamics of the atmosphere. For instance, the middle atmosphere is the region where the ozone layer exists, absorbing solar ultraviolet radiation that is potentially harmful to life on earth, and the region where chemical species may exhibit properties not found in other altitude regions, e.g., airglow from hydroxyl radicals (OH). The effect of ionization reaches into the upper middle atmosphere and the metallic layer near 80–100 km contains numerous metallic neutrals and ions produced from the breakup of extraterrestrial meteors. While the polar mesopause receives its greatest amount of solar radiation in summertime, it is the coldest region of the atmosphere in the summer contradictory to radiative balance. Similarly, there exists a stratopause at the winter pole even though no solar radiation is received.

The goal in examining the variability of the temperature structure is to gain information on the interactions taking place in the middle atmosphere. The accuracy of these measurements is a fundamental quality that allows the study of atmospheric temperature trends (long and short term) and the collection of data to form a reference database in this relatively unexplored region of the atmosphere. Through Rayleigh lidar observations we hope to gain a better understanding of the mesospheric temperature structure, its fluctuations, and the dynamics of the region including atmospheric wave phenomena and their effect on the mesospheric circulation. This knowledge will provide the groundwork for future dynamic, physical, and chemical atmospheric modeling activities.

### 3. Summary

The objectives of this dissertation are:

- 1) Determine the absolute temperature profile as derived from lidar measurements. This includes a detailed analysis of possible systematic errors in the temperature calculations such as the altitude/latitude variability of the "gravitational constant," the variation of the mean molecular mass above

85 km and its effect on the Rayleigh backscatter ratio, the presumed initial temperature value at the top of the profiles, and evaluation of the background signal.

2) Evaluate the middle atmospheric temperature climatology for the mid-latitudes. Compare profiles collected over Logan, UT, with those obtained at mid-latitudes from other groups using a variety of sources (e.g., models, lidars, satellites, etc.) in order to distinguish similarities and differences in locations and methods.

3) Examine the temperature structure to find an explanation for variations. Identify the existence and nature of wave and tidal propagation through the upper stratosphere and into the mesosphere as observed in temperature profiles. This includes distinguishing tidal and wave effects via temperature variability on time scales from hourly, to nightly, monthly, seasonally, and annually.

4) Compare seasonal observations of several parameters with those produced by a global circulation model (i.e., TIME-GCM). These parameters include temperatures from the USU lidar and mesopause winds and OH airglow intensity observations from the Fabry-Perot interferometer at Bear Lake Observatory (BLO). A photochemical model is developed and used to simulate OH emission intensities using the constituent profiles of the TIME-GCM. Comparing co-located temperatures, winds, and OH intensities, simultaneously, allows us to study the effect of gravity waves and tides on both the dynamical structure and the chemical composition of the mesosphere.

5) Compare the dynamical structure of the middle atmosphere to the dynamical structure of the troposphere. A major feature of the middle atmosphere is the intermediate layer (an anomalous temperature inversion), the cause of which is still in question. A connection between the troposphere and the middle atmosphere is expected to result from planetary wave activity propagating through the stratosphere. Planetary waves activity may correlate to changes in the winter temperature inversion.

This dissertation is organized with a review of the radiative and dynamical processes of the region in Chapter 2. Wave theory is described in Chapter 3 where we are primarily concerned with gravity and planetary waves and solar tides. Chapter 4 provides a detailed description of the USU lidar system. It includes a description of the measurement and data analysis techniques with a detailed

description of possible systematic errors in the temperature calculations. Results of the 2-year lidar climatology study are presented in Chapter 5. Chapter 6 describes the development of the OH emission model and compares observations to theory using FPI and lidar data and the TIME-GCM calculations. Conclusions are presented in Chapter 7.

## CHAPTER 2

### MIDDLE ATMOSPHERE

#### 1. Radiative Processes

Fundamentally, atmospheric dynamics and circulations are driven by differential solar heating and gravity resulting in pressure gradients. The lower atmosphere is in continual motion in response to these pressure gradients. More specifically, the resulting wind and thermal structure is a product of the balance between heat production, heat loss, and the resulting heat transport due to atmospheric motions.

Radiative heating in the middle and upper atmosphere is dominated by absorption of solar UV and extreme UV (EUV) radiation by the various constituents, in contrast to the troposphere where re-radiated infrared (IR) is most significant although some absorption by water vapor occurs. The temperature maximum at the stratopause (40–50 km) results from absorption of solar radiation at 200–300 nm by ozone ( $O_3$ ). Molecular oxygen ( $O_2$ ) adds a small amount of heat near 80–120 km as radiation absorbed in the Schumann-Runge bands dissociates the molecule to form atomic oxygen (O) in the thermosphere. This energy is transported via eddy diffusion of O downward to the upper mesosphere where the energy is then released through recombination. While the heat input may be small, the rise in temperature can be considerable due to the low density at these altitudes. The response of the middle atmosphere to variations in solar irradiance (e.g., the seasonal variation, the 11-year solar cycle, and the 27-day solar period) will also affect the temperature structure.

Radiative heat loss is attributed to Newtonian cooling or molecular IR emission. Wien's displacement law suggests emissions would be in the wavelength range of 15–9.7  $\mu\text{m}$  for a mesospheric temperature of 200–300 K. Atmospheric species which contain efficient rotational and/or vibrational energies in this IR region include  $CO_2$ ,  $H_2O$ , and  $O_3$ . In the stratosphere and lower mesosphere the thermal structure is in radiative equilibrium and is accounted for by a balance between these emission and absorption processes.

Heat transport via conduction and convection allows heating and cooling between levels. Molecular conduction of heat downward from the thermosphere into the mesosphere creates a major loss

of heat for the thermosphere but only a minor source for the mesosphere. Eddy diffusion or convection is more efficient than conduction below the turbopause ( $\sim 110$  km) and plays a larger role in the energy balance of the mesosphere. Although the atmosphere is generally considered to be in radiative equilibrium in the stratosphere, this is not true in the upper mesosphere and mesopause where the dynamics of large-scale winds significantly alter the local heat balance. These winds not only affect the horizontal distribution of sensible heat throughout the atmosphere, but also lead to the redistribution of heat, which occurs when an ionized or dissociated species created in one place recombines in another. The relationship of chemical composition with the radiative budget illustrates the importance of transport mechanisms in the upper mesosphere. Dissipation and turbulent energy of wave disturbances propagating upward from the lower atmosphere and exothermic chemical reactions also contribute to the temperature structure of the middle atmosphere.

In addition to a vertical temperature structure, the seasonal variance of insolation leads to strong meridional gradients of atmospheric temperature. Maximum heating at mid to high summer latitudes and maximum cooling at mid to high winter latitudes translates to the expected high summer temperatures and low winter temperatures in the troposphere and stratosphere. Figure 2 shows the zonally averaged temperature field in which a temperature maximum in excess of 290 K occurs at the high latitude summer stratopause (55 km), consistent with maximum solar ozone heating while cooler temperatures of about 240 K are found at the high latitude winter stratopause where solar heating is absent.

## 2. Zonal Mean Wind Structure

### 2.1. Thermal Wind

The theory of thermal wind demonstrates the close relationship between thermodynamic conditions and advective motions. To show this, we start with the momentum equation [Holton, 1979]:



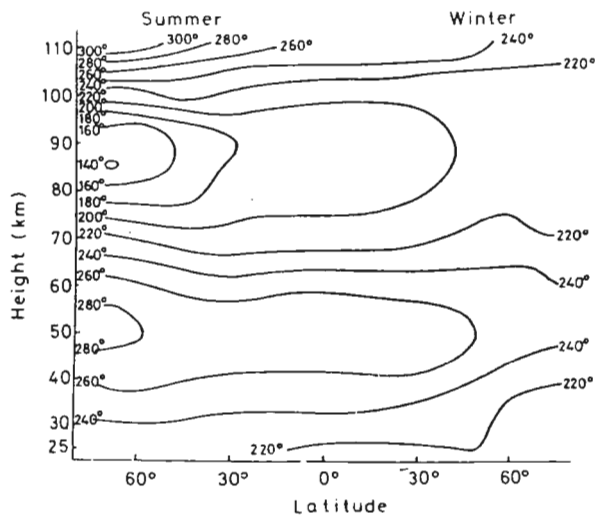


Figure 2. Height-latitude cross section of mean zonal temperature (C) for solstice conditions [CIRA, 1972].

$$\frac{\partial \vec{U}}{\partial t} + (\vec{U} \cdot \nabla) \vec{U} + 2(\vec{\Omega} \times \vec{U}) = -\frac{1}{\rho} \cdot \nabla p + \vec{g} + \vec{F} \quad (1)$$

where  $\vec{U}$  is the vector wind speed,  $\vec{\Omega}$  the Earth's angular momentum,  $p$  pressure,  $\rho$  the density,  $\vec{g}$  the acceleration due to gravity, and  $\vec{F}$  the acceleration due to frictional forces that may be acting (e.g., viscosity). The terms represent forces per unit mass, acting on a parcel, and include the Coriolis force ( $2\vec{\Omega} \times \vec{U}$ ), the pressure gradient force ( $-\frac{1}{\rho} \cdot \nabla p$ ), and the gravitational ( $\vec{g}$ ) and frictional ( $\vec{F}$ ) forces.

Separating the momentum equation into its components and retaining only the dominant terms for a large-scale quasi-horizontal frictionless flow results in the horizontal geostrophic momentum equations, representing the balance between the Coriolis force and pressure gradient. The geostrophic momentum equations characterize the dynamic structure of the middle atmosphere:

$$f u = -\frac{1}{\rho} \frac{\partial p}{\partial y} \quad (2)$$

$$f v = \frac{1}{\rho} \frac{\partial p}{\partial x} \quad (3)$$

where  $f (= 2\Omega \sin \theta)$  is the Coriolis parameter,  $u$  (an east wind is towards the east in the positive  $x$  direction) and  $v$  (a north wind is towards the north in a positive  $y$  direction) are the zonal and meridional winds, respectively. The vertical component is the hydrostatic equation representing the balance between the vertical pressure gradient and gravity.

$$\frac{\partial p}{\partial z} = -\rho g \quad (4)$$

Combining the vertical gradient (differentiating with respect to  $z$ ) of the geostrophic wind together with hydrostatics and the ideal gas law leads to the thermal wind equations

$$f \frac{\partial u}{\partial z} = -\frac{g}{T} \left( \frac{\partial T}{\partial y} \right) \quad (5)$$

$$f \frac{\partial v}{\partial z} = \frac{g}{T} \left( \frac{\partial T}{\partial x} \right) \quad (6)$$

The thermal wind equation illustrates that the vertical shear of horizontal wind is proportional to the poleward and zonal temperature gradients, whereby a winter to summer temperature gradient gives

rise to a westward wind that increases with height in the summer hemisphere and an eastward wind that increases with altitude in the winter hemisphere. The thermal wind is often used in atmospheric models to obtain the mean zonal wind distribution from the temperature field [Garcia and Solomon, 1985].

This is the situation observed in the stratopause and mesopause as shown in Figure 3. Near 65 km the flow is easterly (toward the west) in summer latitudes. Moving up in altitude, the flow reverses and becomes strong westerly at 105 km. Similarly, the temperature gradient is equatorward in the altitude range of 75–100 km. From the viewpoint of the thermal wind, the zonal wind system is consistent with the meridional temperature distribution as observed.

However, determination of the meridional wind fails when using the thermal wind relationship since  $v$  is considered constant and independent of altitude, and thus any longitudinal variation of temperature is ignored in the mean zonal temperature. The result is inconsistent with observations, suggesting that a north-south flow is controlled by mechanisms we neglected.

## 2.2. Diabatic Circulation

The zonal winds are approximately in balance with the meridional temperature distribution, thus obeying the thermal wind equation and indicating that for a winter to summer temperature increase, the summer easterlies (toward the west) should increase with height. The same types of arguments and balances apply to equinox conditions when the maximum net heating occurs in the equatorial region, the temperature decreases away from the equator, and the zonal winds are westerly (i.e., towards the east) in both hemispheres.

Calculations [Geller, 1983] and observations indicate an opposite tendency above 70 km where the latitudinal temperature gradient reverses and the temperature increase is from the summer to the winter hemisphere, contrary to the direction predicted by radiative equilibrium [Murgatroyd, 1969]. Here the mesopause is warmer in winter than summer [Stroud et al., 1959; Theon and Smith, 1970; von Zahn and Meyer, 1989; Lübken and von Zahn, 1991]. Evidence of this departure from radiative equilibrium in the mesosphere is available from temperature measurements using in situ and remote sensing techniques [von Zahn and Meyer, 1989; Clancy and Rusch, 1989; Hauchecorne et al., 1991; She et al., 1993; this

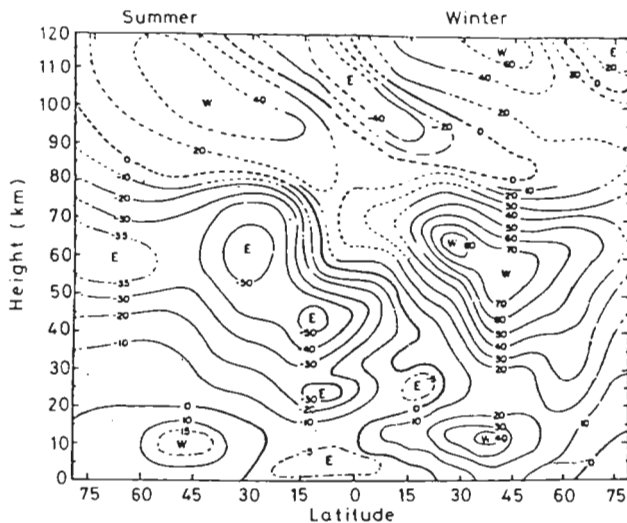


**Figure 3.** Height-latitude cross section of mean zonal wind ( $\text{ms}^{-1}$ ) for solstice conditions. W and E designate westerly (from the west) and easterly (from the east) direction [CIRA, 1972].

dissertation]. As such, the key issue in the last two decades has been to understand why the circulation and temperature structure of the mesosphere is more complex than that predicted by simple radiative forcing alone.

As it turns out, vertical motions in the mesopause drive the reversal of meridional temperature gradients. Consider a classical convection model where stratospheric solar heating in the summer hemisphere and radiational cooling in the winter hemisphere set up a pressure gradient that drives a summer to winter meridional circulation with cross-equatorial flow. The meridional air flow follows that of a convective cell where a hot, light air mass rises and a cold, heavy air mass sinks. This diabatic circulation governs the upper mesospheric temperatures near 80–90 km via adiabatic cooling due to expansion by rising motions near the summer pole and adiabatic heating due to compression by sinking motion near the winter pole. These vertical motions lead to significant departures from radiative equilibrium for the polar mesopause.

Theoretically, Coriolis torques acting on this transverse motion from the summer to winter mesosphere should translate to very strong zonal (east/west) accelerations. Yet despite this tendency to accelerate the mean flow, observed zonal winds decrease with height above 70 km, consistent with the thermal wind balance relationship. The strength of the observed mean meridional circulation depends significantly on a momentum sink (or source) needed to counterbalance the Coriolis force produced by parcels moving in the meridional direction, decelerate the mean zonal wind, and reverse its vertical gradient. A transfer of momentum into the mesosphere region was required in order to obtain agreement between the momentum equation and the observed departures from radiative equilibrium.

Early atmospheric models required the inclusion of a Rayleigh friction or "wave drag" term in the general circulation equations as a constraint on the mean zonal wind in the upper mesosphere [Leovy, 1964; Schoeberl and Strobel, 1978; Holton and Wehrbein, 1980] in order to achieve a reversal of the mean zonal wind gradient which must accompany the mean meridional temperature gradient reversal near the mesopause. These efforts improved calculated wind and temperature fields yielding qualitative agreement with observations [Geller, 1983]. However, a wave drag simply proportional to the mean wind

is insufficient to balance the momentum budget at the zero mean wind level [Holton, 1982] and induce a reversal of the zonal wind shear gradient. The question remained as to the origin of this eddy process. Eventually, the nature of the drag mechanism needed to balance the thermal and momentum budgets of the middle atmosphere was suggested to be the dissipation of gravity waves [Lindzen, 1967; Hodges, 1969; Houghton, 1978; Holton and Wehrbein, 1980].

### 3. Theory of Wave Dynamics

Despite rather regular behavior of the mean winds, the winds observed over short time spans are quite variable, the variability increasing with height. Upon observations of these short period fluctuations in the middle atmosphere, Hines [1960] proposed a theory describing fluctuations in the upper atmosphere in terms of (upward) propagation of gravity waves and the consequences of dissipation and wave-wave interaction. Hines was able to predict some of the important effects of gravity waves in the middle atmosphere, including the transport of energy, the generation of turbulence, the cascade of energy to smaller scale waves as the result of large gravity wave amplitudes, and the modulation of the middle atmosphere due to the variable energies of upward propagating gravity waves.

Gravity waves propagating upward from the troposphere are now accepted as the primary sources of these external fluctuations. Under the constraints of conservation of energy, the amplitudes of vertically propagating atmospheric gravity waves (as well as planetary waves and tidal oscillations) must increase as they pass into regions of lower density. The wave kinetic energy density,  $1/2 \rho U^2$ , remains constant in the absence of dissipation. It follows that

$$|U| = c\rho^{-1/2}, \quad (7)$$

where  $\rho$  is the mean background density and  $c$  is a constant. Since  $\rho$  varies exponentially with altitude as  $\rho_0 \exp(-z/H)$ , where  $\rho_0$  is the density at  $z=0$ , then

$$|U(z)| = c\rho_0 \exp(z/2H), \quad (8)$$

i.e., the wave amplitude grows by  $e$  every two scale heights ( $H$ ).

Recognition of the significance of atmospheric gravity waves led to a number of investigations in which two separate effects of gravity wave forcing were examined: the generation of turbulence and transfer of momentum.

As atmospheric gravity waves propagate through the stratosphere their amplitudes grow exponentially until at some altitude—the upper stratosphere, the mesosphere, or the lower thermosphere—they approach a level where the amplitude is so large as to be dynamically unstable. The resultant convective instability, shear instability, or Kelvin-Helmholtz instability, causes the unstable wave to overturn or “break” [Hodges, 1967; Lindzen, 1968] producing turbulence and smaller scale gravity waves. Further vertical amplitude growth is prohibited by an irreversible exchange of energy from the wave into the production of turbulence and heat to the surrounding medium [Hodges, 1969].

Bretherton [1966] and Booker and Bretherton [1967] demonstrated that gravity waves have a significant influence on the mean flow by their ability to interact with the mean flow and redistribute momentum and energy between layers of the atmosphere. They found a discontinuity of the gravity wave momentum flux at the same level where the wave's horizontal phase speed matches the mean background wind. At this altitude, gravity wave energy dissipates as the wave is absorbed into the mean flow, thus prohibiting or filtering these waves from further propagation [Booker and Bretherton, 1967]. This level was aptly named the “critical level” as it is here that the termination of amplitude growth creates a divergence of horizontal momentum flux and introduces a deceleration of the mean zonal flow and production of turbulence at the breaking level [Bretherton, 1966]. This acceleration will drive the mean flow toward the horizontal phase speed of the wave [Fritts, 1984] but it is typically manifested as a drag on the mean wind [Lindzen, 1981].

Through both wave breaking and the transfer of energy to the medium at the critical level, the interactions of gravity waves with the prevailing winds, planetary waves, and tides become significant [e.g., Walterscheid, 1981; Fritts, 1984; Forbes, 1984; Forbes and Vial, 1989]. The dissipative Rayleigh damping of Holton and Wehrbein [1980] involves the divergence of eddy momentum flux associated with transient waves and could be considered a crude parameterization of gravity wave drag. Lindzen [1981]

would modify the Rayleigh drag with a simple parameterization in which the effects of breaking gravity waves included both momentum deposition (representing wave forcing) and eddy diffusivity (accounting for turbulence). He further added that the attenuation of gravity waves at mesospheric levels may be caused by absorption of the waves at a critical layer or by the breaking of the waves themselves at a different altitude, thus advancing the concept that gravity waves with a variety of vertical and horizontal wavelengths are excited in the lower atmosphere, propagate upwards into the mesosphere, saturate, and deposit momentum to the mean flow.

Lindzen's parameterization, unlike Rayleigh friction, enabled expressions for the turbulent diffusion and for wave drag that are functions of  $(\bar{u} - c)$ , the difference between the zonal mean wind  $u$ , and the horizontal phase speed of the wave,  $c$ . In this way, wave drag can produce positive or negative acceleration of the zonal wind depending on the sign of  $\bar{u} - c$ . The characteristics of the gravity wave field at a given altitude will depend on the critical level filtering imposed by the background wind field. Wave saturation can result from either the growth of wave amplitude with height (breaking level) or from the approach to a critical level. The wave-induced accelerations provide an explicit source for the "friction" needed to reverse mesospheric wind shears and to reverse the pole-to-pole temperature gradient at the mesopause while forcing the mean flow toward the wave phase speed. The drag exerted by dissipating waves is now known to exert a substantial influence on the general circulation throughout the atmosphere while the induced turbulent diffusion encourages fluctuations in the constituent structure.

Studies and measurements of middle atmospheric gravity waves have increased dramatically since Lindzen [1981] offered a more satisfactory description for the mean zonal wind reversals observed in the upper mesosphere and lower thermosphere by relating the acceleration accompanying the wave momentum flux divergence to the phase speed of the wave. Temperature and density observations in this region have shown distinct wave-like structures with large spatial and temporal variability [e.g., Hines, 1960; Schmidlin, 1976; Hauchecorne and Chanin, 1980; Mitchell et al., 1991], indicating frequent penetration of external perturbations of many different scale sizes into this region. The existence of wave activity up to mesopause heights is well documented [Vincent and Fritts, 1987; Reid and Vincent, 1987;



*Manson et al.*, 1989; *Tsuda et al.*, 1990; *Wilson et al.*, 1991; *Swenson and Mende*, 1994]. These observations, together with various numerical models that were able to simulate the main features of large-scale thermal, dynamic, and chemical structure of the mesosphere [*Holton*, 1983; *Geller*, 1983; *Garcia and Solomon*, 1985], have been discussed by a number of authors [e.g., *Lindzen*, 1981; *Holton*, 1982; *Schoeberl et al.*, 1983; *Fritts*, 1984, 1989; *Dunkerton*, 1989]. As the models become more sophisticated, the best way of understanding this interrelationship of waves is through measurements of winds and temperatures in this region, with good temporal and spatial resolution.

#### 4. Gravity Wave Spectra

The spectral characteristics that the gravity wave field displays at a given altitude depend on the propagation and growth of the gravity wave as well as the filtering induced by the underlying wind profile between the source region and the thermosphere. Most theoretical studies of gravity wave spectra of atmospheric winds follow one of two lines of research: those that rely upon convective or dynamical instabilities within the wave field to dissipate wave energy and thus limit wave amplitudes, and those that assume wave amplitudes are limited by nonlinear interactions among the components of the gravity wave spectrum. A common feature of all of these studies is that atmospheric waves are principally responsible for the momentum dissipation of the mean flow and the generation of turbulence, and that the effect of wave breaking is not simply to decelerate the zonal flow to zero (as was the case with Rayleigh friction) but, more generally, to accelerate or decelerate the flow to the (zonal) phase velocity of the breaking wave.

We have essentially followed the theory in which the saturation of gravity waves is caused by linear shear and convective instabilities in the wave field, referred to as the linear instability theory of gravity wave breaking initially proposed by *Dewan and Good* [1986]. They suggested that vertically propagating atmospheric waves will undergo a filtering process due to the effect of the background winds. When a packet of isotropic waves rises through the atmosphere, components propagating in the same direction as the prevailing wind are lost, and those with a phase propagation direction opposite that of the wind are retained. The remaining waves will increase in amplitude with height at an exponential rate, whereupon instabilities set in. At this point the wave becomes unstable and is said to "break," producing

turbulent energy that prevents further growth of the wave with altitude. A constant amplitude is maintained and the waves dissipate, generate turbulence and deposit mean heat and momentum into the mean flow [Lindzen, 1967; Hodges, 1967, 1969]. Consequently, the layer will be accelerated in the direction opposite to the prevailing winds, as the result of convergence of the momentum flux associated with the waves. In the lower layer, wave components propagating in the same direction as the wind are absorbed, creating an acceleration of the prevailing wind system. This mechanism, unlike Rayleigh friction, is able to produce winds in the opposite direction to the primary winds. Such a reversal of winds is actually observed near the mesopause [e.g., Manson *et al.*, 1974].

Others have demonstrated that a similar form of gravity wave spectrum is achievable using such nonlinear mechanisms as Doppler spreading of the vertical wavelengths [Hines, 1991] by both the background wind and the wave induced winds, and scale-dependent [Weinstock, 1990] and scale-independent [Gardner, 1994] diffusive filtering processes involving nonlinear wave-wave interactions.

Although considerable theoretical work has been done to provide information about the physical and dynamical effects of propagating waves in the atmosphere, it was only through observations in the last few decades that gravity wave saturation have been recognized to play a crucial role in the large scale circulation of the middle atmosphere. We examine some fundamentals on atmospheric waves in the next chapter, before reviewing the lidar technique and observations made at USU.

## CHAPTER 3

### ATMOSPHERIC WAVES

#### 1. Wave Characteristics

The atmosphere is able to sustain a variety of wave motions, most of which are a combination of longitudinal and transverse waves. The three types that are most important to the large-scale dynamical behavior of the middle atmosphere are gravity waves, planetary waves, and tides. In addition, wave-wave and wave-mean flow interactions frequently alter the motions of the atmosphere as the different wave components combine to create a wave packet or traveling disturbance characterized by variations in the mean background wind speed, atmospheric temperature, and atmospheric pressure. These waves are dispersive, as the separate wave components have different phase speeds, and thus the energy of the wave packet is dispersed and the shape of the disturbance changes (flattens and broadens) as the wave travels.

Gravity waves are oscillations in which the restoring force is gravity. The best known examples are ocean waves, which exist largely because of the abrupt change of density at the water-air boundary. But gravity waves are not restricted to interfaces: They can also occur in the interior of a medium, such as the atmosphere. Although tides are gravity waves by nature, they are classified as forced waves that must be continuously maintained by diurnal variations of heating due to absorption of solar radiation by water vapor and ozone. The restoring mechanism for planetary waves is the conservation of planetary vorticity imparted by the longitudinal gradient of the Coriolis effect for a rotating earth.

Storm fronts and convection [Fritts and Nastrom, 1992], jet streams [Fritts and Nastrom, 1992; Tsuda *et al.*, 1994], flow over mountains [Nastrom and Fritts, 1992; Bacmeister, 1993], and lightning [Taylor and Hapgood, 1987] are believed to be the most likely tropospheric sources of gravity waves. Planetary waves and tidal intrusions originating in the troposphere and stratosphere will also produce fluctuations in the atmosphere.

Linear wave theory [see Andrews *et al.*, 1987] follows the assumption that wave fields (wind, pressure, temperature, density, etc.) are composed of a background (mean) state and small fluctuating component about the mean. For example, we can express a field  $X$  in the following manner

$$X = X_o + X' \quad (9)$$

where  $X_o$  is the mean field and  $X'$  is the deviation from  $X_o$ . With the assumption that  $X'$  is small, we can linearize the equations in  $X$ , i.e., neglect quadratic and higher order terms of perturbed fields. If the atmosphere undergoes small disturbances or fluctuations, the interaction of the mean flow with the disturbance results in wave motions. First-order perturbation theory applied to the basic equations—momentum, energy (adiabatic equation of state) and continuity—can describe many characteristics of wave phenomena as well as wave motions in the atmosphere. The equations of the basic state are rewritten in terms of the mean and perturbations about the mean of density, pressure, temperature, and velocities. Terms involving only the basic state cancel since the basic state must also be a solution. The resulting equations represent the interaction between mean and perturbed fields in the appearance of effective “forcing” terms (eddy momentum flux). In order to obtain a closed set of equations, it is necessary to either neglect these terms, simplify and assume they are known a priori, or parameterize them. It turns out that the radiative-dynamical balance of the mesopause region is inextricably involved with wave-mean flow interactions making it necessary to impose simplifications and parameterizations.

This leads to a set of homogeneous linear equations for the horizontal and vertical components of the equations of motion, continuity, and state. Assuming a nonrotating flat earth, negligible molecular and turbulent viscosity, and the basic flow as  $U = u_o$ ,  $v_o = 0$ , we get [following Lindzen, 1990]:

$$\frac{\partial u}{\partial t} = -\frac{1}{\rho_o} \frac{\partial p'}{\partial x} \quad (10)$$

$$\rho_o \frac{\partial w'}{\partial t} = -g\rho' - \frac{\partial p'}{\partial z} \quad (11)$$

$$\frac{\partial u'}{\partial t} + \frac{\partial w'}{\partial z} = 0 \quad (12)$$

$$\frac{\partial \rho'}{\partial t} + w' \frac{\partial \rho_o}{\partial z} = 0 \quad (13)$$

where the coordinate system is aligned so that (x) lies along the direction of horizontal phase propagation and (z) denotes the vertical direction,  $g$  is the acceleration due to gravity,  $\rho$  is density, and  $p$  is pressure.

Two-dimensional (given horizontal symmetry) plane wave solutions assume the form

$$u', v', w', p', \rho' \propto \exp [i(kx - mz - \omega t)] \quad (14)$$

where  $\omega$  is the angular frequency of the wave, and  $k$  and  $m$  are the horizontal and vertical wavenumbers, respectively. These linearized perturbation equations can now be solved simultaneously to give a single wave equation whereby various wave characteristics can be represented that are unique to the scaling arguments, boundary conditions, and imposed forcing terms (e.g., tides). In addition, wave motion is assumed adiabatic and perturbations are small. Thus neglecting external forces except for gravitational force, heat source, and the Coriolis force in the perturbation equations, a dispersion equation for  $\omega$ ,  $k$ , and  $m$  can be obtained from this solution. The dispersion relation that results is

$$\omega^4 - \omega^2 c^2 (k^2 + m^2) + (\gamma - 1) g^2 k^2 + i \omega^2 \gamma g m = 0. \quad (15)$$

In this equation,  $c$  is the speed of sound, and  $\gamma$  is the ratio of specific heats for the atmospheric gas.

Specific dispersion relationships between  $\omega$  and  $k$  for the various types of waves are obtained through appropriate scaling assumptions and simplifications dependent on the phenomena under scrutiny.

## 2. Gravity Waves

### 2.1 Gravity Wave Theory

In a stable atmosphere, a displaced air parcel will undergo a temperature change at the adiabatic rate and will become cooler or warmer than the surrounding environment. Buoyancy will then force it back to its original position causing oscillations about this point. The maximum frequency of vertical oscillations that the atmosphere can support is called the Brunt Vaisala frequency ( $N$ )

$$N^2 = \frac{g}{T} \left( \frac{dT}{dz} + \frac{g}{c_p} \right) \quad (16)$$

where  $c_p$  represents the specific heat at constant pressure. This is the internal resonant frequency of the atmosphere obtained mathematically by balancing the vertical accelerations of the parcel with the buoyancy force of the atmosphere. The stability of the atmosphere is represented by positive values of  $N^2$ . If  $N^2$  is negative, the layer is statically unstable and no oscillation occurs.

Gravity waves are not purely longitudinal because gravity has produced a component of the motion transverse to the propagation direction. Considered the primary cause of mesoscale fluctuations throughout the atmosphere, they occur on scales much less than the earth's radius with periods smaller than a day, thus the effects of the Earth's rotation and curvature can be neglected when simplifying the illustration of gravity wave propagation characteristics.

Waves of frequency ( $\omega$ ) will essentially do one of three things: propagate both vertically and horizontally in the absence of dissipation ( $\omega < N$ ), form with no vertical propagation ( $\omega \approx N$ ), or decay with height ( $\omega > N$ ), since waves with frequencies comparable to or larger than buoyancy frequencies violate the hydrostatic relation. This can best be illustrated by substituting the Brunt-Vaisalla frequency into the dispersion relationship. For the simplest case of gravity waves, we assume a flat earth with a continuously stratified and incompressible atmosphere that is isothermal (scale height,  $H$ , is constant) and uniform in composition and stationary in the absence of waves we get

$$\omega = \pm \frac{N k}{(k^2 + m^2)^{1/2}} \quad (17)$$

Close scrutiny indicates the vertical phase velocity  $c_{ph}$

$$c_{ph} = \frac{\omega}{m} = \pm \frac{N k}{m (k^2 + m^2)^{1/2}} \quad (18)$$

and vertical group velocity,  $c_g$

$$c_g = \frac{\partial \omega}{\partial m} = \mp \frac{N k m}{(k^2 + m^2)^{3/2}} \quad (19)$$

are in opposite directions; therefore, a wave propagating upward will have a downward phase progression.

In a fluid such as the ocean, which is bounded both above and below, gravity waves propagate primarily in the horizontal plane since vertically traveling waves are reflected from the boundaries to form standing waves. However, in the atmosphere, no upper boundary exists and gravity waves may propagate vertically as well as horizontally. In vertically propagating waves the phase is a function of height, such waves are referred to as internal waves. Internal gravity waves with a vertical phase velocity component

are believed to be an important mechanism for transporting energy and momentum to high levels, and it is these waves we are referring to in this dissertation as vertically propagating gravity waves.

Gravity waves emerge as the dominant wave feature at middle and high latitudes. Their variability is due primarily to two factors. One is the variability of the source, including source type strength, wave characteristics, and temporal and spatial distribution. The other factor is the modulation of the wave field by the local environment, including background winds and low-frequency wave structures. When these waves originate in the troposphere their phase speeds will typically range from zero (mountain waves) to typical tropospheric flow speeds (e.g., jet stream velocities). The mean flow distribution, which varies with season, effectively determines which gravity waves (depending on phase speed) will reach the mesosphere and relatedly the amplitudes and breaking levels of gravity waves reaching the mesosphere. Specifically, when the wave phase speed is equal to the mean zonal wind speed ( $\bar{u} = c$ ), the wave will be absorbed [Lindzen, 1981]. The altitude where this occurs is referred to as the critical level. During summer (June through September), when the prevailing mesospheric and stratospheric winds are easterly (towards the west), propagation of waves up through the stratosphere is expected to be blocked, leading to a small variability in the temperature profiles, whereas in the winter (October through March) when prevailing winds are westerly (towards the east), the temperature profiles are expected to be continuously perturbed by wave activity. Figure 4 shows how this absorption effect influences wave propagation in summer and winter for mid-latitudes.

## 2.2 Observations of Gravity Waves

Many, but not all, gravity waves are triggered by changes in the flow of wind over mountains and other extended topographic features, so they are not restricted to a particular range of latitudes. Their probability of occurrence may depend on season, however, because the initiation of topographically generated gravity waves depends on the wind at low altitudes, and their ability to propagate upward depends on the winds in the stratosphere and mesosphere, which have strong seasonal variations.

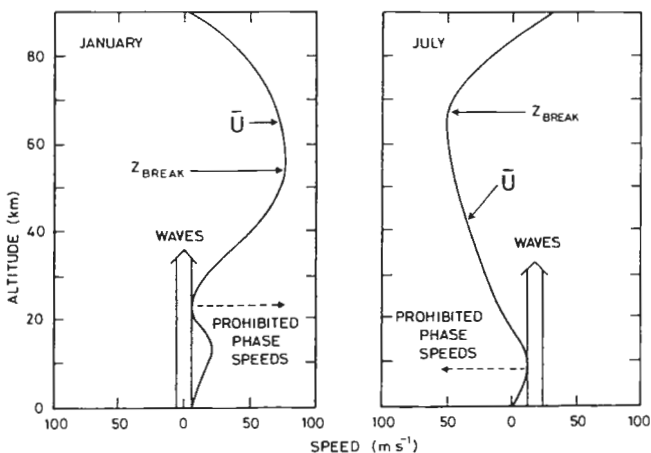


**Figure 4.** Schematic showing the approximate altitude profiles of the mean zonal winds for summer and winter. Also shown are the permitted phase speeds for gravity waves propagating into the mesosphere and their estimated breaking levels [Brasseur and Solomon, 1984].

Internal gravity waves are often observed at middle and high latitudes, especially in winter.

Generally, a shorter period results in a smaller phase speed and shorter wavelength. Lidars provide the ability not only to detect gravity waves from the ground but also to monitor the gravity waves on a continual basis by observing their effect on the density and temperature of the middle atmosphere.

Temperature measurements between 50–70 km at mid-latitudes reveal waves with a downward phase propagation and phase velocities of about 4 km/hr, vertical wavelengths of 8 km, and periods of 3–4



hours [Chanin and Hauchecorne, 1981], consistent with *internal gravity waves* generated in the troposphere and propagating upwards. Below 50 km, the waves exhibit a much slower phase descent of  $\sim 0.5$  km/hr, and a longer period ( $\sim 24$  hours) indicative of a diurnal tidal mode between 30 and 50 km. Other observations confirm the presence of vertical wavelengths of 2–3 km in the lower stratosphere, 5–10 km in the upper stratosphere, and 15 km in the mesosphere [Tsuda *et al.*, 1994; Gardner *et al.*, 1989].

Above 70 km, lidar observations indicate very large density perturbations probably due to the turbulence from the breaking of gravity waves at or above this altitude or the superposition of gravity waves with tropospheric origins and tides. Fourier analysis of the profiles between 30 and 70 km [Chanin and Hauchecorne, 1981] indicated most of the energy spectra is within the vertical wavelength range of 8 to 15 km with a secondary maximum of shorter wavelength waves in summer (6–8 km) and longer wavelength waves in winter (20–27 km). This difference between summer and winter is due in part to the filtering of the waves by mesospheric zonal winds [Lindzen, 1981].

The relationship between gravity wave activity and production of turbulent kinetic energy in regions where they break is well identified. Longer period waves with vertical scales  $\sim 10$  km dominate the mesospheric region, modifying the wind and temperature structure and inducing unstable conditions where breaking waves will produce turbulence [Tsuda *et al.*, 1994] although these turbulent layers are somewhat affected by the large-scale temperature structure (planetary waves, tides, background winds). Seasonal variations in gravity wave activity demonstrate a winter maximum and summer minimum in the lower stratosphere while a double maximum appears in the mesosphere where the summer mesospheric maximum is dominant. The winter mesosphere suggests a seasonal asymmetry most likely affected by large scale variations such as atmospheric tides [Fritts and Vincent, 1987].

Large-scale, long period quasi-monochromatic gravity waves have been observed frequently in the 30–60 km range [Mitchell *et al.*, 1991; Shibata *et al.*, 1986; Chanin and Hauchecorne, 1981; Gardner *et al.*, 1989; Whiteway *et al.*, 1995]. These reports suggest this may represent the normal state of the wave field at these heights. These waves are characterized by vertical wavelengths of 10 km in the lower mesosphere and 4 km in the stratosphere. Periods are commonly less than the inertial period ( $2\Omega \sin\phi/\pi$ ,

where  $\Omega = 7.2921 \times 10^{-5}$  radians/s, and  $\phi$ =latitude) for the latitude of observation, and slow phase speeds on the order of 1 km/h are often observed (though *Mitchell et al.* rarely saw persistence over many nights). *Mitchell et al.* [1991] suggested the shorter periods reported by *Chanin and Hauchecorne* [1981] and *Gardner et al.* [1989] may have under represented motions of long periods. While not observed in summer, there is evidence of their presence, but amplitudes may be small and indistinguishable from noise [*Mitchell et al.*, 1991].

Spectrum analysis of gravity waves showed strong gravity wave activity at 25–45 km during stratospheric warmings [*Philbrick and Chen*, 1992]. The lack of gravity wave activity at 45–65 km implied that the critical layer interaction was below 50 km during the event, indicating that stratospheric filtering of gravity waves was induced by planetary waves in this region.

### 3. Planetary Waves

#### 3.1 Planetary Wave Theory

Planetary, or Rossby waves are large-scale waves that are influenced by the earth's curvature and rotation (the Coriolis parameter). The conservation of planetary vorticity (a measure of a liquid's tendency to rotate) is based on the latitudinal variation of the Coriolis force and acts as a restoring force on these horizontally transverse waves. As with gravity waves, planetary waves also originate in the troposphere and propagate through the stratosphere into the mesosphere [*Holton*, 1979], transporting heat and momentum. The eddy motions in the stratosphere consist primarily of ultralong quasi-stationary planetary waves which seem to be confined to the winter hemisphere. Variations in the stratopause altitude have been detected in the mid-latitude winter hemisphere [*Hauchecorne and Chanin*, 1982] and attributed to the action of planetary waves. These planetary waves propagate zonally in either direction with meridional displacements and exhibit large-scale asymmetries in the middle atmospheric flow.

The traditional approach to modeling planetary waves in the middle atmosphere has been to solve the linearized primitive equations, parameterizing terms for eddy and molecular diffusion of heat and momentum by Rayleigh friction [*Salby*, 1984]. From the subsequent dispersion relationship we find that

periods must be larger than the semidiurnal period [Beer, 1974] and for vertical propagation of planetary waves, the mean wind must be westerly (toward the east). In summertime, the prevailing mesospheric and stratospheric winds are easterly (towards the west) and propagation of planetary waves up through the stratosphere is expected to be blocked. However in wintertime, winds are westerly (towards the east), thus more planetary wave activity is able to propagate into the middle atmosphere and the temperature profiles are expected to be continuously perturbed by planetary wave activity.

Although they play a significant role in middle atmospheric phenomenon, planetary wave fluxes are probably not responsible for providing the necessary zonal momentum dissipation to maintain the mean zonal wind and temperature states that are observed [Geller, 1983]. The strongest argument for this is that the same order of magnitude decelerations are required in both the summer and winter hemispheres, but planetary waves are not observed to propagate through the lower stratosphere in summer given the easterly (towards the west) flows there [Charney and Drazin, 1961]. This filtering action of stratospheric-mesospheric planetary waves can also modulate gravity wave accessibility to the upper atmosphere [Holton, 1984] by the oscillatory disturbances at stratospheric levels, thereby inducing a long period oscillation at mesopause heights in summer [Forbes *et al.*, 1995; Smith, 1996].

### 3.2 Observations of Planetary Waves

*Hauchecorne and Chanin* [1983] conducted an analysis of temperature profiles taken between June 1981 and April 1982. They observed summer profiles similar to those of the CIRA 72 model in which no disturbances were present. In October, as the lower stratospheric winds reverse from easterly (towards the west) to westerly (towards the east), temperatures become more variable as a succession of large perturbations develop in the upper stratosphere and the mesosphere due to the planetary waves propagating through the middle atmosphere. By March, as the seasonal reversal of winds from the typical winter westerlies to the summer easterlies begins, the upward propagation of planetary waves is blocked in the stratosphere and the wave is unnoticeable at mesosphere heights.

Planetary waves are commonly reported in three categories [Vincent, 1984]: the 16-day wave, the 5-day wave, and the 2-day wave. However, spectral analysis of data collected during winter 1981–1982 [Hauchecorne and Chanin, 1983] revealed two main periods in the mesosphere, 18 and 25–40 days, the latter having greater amplitudes. Natural variations in the winter stratopause height have a period of ~20 days [Hauchecorne and Chanin, 1982] and are attributed to the interaction of planetary waves. These winter temperature profiles are characterized by a vertical wavelength of ~40 km, which appears to be quite typical [Offermann *et al.*, 1979; Hauchecorne and Chanin, 1982]. This period may be related to the 16-day wave, which is observed in the winter lower stratosphere [Madden and Labitzke, 1981]. However, the periodic variation of the structures does not appear to be due to the propagation of a single planetary wave but rather a number of waves with different periods. Wave amplitudes are greater at mid-latitudes than in the tropics [Barnett and Corney, 1985b], with the largest amplitudes generally occurring in the stratosphere and lower mesosphere, but still rather large variations remain up to the mesopause.

The stratosphere and mesosphere are subject to a regular succession of coolings and warmings where each cooling is associated with a warming ~20 km above or below corresponding to the 40-km vertical wavelength. During this pattern, the zonal winds in the lower stratosphere (20–30 km) were observed to be accelerated westerly (towards the east) at the time when warming is maximum in the upper stratosphere (40–45 km), and a reversal to easterly (towards the west) winds when the warming reaches the lower stratosphere. As the lower stratosphere cools, westerly (towards the east) winds return. These structures create an anti-correlation between the temperature variation of the upper stratosphere (40–45 km) and the lower mesosphere (55–60 km) [Hauchecorne and Chanin, 1983] so that as warming near 50 km descends into the 40-km region, mesospheric cooling will descend from 70 to 58 km.

Although high amplitude wave-like perturbations in the mesospheric temperature [Theon *et al.*, 1967; Schmidlin, 1976; Hauchecorne and Chanin, 1980, 1983] have been attributed to the presence of planetary waves, Jenkins *et al.* [1987] found no indication of a downward phase progression on most nights over Aberystwyth, ruling out the interpretation of a traveling planetary wave or a propagating tide. Thus he anticipated either a persistent stationary (or very slow moving) planetary wave in the mesosphere or

some other equally persistent wave-like disturbance such as long period gravity waves [Mitchell *et al.*, 1991].

And finally, large variations of the zonal wind are often observed in the tropical lower stratosphere, with periods of 20 to 40 months, but exhibiting a mean period of 26 months normally referred to as the quasi-biennial oscillation, or QBO [Veryard and Ebdon, 1961; Reed *et al.*, 1961]. Theoretical studies indicate that their origin lies in the vertical transport of momentum associated with certain types of tropical waves [Lindzen and Holton, 1968; Holton and Lindzen, 1972]. Total ozone exhibits a variation in the tropics which is apparently related to the QBO [Hilsenrath and Schlesinger, 1981] and a 26-month cycle has been observed at mid-latitudes in middle atmospheric temperature profiles [Chanin *et al.*, 1989b]. The relationship between the QBO and planetary waves has not yet been fully explored.

#### 4. Atmospheric Tides

Tides are global-scale periodic atmospheric oscillations related to the solar or the lunar day and subharmonics thereof (i.e., 24 hours, 12 hours, etc.). Unlike ocean tides, which are predominantly due to gravitational gradients, atmospheric tides are predominantly due to solar heating. These tides are excited directly or indirectly by the daily variation of solar thermal forcing generated by absorption of solar energy by  $O_3$  in the stratosphere and  $H_2O$  in the troposphere [Chapman and Lindzen, 1970]. The earth's atmosphere responds to these periodic forces in a manner analogous to forced mechanical oscillations. For solar tides, the daily cycle of heating and cooling in the atmosphere would produce a single tide with a period of 24 hours. The possibility of tidal periods less than 24 hours comes about because the daily heating cycle is more a square wave than a purely sinusoidal wave and as such, contains many harmonics.

The wind field of the upper mesosphere is dominated seasonally by prevailing winds and diurnally by solar tides. Diurnal tides propagate vertically only below 30° latitude. At higher latitudes they remain trapped in the stratosphere. With decreasing importance of the diurnal tide at mid-latitude mesospheric altitudes, the semidiurnal tide becomes dominant with an amplitude at least as large as the prevailing wind (order of 10s m/s). In general, several tidal modes coexist and superpose linearly (mode

coupling ) so that a realistic mean horizontal structure of the atmosphere with distinct separable modes is obscured. Propagating tides can be viewed as gravity waves for which the rotation and sphericity of the earth must be taken into account due to their long periods and horizontal wavelengths. Theoretically, atmospheric tides may propagate eastward or westward, but as a rule a tidal perturbation will travel or migrate westward with respect to the earth's surface so that it remains synchronized with the apparent motion of the sun or moon. As with all atmospheric waves, tidal amplitudes increase with height as they propagate upward from their source regions. They also influence temperature and wind oscillations along the way. At ground level the typical fractional pressure variation is about  $10^{-3}$  and the tidal wind is about 0.05 m/s. At 100 km the pressure variation is 10% and the corresponding air speed 50 m/s. These tides may appear as variations of the background atmospheric fields and are capable of generating turbulence and depositing heat and momentum at mesopause heights.

#### 4.1. Tidal Theory

To interpret tidal motions one should understand the normal modes of oscillation of the atmosphere and consider how effectively these are stimulated by the forcing agent. General tidal theory includes considerable mathematical complexity. In order to account for longer time (order of 24 hours) and length (order of hundreds of km) scales, the equations of the atmosphere must be solved on a rotating spherical shell (i.e., a latitude dependent Coriolis force) subject to the earth's gravitational field with the addition of a tidal potential function (the driving or forcing term) and a periodic thermal forcing term. As with other wave studies, we assume the tidal fields to be small perturbations about some mean and linearize the basic equations in accordance with perturbation theory. It is convenient to express them in polar coordinates and assume that the tidal variables have solutions that are periodic in both time and longitude, such as

$$G^{\sigma,s}(\theta, z) \exp[i(\sigma t + s\phi)] \quad (20)$$

where  $\sigma$  is the angular frequency of the tidal oscillation and  $s$  is the zonal wavenumber ( $s$  must be an integer) for colatitude,  $\theta$ , longitude,  $\phi$ , and altitude,  $z$ . Substitution into the set of linearized equations

(which now include Coriolis force and tidal forcing functions) leads to a second-order partial differential equation in the variable  $G$ :

$$H \frac{d^2 G^{\sigma, \nu}}{dz^2} + \left( \frac{dH}{dz} - 1 \right) \frac{dG^{\sigma, \nu}}{dz} = \frac{g}{4a^2 \omega^2} F \left\{ \left( \frac{dH}{dz} + \kappa \right) G^{\sigma, \nu} - \frac{\kappa}{\gamma} \frac{J^{\sigma, \nu}}{gH} \right\} \quad (21)$$

where  $H$  is the atmospheric scale height defined as  $RT(z)/g$ ,  $a$  is the earth's radius,  $J$  is the thermotidal heating per unit mass per unit time and represents the periodic driving force acting on the free atmospheric oscillations,  $\kappa = (\gamma - 1)/\gamma$ ,  $\gamma$  is the ratio of specific heats,  $\omega$  is the rate of rotation of the earth, and  $F$  is defined as a differential operator.

This equation is separable in terms of latitude, longitude, altitude( $z$ ), and time( $t$ ). Solutions of the second-order differential equation can be expanded in a series solution for  $G$  and  $J$ , in which the latitude dependence is expressed in terms of orthogonal functions, or Hough functions,  $\Theta$ , which can be expanded by the associated Legendre polynomials:

$$G(\theta, z) = \sum_n L_n(z) \Theta_n^{\sigma, \nu}(\theta) \quad (22)$$

$$J(\theta, z) = \sum_n J_n(z) \Theta_n^{\sigma, \nu}(\theta). \quad (23)$$

Hough functions are latitudinal structures of perturbations in temperature, pressure, density, and vertical velocity that describe the various modes of oscillation, identified according to their zonal and meridional wavenumbers ( $s$  and  $n$ , respectively). Substituting the Hough functions into Equation 21, we obtain an eigenvalue equation, referred to as the Laplace tidal equation describing tidal motions:

$$F(\Theta_n^{\sigma, \nu}) = - \frac{4a^2 \omega^2}{g h_n^{\sigma, \nu}} \Theta_n^{\sigma, \nu} \quad (24)$$

where  $h_n$  representing the set of eigenvalues, is called the equivalent depth, given in dimensions of length and  $\Theta_n$  the set of eigenfunctions. The equivalent depths depend on the parameters of the atmosphere particularly to the temperature profile [Lindzen, 1968] and provides the link between the horizontal and vertical structure of the mode. Proper manipulation and substitutions leads to the vertical structure equation:

$$H \frac{d^2 L_n^{\sigma,s}}{dz^2} + \left( \frac{dH}{dz} - 1 \right) \frac{dL_n^{\sigma,s}}{dz} + \frac{1}{h_n^{\sigma,s}} \left( \frac{dH}{dz} + \kappa \right) L_n^{\sigma,s} = \frac{\kappa}{\gamma g H h_n^{\sigma,s}} J_n^{\sigma,s} \quad (25)$$

where  $h_n^{\sigma,s}$  is the separation constant. Given two boundary conditions, this equation yields a unique solution for the vertical structure for a given Hough mode ( $s, n$ ). The height dependence of these normal modes is a crucial factor in tidal theory, since thermal forcing (i.e., solar heating) is included in the equations, the only modes excited are those having a vertical structure that matches the vertical structure of the forcing. As the meridional wave number ( $n$ ) increases, the equivalent depth decreases, indicating that the higher harmonics will be shallower in vertical extent and damp quickly away from the source. If  $h_n$  is negative, no vertical propagation occurs and thus no transport of energy is possible.

For each period and value of  $s$  there is an infinite number of discrete meridional structures possible ( $n$ ). Only a few of the lowest order (longer period) modes (simplest structure) are expected to dominate in the atmosphere. For  $s=0$ , the temporal behavior does not propagate with respect to the earth. For the diurnal tide,  $s=1$ , the disturbance has a wavelength of one global circumference and propagates westward following the sun. The semidiurnal and terdiurnal tides correspond to  $s=2$  and  $s=3$ , respectively. At mid-latitudes, the semidiurnal tide (2,2) has a long vertical wavelength and is the dominant solar tide in the stratosphere and mesosphere while the diurnal tide (1,1) has a short wavelength of only 30 km, and is only a secondary component.

Recently, tidal modeling studies have progressed from the oversimplified assumptions of isothermal, inviscid, and motionless atmosphere [Lindzen, 1967] to include such complex processes as eddy and molecular diffusion of momentum and heat, latitudinal, seasonal, and solar cycle variations in thermal structure, wind circulation, chemical composition, and molecular and thermal conductivities and viscosities [Vial and Forbes, 1989; Forbes and Vial, 1989].

#### 4.2. Tidal Observations

The optimum observation period for data sets for use in tidal studies appears to be 10 days since shorter intervals may show nonglobal effects [Forbes, 1984] and a seasonal departure of the tidal phase may contaminate longer periods [Manson *et al.*, 1989].



Observations and theory have verified that the semidiurnal tide is stronger than the diurnal tide in mid-latitudes [Manson *et al.*, 1989] with a large vertical wavelength  $> 100$  km and an amplitude of roughly  $8 \pm 4$  K above 60 km in late summer and a shorter wavelength (50–80 km) with a greater amplitude of up to  $12 \pm 6$  K above 60 km in winter [Gille *et al.*, 1991]. A rather short (2 weeks) transition period occurs during spring [Forbes, 1990] and a rapid transition from summer to winter conditions has been observed as late as the end of November, during which time semidiurnal tidal amplitudes are reduced. Also, an increase in gravity wave activity for November over January at levels above 60 km [Wilson *et al.*, 1991] may indicate that gravity waves drown out the apparent tidal effects.

A variety of vertical structures can occur with the smaller amplitude diurnal tide at mid-latitude regions depending on phase interference between the evanescent and propagating components, making it difficult to define a typical structure. Vincent *et al.* [1989] observed hemispheric differences in the diurnal tide, but not in the semidiurnal mode.

Spectral analysis of lidar measurements in France during January 1989 [Gille *et al.*, 1991] displayed strong 12- and 24-hour periods above 50–75 km, suggesting that semidiurnal and diurnal tidal effects dominate gravity wave responses for periods of 10–60 hours in the mesosphere.

Observed amplitudes are often larger than model predictions [Hoxit and Henry, 1973; Gille *et al.*, 1991], suggesting more complicated processes than currently included in theory, including coupling with gravity waves or planetary waves, to create larger amplitudes than anticipated [Walterscheid, 1981]. Tidal modulation of gravity wave fluxes essentially leads to a "feedback" at tidal periods which can serve to locally damp or amplify the tide depending on the relative scales involved [Walterscheid, 1981]. The term pseudotides refers to such phenomena characterized by tidal frequency oscillations forced internally by tidally modulated gravity wave-mean flow interactions and may be caused by viscous absorption near critical levels [Walterscheid, 1981] or wave breakdown [Fritts and Vincent, 1987].

With this background information, we can infer how the interaction of winds with wave activity of many different periods influences the temperature structure of the mid-latitude middle atmosphere using

lidar measurements at USC. We begin with a discussion of the lidar instrument, the temperature measurement technique, and the accuracy of this technique in the next chapter.

## CHAPTER 4

## DERIVING TEMPERATURES FROM A LIDAR

The Rayleigh-scatter lidar method is unique in that it is the only ground-based remote sensing technique capable of providing precise, near continuous, high-resolution height profiles of middle atmospheric temperatures from 30 to 90 km. The method relies on the principle of Rayleigh scattering of a transmitted laser pulse by the atmospheric medium to determine density profiles then converting these density profiles into temperature profiles. Various assumptions, simplifications, and other possible sources of error may occur during the collection, processing, and analysis of the data which contribute to uncertainties or inaccuracies in the evaluation of the temperatures. A rigorous attempt was made to identify and reduce sources of error, not only to ensure more precise measurements but to allow more accurate comparisons with other observational methods. In this chapter we review the lidar system and the technique of retrieving temperature profiles. We then consider possible sources of error that may arise and discuss how we attempted to avoid or minimize them.

### 1. Rayleigh Lidar

The lidar technique involves emission of a powerful short laser light pulse, a small fraction of which returns to the detector due to backscatter by atmospheric molecules (and aerosols below 30 km). As these very short pulses of light are sent into the atmosphere, the altitude of backscatter is determined by the time delay between laser emission and detection, and range-resolved measurements are obtained in a manner analogous to radar. A time-gated return signal provides a vertical profile of atmospheric density, which can then be resolved into an absolute temperature profile.

The configuration of the USU lidar is shown in Figure 5. The hardware for the lidar consists of the transmitter, the receiver, and the data acquisition and processing hardware and software. The specific requirements of each element's characteristics are determined by the intended purpose of the lidar observations.

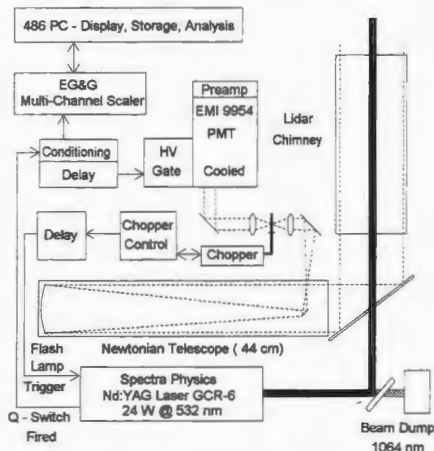


Figure 5. Schematic diagram of the USU lidar system.

### 1.1. Transmitter

#### 1.1.1 Laser Theory

At the heart of the lidar lies the laser. The laser generates a coherent, monochromatic, highly directional, intense photon beam. As the name implies, its operational principle is light amplification by the stimulated emission of radiation (laser). Quantum theory reveals that matter exists only in certain allowed energy levels or states. In thermal equilibrium, lower states are preferentially populated. Incident radiation at frequency  $\nu$  can cause a transition from the lower energy state to the upper energy state with the absorption of a photon. When matter in an excited state decays spontaneously to a lower energy state, a photon is emitted with a transition frequency  $\nu = \Delta E / h$  where  $\Delta E$  is the energy difference between the two states and  $h$  is Planck's constant. A transition from the upper state to the lower state may also be induced by radiation whereby a "clone" photon wave packet is emitted simultaneously with the stimulating radiation wave, possessing the same energy and momentum; this stimulated emission process

is the reverse of the absorption process. A laser is designed to take advantage of absorption, and both spontaneous and stimulated emission phenomena, using them to create conditions favorable to light amplification.

A laser generally requires an active medium with energy levels that can be selectively populated (e.g., Nd:YAG), a pumping or seeding process whose output matches principal absorption bands in the active medium, to establish population inversion, and a resonant cavity containing the active medium, which serves to store the emitted radiation. In a continuously operating laser, coherent radiation will build up in the cavity to a level set by the decrease in inversion required to balance the stimulated emission process with the cavity and medium losses. The system is then said to be lasing, and radiation is emitted in a direction defined by the cavity. The development of Q-switched laser pulsing provided the capability to produce short, high-energy laser pulses.

#### *1.1.2 Pulsing and Q Switching*

A laser made up of just the active medium and resonator will emit a pulse of laser light each time the flash lamp fires. However, the pulse duration will be long, about the same as the flash lamp, and its peak power will be low. The technique used to shorten the pulse and raise its peak power uses the idea that if the upper level of the transition has a long lifetime, a large population of excited neodymium ions can build up in the YAG rod, similar to the way a capacitor stores electrical energy. By preventing oscillation while the population inversion builds and releasing the stored energy quickly, stimulated emission occurs rapidly and the radiation is emitted in a short pulse of high intensity light. This technique of Q switching (quality factor switching) results in a pulse width of  $<10$  ns for the Nd:YAG laser, and peak optical power up to tens of megawatts.

Because the Rayleigh scattering cross section varies as  $\lambda^{-4}$ , one would expect that the optimum lidar wavelength would lie in the shorter wavelength, UV, part of the spectrum; however, the intensity of the return signal actually depends on other variables such as the energy per pulse of the laser, repetition rate, quantum efficiency of the PMT, and atmospheric transmittance for the selected wavelength selected.

Because of these restrictions as well as ease and expense of operation, the powerful Nd:YAG laser whose second harmonic produces a 532 nm signal is ideal for middle atmospheric studies.

The transmitter includes a high-power pulsed Nd:YAG laser and the associated optics. The lidar used for the observations reported here is a Spectra Physics GCR-6 flashlamp pumped laser employing neodymium-doped yttrium aluminum garnet (Nd:YAG) as the excitation medium. The GCR-6 consists of four colinear Nd:YAG crystals (two acting as oscillators initiating the pulse, and two acting as laser

amplifiers), emitting radiation at 1064 nm. The high peak power of Q-switched pulses permits frequency conversion in nonlinear crystals. As the radiation passes through a frequency doubling crystal mounted at the end of the laser, about 50% of the incident light is converted to 532 nm (green light). This green light is the active signal that is directed vertically along the receiving telescope's path via a series of dichroic mirrors, passive optical devices with high reflectance for the 532 nm emission and high transmittance for the 1064 nm emission. The laser generates 800 mJ per pulse at 532 nm with a repetition frequency of 30 Hz, providing a total power output of 24 watts. The pulse length is 8 ns and full-angle beam divergence of 0.5 mrad provides a 50 m FOV at 100 km. A summary of the lidar technical data is given in Table 1.

## 1.2. Receiver

The receiving system requires a light collector, optics, filters, and a photon counter. Theoretically, two basic configurations exist for laser remote sensors, bistatic in which the transmitter is separated from the receiver, and coaxial where the transmitter and receiver are co-located and with proper alignment the outgoing and incoming radiation travel along the same path but in different directions. The coaxial system ensures that the field-of-view of the receiver system includes the area illuminated by the

**Table 1.** Rayleigh Lidar Facility

Lidar Characteristics	
Configuration	Coaxial
Power-Aperture	3.42 W-m <sup>2</sup>
Laser (Nd:YAG) Spectra Physics GCR-6	
Wavelength	532 nm
Energy per Pulse	800 mJ
Repetition Rate	30 Hz
Power	24 W
Pulse Length	8 ns
Spectral Width	< 150 MHz (Seeded)
Beam Divergence	< 500 $\mu$ rad
Telescope — Newtonian	
Focal Length	2.20 m
Diameter	0.44 m
Effective Area	0.152 m <sup>2</sup>
Field of View	1.0–1.5 mrad

laser beam [Measures, 1988]. Because very little of the outgoing light is reflected back to the receiver, a telescope must be used to collect the return signal. For constant laser power, the magnitude of this signal is determined by the size of the telescope's collecting mirror.

The USU lidar system is a coaxial design such that the backscattered return signal is reflected off a mirror and enters a Newtonian telescope with a 44-cm diameter and 201-cm focal length. An adjustable aperture, placed in the focal plane of the telescope, allows control of the telescope field-of-view, and is typically chosen to be 2–3 times greater than the laser beam divergence.

The backscattered light incident on the telescope aperture is brought to a second focus at the vertical plane of the mechanical chopper after which the 532 nm light passes through a collimating lens and is directed toward the detector.

To detect the incoming photons, a red sensitive bialkali photomultiplier tube (PMT) (EMI 9954B) converts the individual photons into electronic pulses. As a photon enters the PMT, the photocathode emits an electron that is accelerated into a dynode, causing several secondary electrons to be emitted. These electrons hit another dynode, causing more electrons to be emitted. This process occurs at 12 dynodes, giving rise to a large pulse at the anode. The choice of a photodetector depends on its quantum efficiency at the wavelength of interest, frequency response, dark current, and ability to handle large pulses. The PMT is thermoelectrically cooled to reduce the dark count (spurious signals resulting from thermal fluctuations in the tube) and extend the altitude range of measurements. A narrow-band (0.5 nm) interference filter, centered on the wavelength being monitored and placed in front of the PMT, shields the photodetector from unwanted light.

Two difficulties arise in the detection of the lidar returns, the large dynamic range of the return signal (Figure 6) and the high illumination of the detector due to the backscatter of laser light at low altitudes. The PMT is electronically gated in order to accommodate the dynamic range of the number density of backscattered photons. This value extends over six orders of magnitude from 30 to 90 km. An electronic gating switch increases the voltage of the photocathode to equal that of the first dynode (e.g.,

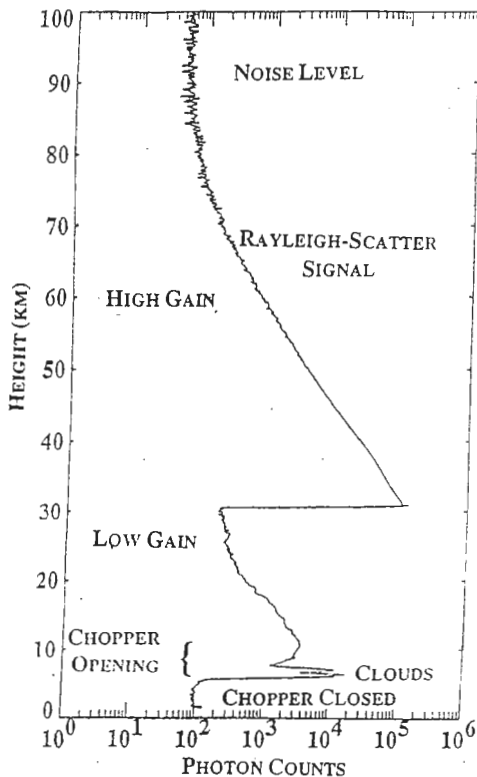


**Figure 6.** Dynamic range of backscattered USU lidar signal. Note the exponential decay of photon counts with height. Initially the chopper is shut and the signal level is low. As the chopper opens, there is a weak Rayleigh signal—weak because the PMT is in low gain. At 30 km, the gain is increased by a factor of 1000, and there is very good signal to approximately 90 km. Between 100 and 450 km is an extended region where we measure the background level.



from -2100 to -1800 ). The dynode voltage remains constant. This gating reduces the gain by a factor of between 100 and 1000 for protection against strong lower altitude ( $< 40$  km) returns.

On the other hand, the intensity from atmospheric scattering below 20 km is strong enough such that a PMT is easily saturated with light at the lowest altitudes. In addition to the electronic gating of the PMT, a high-speed mechanical chopper is used to prevent the near-field saturation problem by blocking the intense echoes from the troposphere and lower stratosphere ( $< 15$  km).

The mechanical chopper also controls the synchronization of the laser firing. However, the timing for sampling the return signal is controlled by the time the laser fires. The chopper blade contains two openings and rotates at 90 rps, providing a 180-Hz signal for the chopper position sensor. The chopper delay unit, triggered on the leading edge of every sixth opening (i.e., 30 Hz), is used to fire the flashlamps and the Q-switch. When the Q-switch fires, a pulse from the laser gates the phototubes, and synchronizes the multichannel scaling (MCS) data acquisition system. The signal is slightly delayed so that the laser is fired when the chopper is blocking the PMT from the intense low altitude returns and "opens" for the backscattered signal from above  $\sim 15$  km to reach. A buffer connected to the Q-switch starts the MCS boxes recording the signal and, after the specified delays, gates the high voltage to the PMT at a time which is set independently and corresponding to a predetermined altitude, chosen so as to minimize saturation at low altitudes.

### 1.3. Data Acquisition

The signal is sent to the MCS where it is discriminated, counted, and recorded in discrete time intervals corresponding to height range bins and saved as a range-gated value. The data acquisition software allows a variation of the dwell time and range of the MCS. The maximum vertical resolution of lidar measurements is determined by the time resolution of the scaler. The 250 ns time gate of the photon counter gives a spatial resolution of 37.5 meters per bin. A total of 14,000 such range bins is used to span an altitude range of 525 km. The temporal resolution is theoretically limited by the laser repetition interval (i.e., 33.3 ms) but actual limits are much longer. We used 3600 laser pulses, i.e., 2 minutes.

These data were used directly in spectral analysis work but for temperature analysis we chose to combine 30 of these 2-minute integrations.

#### 1.4. Data Processing

The initial data were reduced to a 112.5-meter resolution using a 3-point average over the range bins. Each profile has a high altitude above which the received signal is comparable to the background noise level and occurs at altitudes roughly above 100–120 km. Further data reduction (30-point total) was applied to altitude bins above 100 km, which basically represented the background. This then limited the background resolution to 1.125 km. As the system performance improved, this additional reduction of the data was moved to 120 km, still well into the background region of each profile.

The signal count is described by Poisson statistics such that accuracy at a particular altitude will increase as the square root of the number of counts. The most fundamental method of boosting the signal to levels above the background noise in these high altitude regions is to sum the 2-minute profiles into temporally resolved profiles of one to several hours. Summing the data into 1-hour integrations, for example, will increase the top altitude for a given accuracy by 15–20 km, and averaging an entire night's data will have a proportionately greater effect. Recent measurements suggest that reliable measurements in excess of 100 km are achievable by the USU lidar. Depending on the intended use, the data in this paper were summed over a 1-hour period or the entire night, and smoothed over 3 km using a simple boxcar average. While this dissertation is concerned mainly with temperature measurements, the USU lidar data have previously been used to study temperature perturbations [Wickwar *et al.*, 1995], power spectra [Sears *et al.*, 1997], and wavenumber spectra [Gao *et al.*, 1997] of mesospheric gravity waves.

## 2. Photons to Temperature

### 2.1. Atmospheric Scattering

As light passes through an atmospheric layer, it is partially attenuated by gases and particles in its path. This atmospheric attenuation of radiation arises from the individual or collective effects of

- 1) aerosol absorption.
- 2) molecular absorption.
- 3) aerosol scattering, and
- 4) molecular scattering.

Molecular absorption occurs in several absorption bands and is due to the ability of molecules to go from one vibrational-rotation state to another upon absorbing a photon. By operating in a region of the spectrum with little atmospheric absorption the USU lidar avoids the problem of attenuation by absorption.

Scattering causes a redistribution of the incident radiation energy into all directions, thereby diminishing the energy in the original direction. Aerosol, or Mie, scattering occurs for light waves and particles whose dimensions are of the same order of magnitude (aerosols, dust, clouds). Molecular scattering occurs when light is scattered by particles (molecules, atoms) many times smaller than the incident wavelength and is referred to as Rayleigh scattering.

Molecular scattering and extinction is predicted by Rayleigh theory in which scattering is directly proportional to the product of the atmospheric density and the Rayleigh cross section. Rayleigh scatter is an energy conserving event that results from the displacement of bound electrons of an atom or molecule by the electric field of the incident light. The polarizability of the molecule determines the effective energy level displacement of the electron and thus determines the magnitude of the induced electric dipole. The induced dipole oscillates at the same frequency as the incident radiation, and correspondingly radiates at that frequency. This is the basic premise of the Rayleigh backscatter lidar technique.

The attenuation due to Rayleigh scattering of a transmitted beam traveling through the atmosphere can be described by

$$dl = I_0 \delta \, dh \quad (26)$$

where  $dl$  is the incremental change in intensity,  $I_0$ , over the distance  $dh$ .  $\delta$  is the attenuation or extinction coefficient of the medium given by

$$\delta = \sigma_R \cdot N. \quad (27)$$

Here  $\sigma_R$  is the Rayleigh scattering cross section and  $N$  the molecular number density. Atmospheric transmittance,  $T$ , is a function of height and wavelength and is defined as the fraction of light remaining after traveling from  $h_0$  to  $h$

$$I(\lambda, h) = I_0 T(h, h_0) = I_0 e^{-\int_{h_0}^h \delta(\lambda) dh'} \quad (28)$$

where

$$T(h, h_0) = \exp \left[ - \int_{h_0}^h \delta(\lambda) dh' \right]. \quad (29)$$

The differential Rayleigh scattering cross section gives the probability that a molecule will scatter light, is given in the Rayleigh approximation [Measures, 1988]

$$\frac{\partial \sigma_R}{\partial \Omega} = \frac{\pi^2 \alpha^2}{N \lambda^4} (\cos^2 \varphi \cos^2 \theta + \sin^2 \varphi) [cm^2 sr^{-1}] \quad (30)$$

where  $\alpha$  is the polarizability of the medium,  $\lambda$  the wavelength of incident radiation,  $\theta$  is the angle between incident and scattering direction, and  $\varphi$  is the polarization angle. (Note the characteristic inverse relationship between the Rayleigh scattering coefficient and the fourth power of the wavelength.) The phase function,  $\cos^2 \varphi \cos^2 \theta + \sin^2 \varphi$ , describes the anisotropy of Rayleigh scatter. Setting  $\theta = 180^\circ$ , and integrating Equation 30 over all  $\varphi$  provides the backscatter cross section ( $cm^2$ )

$$\sigma_R^{\pi}(\lambda) = \frac{\pi^2 \alpha^2}{N \lambda^4}. \quad (31)$$

As previously mentioned, the retrieval of temperature requires several assumptions. One such assumption is that Mie scattering is negligible in our calculations. Mie scattering plays a significant role in lidar observations only in the presence of aerosols. Above 35 km, however, the atmosphere is considered to be both aerosol- and cloud-free so that the light backscattered from a laser beam is due to atmospheric molecules. Rayleigh scattering by molecules may be differentiated from Mie scattering by aerosols by making simultaneous observations at different wavelengths. Experiments using two different

wavelengths [Chanin and Hauchecorne, 1981] demonstrated simultaneous density measurements above 30 km to be similar and well within the limits of their respective accuracy. Additionally, Jenkins *et al.* [1987] used lidars at 532 nm and 355 nm nearly 15 months after the 1982 El Chichon volcano erupted in Mexico, and found aerosols were confined below 34 km. For measurements above 35 km, aerosol effects can be considered negligible and thus we can safely neglect Mie scattering.

## 2.2. Lidar Equation

For  $N_0$  photons emitted from a laser pulse, the number of backscattered photons received by a lidar will be proportional to the product of the output power of the laser, the square of the atmospheric transmission of light from the lidar altitude to the scattering altitude, the molecular cross section for Rayleigh backscatter, the physical characteristics of the light-receiving system, and the range-squared corrections. The lidar equation can be written as

$$N(h) = \frac{N_0 A Q T^2(h)}{h^2} \cdot [n(h) \sigma_R^R] \quad (32)$$

$h$  = height above lidar

$N(h)$  = Rayleigh backscattered signal as number of photons per second

$n(h)$  = atmospheric number density at  $h$

$\sigma_R^R$  = Rayleigh backscatter cross section (assumes an average atmospheric cross section for Rayleigh scatter regardless of atmospheric constituents)

$A$  = telescope area

$Q$  = optical efficiency of lidar system

$T(h)$  = atmospheric transmittance between the lidar and  $h$ . The transmittance term enters the equation as a square because the light must pass through the atmosphere twice with attenuation occurring in both directions.

The lidar equation is inverted to give the relative molecular density as a function of altitude in terms of measured quantities [Hauchecorne and Chanin, 1980]. The density is proportional to the range-

squared corrected return signal; thus, for the signal received from altitude  $h$  due to Rayleigh backscatter only, we have

$$n(h) = \frac{C(\lambda)}{T(h, \lambda)^2 \sigma_R(\lambda)} N(h) h^2. \quad (33)$$

where  $N$  is the return signal and  $C$  a system calibration constant (i.e.,  $C = N_o A Q$ ). We assume the transmittance to be constant for our range of interest based on calculations by *Hauchecorne and Chanin* [1980] who reported variations of only 0.4% in transmittance between 35 and 90 km at 532 nm when taking into account ozone absorption and molecular extinction. Due to the lack of an absolute calibration of the atmospheric transmission as a function of time and other constants, the density profile is relative, and thus we have a very straightforward determination of the relative density. In order to obtain an absolute density profile, we must fit the relative profile to either a theoretical model or other experimental data.

### 2.3. Temperature Algorithm

The temperature is derived by integrating the relative density profile downward [*Gardner*, 1989] beginning at the maximum altitude of interest and under the assumption that the atmosphere is an ideal gas in hydrostatic equilibrium. The assumption of hydrostatic equilibrium may not be true locally in strong turbulent layers; however, taking into account sufficient time and spatial integration of the lidar measurement, such a hypothesis is reasonable. *Jenkins et al.* [1987] have shown that even with large amplitude waves (~20 K), the error in the wave component does not constitute a significant source of error.

Under hydrostatic conditions, in which vertical acceleration of air parcels is negligible, one may combine the ideal gas law,  $P = n k T$ , with the hydrostatic equation,

$$\frac{dP}{dh} = -m(h)g(h)n(h) \quad (34)$$

where  $n$  is the number density at  $h$ ,  $m$  is the mean molecular mass, and  $k$  is Boltzman's constant. The resulting equation can be integrated to find the temperature change between altitudes  $h_1$  and  $h_2$

$$k [n(h_2) T(h_2) - n(h_1) T(h_1)] = - \int_{h_1}^{h_2} m(h) g(h) n(h) dh \quad (35)$$

and rewritten to solve for  $T$

$$T(h_1) = T(h_2) \frac{n(h_2)}{n(h_1)} + \frac{1}{k n(h_1)} \int_{h_1}^{h_2} m(h') g(h') n(h') dh' \quad (36)$$

This expression requires knowledge of the absolute density at the incremental altitudes  $h'$ . Left in this form, any error in the reference density profile will propagate through the inversion calculation, potentially diverging with the ratio  $n(h_2)/n(h_1)$ . However, if the uppermost reference altitude is  $h_{\max}$  and we integrate to a lower altitude  $h$  over the range  $h'$ , we get

$$T(h) = \frac{n(h_{\max})}{n(h)} T(h_{\max}) + \frac{1}{k} \frac{n(h_{\max})}{n(h)} \left( \int_h^{h_{\max}} m(h') g(h') \frac{n(h')}{n(h_{\max})} dh' \right) \quad (37)$$

where the integrand has been multiplied and divided by  $n(h_{\max})$ . In this form, any system or model-dependent parameters of density divide out of the temperature calculation. The fact that the density measurement is relative, the temperature derived from it, which depends only upon the variation of density with altitude, is absolute, thus making exact density calibration unnecessary.

The equation is initialized with a temperature, normally estimated from a model or other observation(s), at the top altitude. The top altitude is normally chosen as the highest altitude from which there is a good lidar signal. We fixed the top altitude to be the height at which the signal is equivalent to 16 standard deviations.

### 3. Systematic Errors

The goal of the lidar measurements is to get very accurate temperatures that extend over a large altitude range. We want to have confidence in the data and, at the same time, optimize the collection capability of the lidar.

The accuracy of the measurement is improved by eliminating *systematic errors* arising from the data reduction method or instrumentation problems, such as pulse overlapping and saturation in the PMT. Several assumptions, in addition to the standard hydrostatic balance for an ideal gas, are inherent in the development of Equation 37. Because of its significance to the rest of the scientific analyses, we closely scrutinized the temperature reduction technique and considered several factors that may produce individual errors, albeit small ones, in which the overall accumulated error would invalidate comparisons with other techniques. These factors include 1) the effect of evolving atmospheric composition with altitude, 2) the value of gravity,  $g$ , and its altitude dependence, 3) numerical integration technique, 4) the evaluation of the background signal level, 5) the evaluation of the analytical uncertainty for a temporally and spatially averaged signal, and 6) the requisite value of the standard deviation to signal ratio for starting the temperature integration. Several potential systematic errors of between 0.5 and 3 K (0.2–1%) were identified and eliminated or reduced to a negligible level below 0.1 K. These are discussed below.

### 3.1. Vertical Variation of $m$

It was originally accepted that mean molecular mass ( $m$ ) could be treated as constant in our calculations. While justified for heights up to 80 km, at higher altitudes dissociation of  $O_2$  by solar radiation and downward eddy diffusion of atomic oxygen, (O), causes mixing ratios to vary. Actually, based on the MSISE90 [Hedin, 1991] reference atmosphere, the total  $m$  begins to slowly decrease between 60–80 km. The significant reductions (>1%) in  $m$  from 40 to 90 km and approaching 10% reduction by 120 km must be accounted for.

Returning to the lidar equation, we note that the measured photon signal is proportional to the atmospheric density by a height independent constant scaled by  $r^2$ . Included within this calibration constant is the Rayleigh backscatter coefficient,  $\sigma_R^\pi$ , which depends not only on the laser wavelength [Gardner, 1989], but more importantly, on the specific scatterer(s) themselves.



Rather than use a constant value for the scattering cross section,  $\sigma_R^\pi$ , we chose to evaluate it as  $\sigma_R^\pi = \sigma_R^\pi(h)$ . This requires the characterization of  $\sigma_R^\pi(\text{O})$ ,  $\sigma_R^\pi(\text{O}_2)$ ,  $\sigma_R^\pi(\text{N}_2)$ , and  $\sigma_R^\pi(\text{Ar})$  at the appropriate wavelength,  $\lambda$ , in order to get an expression for a weighted  $\sigma_R^\pi(\lambda, h)$ . Before deriving this function, we first had to calculate the correct values of  $\sigma_R^\pi$  for the primary atmospheric constituents. *Tohmatsu* [1990] listed Rayleigh scatter values for  $\sigma_R(\text{O})$ ,  $\sigma_R(\text{O}_2)$ ,  $\sigma_R(\text{N}_2)$ , and  $\sigma_R(\text{Ar})$  at  $\lambda=589.3\mu\text{m}$ . With little difficulty, one can convert Rayleigh scatter coefficients,  $\sigma_R(589.3\mu\text{m})$ , to Rayleigh backscatter coefficients,  $\sigma_R^\pi(532.0\mu\text{m})$ , i.e.,

$$\sigma_R^\pi(\lambda') = \frac{3}{8\pi} \sigma_R(\lambda) \left( \frac{\lambda}{\lambda'} \right)^4. \quad (38)$$

Thus we obtained the following values ( $\lambda'=532\mu\text{m}$ ):

$$\begin{aligned} \sigma_R^\pi(\text{O}) &= 8.64 \times 10^{-29} \\ \sigma_R^\pi(\text{Ar}) &= 4.54 \times 10^{-28} \\ \sigma_R^\pi(\text{O}_2) &= 4.10 \times 10^{-28} \\ \sigma_R^\pi(\text{N}_2) &= 4.83 \times 10^{-28}. \end{aligned}$$

Treating the Rayleigh backscatter coefficient separately from the constant,  $C$ , in the lidar equation, the relation between photocounts ( $N$ ) and density ( $n$ ) becomes

$$n(h) \propto \frac{N(h)h^2}{\langle \sigma_R^\pi \rangle} \quad (39)$$

where  $\langle \sigma_R^\pi \rangle$  is a constituent weighted height and wavelength dependent mean cross section for Rayleigh backscatter evaluated as

$$\langle \sigma_R^\pi \rangle(h) = \frac{\sum n_i(h) \sigma_R^\pi(i)}{\sum n_i(h)} \quad (40)$$

where  $n_i$  is the number density of constituent  $i$  (i.e., O, O<sub>2</sub>, N<sub>2</sub>, and Ar), at  $h$ , as specified in the MSISE90.

Similarly, the vertical variation of the mean molecular mass,  $m$ , may affect the temperature calculation. Although assuming a constant  $m$  results in considerable simplification of the temperature algorithm, a height-dependent  $m$  that decreased with increasing altitude effectively decreases the calculated temperature. Therefore, we set  $m=m(h)$  as,

$$m(h) = \frac{\sum n_i(h) m_i}{\sum n_i(h)} \quad (41)$$

Figure 7 illustrates the consequence of treating the composition as a function of altitude on the temperature profiles. The first plot has incorporated an adjustment for the variable composition in the temperature integral only, the second in the Rayleigh backscatter term only, and the third plot incorporates the variable  $m$  in both terms. The two actions have opposite effects on the temperature profiles. The reduction in cross section increases temperatures up to 3 K in the top 5–10 km of the temperature profile, becoming negligible after 20 km from the top. The decrease in  $m$  reduces the temperatures by almost 1.5 K in the top 5 km and becomes negligible after 15 km. Thus the combined effect introduces a  $\delta T \approx 1.0$ –2.0 K or roughly  $\sim 0.6$ –0.7% within the upper 5 km level. Most of the major atmospheric constituents appear in constant ratios throughout the lower and middle atmosphere, which minimizes the consequences of assuming a constant  $m$ ; however, this variation becomes more important as lidar instruments (e.g., Purple Crow, ALOMAR, ALO) become capable of reaching greater heights in the thermosphere. For accurate temperature profiles extending above 85 km, the height dependence of  $m$  must be considered.

### 3.2. Gravitational Acceleration

The gravity term used in the integration is corrected to 1500 m from a sea level value using an effective earth radius for Logan, UT, thereby allowing proper temperature and density comparisons with profiles from models and other sites. The method used in determining the gravitational term,  $g$ , is described below.

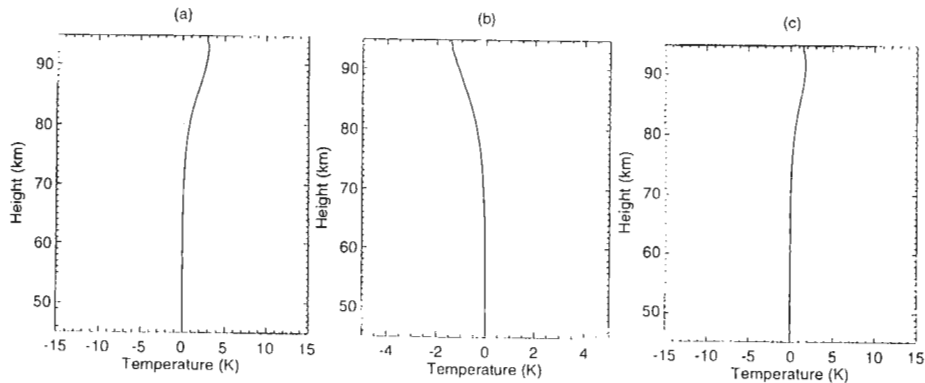


**Figure 7.** The difference in temperature as a function of height for three separate situations. a) A plot of the difference between a temperature profile incorporating a height dependent mean molecular mass and one without, b) the difference when the variation of  $m$  is accounted for in the backscatter ratio only, c) the difference when one plot fully incorporates the altitude variation of  $m$  in both backscatter and mean mass.

True gravity (that due to the earth's mass) falls off inversely with range squared so that

$$g(h) = g_o \frac{r^2}{(r+h)^2} \quad (42)$$

where  $r$  is the earth's radius,  $h$  is the elevation above sea level, and  $g_o$  is the gravitational constant at  $h=0$ .

The effects of rotation modify this true gravity into an apparent gravitational force. Thus the equation for gravitational acceleration,  $g$ , that we measure on a body of mass  $m$ , including centrifugal effects is

$$\vec{g}(h) = \vec{g}_m \frac{r^2}{(r+h)^2} - \vec{\Omega} \times [\vec{\Omega} \times (\vec{r} + \vec{h})] = \vec{g}_m(h) + \vec{g}_c(h) \quad (43)$$

where

$r$  = vector radius of the earth pointing radially outward

$h$  = altitude above sea level whose vector is parallel to  $r$

$g_m$  = gravitational acceleration due to mass and points radially inward

$g_c$  = correction to  $g_m$  due to rotation and points outward perpendicular to the axis of rotation

$\Omega$  = earth's angular velocity ( $7.292 \times 10^{-5} \text{ sec}^{-1}$ ).

The centrifugal acceleration term effectively reduces  $g$  and increases proportionally with range. To get the magnitude of  $g(h)$ , we must use  $g_m$  and  $g_c$ . To get  $g_m$ , we first find the observed value at Logan, reduce this value to sea-level, then remove the centrifugal force dependence.

The standard value of  $g$  at  $45^\circ \text{ N}$  reduced to sea level (including the effect of centrifugal acceleration) adapted by the International Committee on Weights and Measures in 1901 is  $g = 9.80665 \text{ m/sec}^2$  [Halliday and Resnick, 1960]. However, this value varies from approximately  $9.78032 \text{ m/s}^2$  at the equator to  $9.83219 \text{ m/s}^2$  at the pole, [World Geodetic System 1984 model incorporating ground-based and satellite observations of  $g$ ; Rick Blakely, USGS, Menlo Park, private communication, March 1995.]

In order to keep errors in deduced temperatures to less than  $0.1 \text{ K}$ , we should keep errors in  $g$  below  $0.005 \text{ m/s}^2$ . The best local value of  $g$  comes from the Cache County Courthouse [Bob Oaks, Geology Dept., USU, private communication, March 1995]. The USGS has established the value at

41.7347 N, 111.8353 W, 1382 m (asl) as  $9.798312 \text{ m/s}^2$ . Translated to sea level, this gives a value for  $g$  of  $9.802565 \text{ m/s}^2$ .

The magnitude of  $g(h)$  given by

$$g^2 = g_m^2 + g_c^2 - 2g_m g_c \cos \lambda \quad (44)$$

can be solved for  $g_m$  using the quadratic formula

$$g_m = g_c \cos \lambda + \sqrt{g^2 - g_c^2 \sin^2 \lambda} \quad (45)$$

whereby we find  $g_m = 9.82140 \text{ m/s}^2$  for the sea level value at Logan. Now it is possible to determine the altitude dependence of the magnitude of  $g(h)$

$$g(h) = \sqrt{g_m^2(h) + g_c^2(h) - 2g_m(h)g_c(h)\cos\lambda} \quad (46)$$

where

$$g_m(h) = g_m \frac{r^2}{(r+h)^2} \quad (47)$$

$$g_c(h) = \Omega^2 (r+h) \cos^2 \lambda \quad (48)$$

When comparing the results of Equation 48 to those of the simplified formulation of Equation 42, we find the effect of the difference to be insignificant. For hydrostatic equilibrium, we are interested in the magnitude of  $g$  in the radial direction, not the total magnitude. The radial component  $g_r$  is given by

$$g_r(h) = g_m(h) - g_c(h) \cos \lambda. \quad (49)$$

At sea level  $g_r = 9.80255 \text{ m/s}^2$ . When compared to the previous methods (Equations 42 and 43) using only the  $r^2/(r+h)^2$  falloff or the combined effects of  $r^2/(r+h)^2$  and rotation, we discover that the radial component value  $g_r(h)$  is just slightly smaller than the vector magnitude  $g(h)$ . While the first calculation is the simplest, the second method is more accurate as it takes into account the centrifugal acceleration. It suffers, however, in that it is the magnitude of the total gravitational acceleration vector, which is not completely radial. The third method,  $g_r(h)$ , is the most accurate for the data reduction. It takes into account the centrifugal acceleration and is radial. We have used Equation 49 with the above value for  $g_r$ .

and the Clarke spheroid of 1866 for determination of  $r = 6368.67$  km for USU in our temperature algorithm.

The pole to equator effect of latitudinal (for both radius and centrifugal acceleration) on gravity,  $g$ , and hence, the temperature profile is shown in Figure 8. Because the integration starts at  $z_{max}$  with a given temperature, there is no error at the top of the profile. However, the error quickly accumulates as one continues the integration downward, leading to a slight difference ( $\delta T \approx 1.0$ – $2.0$  K) within the stratosphere.

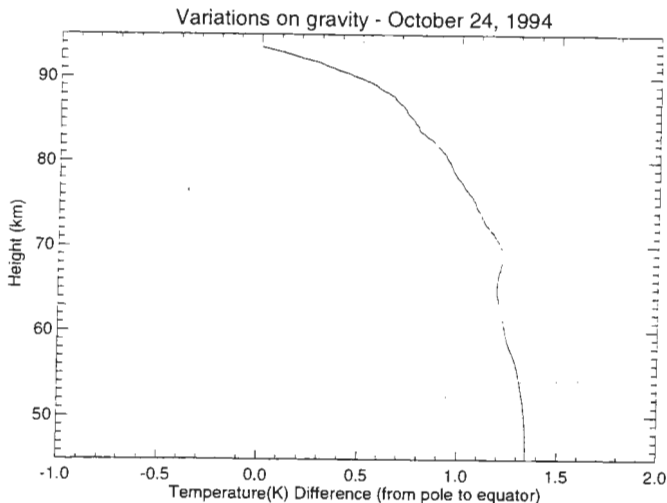


**Figure 8.** The difference between two temperature profiles illustrating the pole to equator latitudinal variation of gravity.

### 3.3 Initialization Temperature

The accuracy, especially at the highest altitudes, is affected by the estimate of the initial temperature. If the estimate is not good, then its influence in the integration will persist to lower altitudes. This can be illustrated as follows: For an exponential decay in atmospheric density with height,

$$n_{\max} = n e^{-(h_{\max} - h)/H} \quad (50)$$

then

$$\frac{n_{\max}}{n} = e^{(h_{\max} - h)/H} \quad (51)$$

and the greater the distance between  $h_{\max}$  and  $h$ , the smaller the ratio  $n_{\max}/n$ . By the time the integration proceeds downward by one scale height,  $H$  ( $\sim 7$  km), this factor is 0.38. For  $2H$  (14 km), it is 0.14 and by  $3H$  (21 km) it is 0.05. Suppose the initial temperature at 90 km is 210 K but the estimate is 200 K, then based on the preceding example, the contributing error, on average, is

$$\Delta T = 3.7 \text{ K at } 1H (\sim 83 \text{ km})$$

$$\Delta T = 1.4 \text{ K at } 2H (\sim 76 \text{ km})$$

$$\Delta T = 0.5 \text{ K at } 3H (\sim 69 \text{ km})$$

$$\Delta T = 0.2 \text{ K at } 4H (\sim 62 \text{ km}).$$

To minimize this bias, we want to choose a "good" set of initial values. In this study, involving mostly long-term averages, a "good" set of initial values would come from either a model or an independent long-term average from the same region. Early on, the MSISE90 model provided our initial upper temperature value. However, during some periods, especially winter, our temperatures rapidly increased with decreasing altitude for the top several kilometers, unlike the model, indicating that the initial values were too low and actual temperatures in this region were probably warmer than MSISE90 indicated. This disagreement with MSISE90 was also observed in sodium (Na) lidar temperature measurements at Fort Collins and Urbana, IL [Senft *et al.*, 1994; Yu and She, 1995]. The fact that our temperature profiles were more similar to Na lidar observations at Ft. Collins than to MSISE90 led to the

development of an initial-value model in which the initial temperature values  $T(h_{\text{max}})$  for the integration are based on the Na lidar temperatures of *Yu and She* [1995]. These values are modified using the temporal and altitude variations in MSIS90 to account for the day of the month, the mid time of the night's observation, and the maximum altitude (if it is below 83 km).  $k$  is Boltzmann's constant.

The initial-value temperature model is normalized to the monthly temperature variation observed at Ft. Collins and the diurnal time dependence in MSIS90. Temperature profiles representing the mean value at midnight on the 15th of the month are obtained using Ft. Collins mean monthly temperatures, which were averaged over a 4-hour period centered at 0700 UT (local midnight) and recorded every kilometer from 81–83 to 105 km [*She et al.*, 1995]. By fitting the monthly values at a given altitude with a cubic spline, we can estimate the profile for a particular day. Because the Ft. Collins data were reported every kilometer, we interpolate the data linearly for the altitude of interest. This provides an initial value for a given day and height at local midnight. To determine the diurnal variation between midnight and the local time of our observation, the MSIS90 is used as it imposes a significant semidiurnal tidal variation at these altitudes. In circumstances where our signal was good enough to extend beyond 105 km, or not strong enough to produce a profile above 81 km, we would rely solely on MSIS90 for the initial temperature. Once we have a value for the correct day and altitude, we use the MSIS90 to determine the difference between midnight and the center time of our observation and add (subtract) this value to the initialization temperature. This is sometimes as large as 5 to 10 K. The final result is used as the top temperature for the hourly profiles. This model is illustrated in Figure 9. However, for a study involving much shorter time scales, this set of initial values would tend to mask the influence of waves that should otherwise be detectable.

#### 3.4. Background

Superposed with the Rayleigh backscatter signal is the background signal—from the dark count of the photomultiplier tube and unwanted ambient sky light such as airglow, starlight, moonlight,



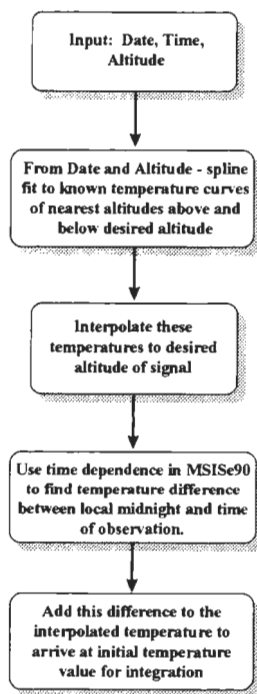


Figure 9. Determination of initial temperature

scattered city lights—that has to be subtracted from the observed signal to obtain the true backscattered signal. While attempts have been made to reduce the background by running only at night, inserting narrow filters, and cooling the PMT, any remaining unwanted signal must be accurately characterized. We found that considerable attention has to be paid to this noise level to ensure an accurate measurement. This becomes crucial in the higher altitudes where the signal to  $\sigma$  ratio drops to  $\leq 16$ .

To estimate the background noise level one averages the photocounts above the altitude where the backscattered signal is considered negligible. This background, derived from the full altitude region through which the background level was stable and constant, is then subtracted from the hourly and all-night photocount profiles. It is best to average this background over as many range gates as possible in order to provide a precise estimate of the noise. This range was usually between 100 and 500 km, but occasionally a smaller region was used near 100–150 km due to nonlinearities in the background levels above.

The monthly profile can be determined in two ways. One way is to sum the total photocounts for every collection and derive a single monthly profile; the second method is to calculate nightly profiles, then average these into one monthly profile. In order to extend temperature profiles for the monthly and seasonal averages to higher altitudes, the summation of all photocounts is the best method. This effectively raises the altitude for which the signal to *sigma* ratio approaches 16 and one obtains a greater profile. However, this method, based on an assumed constant background, was not always satisfactory and caused significant problems in the estimation of the background level during certain months.

In Figure 10 we see temperatures from two months in 1994, both of which show profiles calculated by the two methods. March included 12 nights of observations and August included 11 nights. The results clearly demonstrate the higher altitudes achieved by the summation method. In March, the two profiles are quite similar up to 80 km, 5 km down from the top for the averaged profile and 10 km down for the summed profile. However, during August, the similarity is not accomplished until 65 km. Temperatures from the summation of the photons are much warmer in the upper portion of the profile, indicating an underestimation of the density. This is most likely a result of removing an overestimated background from the raw data. A possible explanation is a slightly increasing noise level in the higher range gates. Sometimes this existed; sometimes it did not. It was much greater in other PMTs that we tried to use. For this research, the monthly and seasonal averages were accomplished by averaging the nightly profiles (usually 4–8 hours) for the period. While this approach results in a shorter profile, it is

less sensitive to the background values. Therefore, we have used this more conservative approach and produced 1-hour and nightly profiles by averaging the photocounts for the whole period and deriving the temperatures, while average monthly and seasonal profiles were obtained by averaging the individual nights for the period. In addition to the factors discussed previously, the electronic gate has to be turned on at a high-enough altitude that the PMT is not greatly overloaded. Otherwise, in addition to affecting the linearity of this low-altitude signal, it affects the accuracy with which the background signal can be measured.

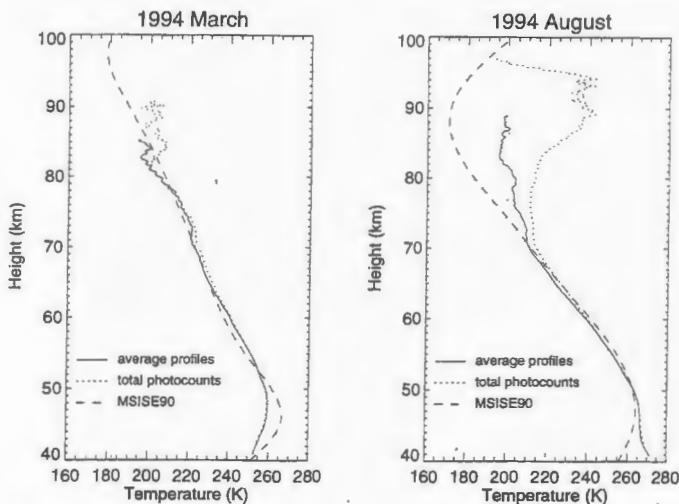


**Figure 10.** Example of the difference between monthly profile derived from summed photocounts vs. that derived from averaged nightly profiles. While the difference for March is within the signal error at the top of the profile, the profile for August is obviously outside the error.

#### 4. Statistical Uncertainty

It is obviously better to be 20 km above than 10 km, which is one reason we cooled the PMT, used a 0.5 nm interference filter, and worried about the effect of changing neutral composition at our highest altitudes. Another way to improve the accuracy at a particular altitude is to optimize the data acquisition and increase the temporal and spatial averaging so that  $h_{\max}$  could be raised as high as possible. *Statistical uncertainty* or precision of the signal is based on Poisson statistics and photocounting, in which the standard deviation is equal to the square root of the number of photocounts, i.e.,  $\sqrt{S+N}$ . The total signal detected and recorded is  $S+N$  where  $S$  is the backscattered signal to be used in calculations and  $N$  is the background signal or noise. A more representative approach is to let  $S=(S+N)-N$ . If we want the backscattered signal  $S$  averaged over  $J$  range gates and  $I$  time intervals, and our background noise averaged over  $K$  range gates (where  $K$  is not necessarily equal to  $J$ ) and the same  $I$  time intervals, the observed signal becomes

$$S_j = \frac{1}{I} \sum_{i=1}^I (S+N)_{ij} - \frac{1}{K} \sum_{k=1}^K N_{kj} = (S+N)_j - N_j. \quad (52)$$

where  $j$  is time,  $i$  and  $k$  the range gate of the combined signal plus noise and background, respectively.

The background is determined over different spatial ranges than the signal and the dependence of a variation in  $N_j$  on the independent  $N_{kj}$  is given by

$$dN_j = \sum_{k=1}^K \frac{\partial N_j}{\partial N_{kj}} dN_{kj} = \frac{1}{K} \sum_{k=1}^K dN_{kj} \quad (53)$$

From which it follows [defining  $\sigma_x^2 = \langle dx \rangle^2$ ] that

$$\sigma_{N_j}^2 = \frac{1}{K^2} \left( \sum_{k=1}^K \sigma_{N_{kj}}^2 \right) = \frac{\sigma_N^2}{K}. \quad (54)$$

The dependence of a variation in  $(S+N)_j$  on the independent  $(S+N)_{ij}$  is given by

$$d(S+N)_j = \sum_{i=1}^I \frac{\partial (S+N)_j}{\partial (S+N)_{ij}} d(S+N)_{ij} = \frac{1}{I} \sum_{i=1}^I d(S+N)_{ij}. \quad (55)$$

From which it follows that

$$\sigma_{(S+N)_y}^2 = \frac{1}{J^2} \sum_i \sigma_{(S+N)_{ij}}^2. \quad (56)$$

Because the observations of  $(S+N)_{ij}$  and  $N_j$  are independent, it follows that the variance of the signal  $S_j$  is given by

$$\sigma_{S_j}^2 = \sigma_{(S+N)_j}^2 + \sigma_{N_j}^2 \quad (57)$$

or in more detail

$$\sigma_{S_j}^2 = \frac{1}{J^2} \sum_{i=1}^J \sigma_{(S+N)_{ij}}^2 + \frac{1}{K^2} \sum_{k=1}^K \sigma_{N_{kj}}^2. \quad (58)$$

For Poisson statistics where the variance is equal to the number of counts, the variance of the signal at time  $j$ , averaged over the altitude range represented by  $i=1-I$ , is

$$\sigma_{S_j}^2 = \frac{1}{J^2} \sum_{i=1}^J \langle (S+N)_{ij} \rangle + \frac{1}{K^2} \sum_{k=1}^K \langle N_{kj} \rangle = \frac{1}{J} \langle (S+N)_j \rangle + \frac{1}{J} \langle N_j \rangle \quad (59)$$

where the spatial averages for the signal and noise have been introduced

$$\langle (S+N)_j \rangle = \frac{1}{J} \sum_{i=1}^J \langle (S+N)_{ij} \rangle, \quad (60)$$

$$\langle N_j \rangle = \frac{1}{K} \sum_{k=1}^K N_{kj}. \quad (61)$$

A temporal average is handled in the same way as the spatial. The averages from  $j=1-J$  are given by

$$\langle \overline{S+N} \rangle = \frac{1}{J} \frac{1}{I} \sum_{j=1}^J \sum_{i=1}^I \langle (S+N)_{ij} \rangle, \quad (62)$$

$$\langle \overline{N} \rangle = \frac{1}{J} \frac{1}{K} \sum_{j=1}^J \sum_{k=1}^K N_{kj}. \quad (63)$$

And the signal is  $\langle \overline{S} \rangle = \langle \overline{S+N} \rangle - \langle \overline{N} \rangle$ .

The variances are

$$\sigma_{\overline{S+N}}^2 = \frac{1}{JI} \langle \overline{S+N} \rangle \quad (64)$$

$$\sigma_{\langle N \rangle}^2 = \frac{1}{JK} \langle N \rangle. \quad (65)$$

Accordingly, the variance for the spatially and temporally averaged signal becomes

$$\sigma_{\langle \bar{S} \rangle}^2 = \sigma_{\langle \bar{S} + N \rangle}^2 + \sigma_{\langle N \rangle}^2 = \frac{1}{J} \frac{1}{I} \langle \bar{S} + N \rangle + \frac{1}{J} \frac{1}{K} \langle N \rangle. \quad (66)$$

Another quantity that we often need is the signal in terms of the standard deviation,

$$\frac{\langle \bar{S} \rangle}{\sigma_{\langle \bar{S} \rangle}} = \frac{\langle \bar{S} + N \rangle - \langle N \rangle}{\sqrt{\frac{1}{IJ} \langle \bar{S} + N \rangle + \frac{1}{KJ} \langle N \rangle}}. \quad (67)$$

For instance, the temperature integration begins at the highest altitude for which the signal is equal to 16 standard deviations. At the peak of the layer,  $S \gg N$ , and

$$\frac{\langle \bar{S} \rangle}{\sigma_{\langle \bar{S} \rangle}} = \sqrt{IJ \langle \bar{S} + N \rangle - \langle N \rangle}. \quad (68)$$

As  $S$  becomes smaller, other terms begin appearing and we get the full expression.

The uncertainty is reduced as the temporal integrations or spatial averages are increased.

Oftentimes the density profile, and consequently the temperature profile, is resolved to a 1-hour or all-night (up to 12 hours during winter) time integral with a 3 km (27 point) height resolution while the background noise is determined from an altitude range of ~ 250 km (provides very large K).

The uncertainty of the signal decreases rapidly from the highest altitude downward such that lower mesospheric and stratospheric temperatures are very precise. While not obvious, this aspect is easily demonstrated with the calculation of the temperature uncertainty. The temperature uncertainty is derived analytically from Equation 37 by propagating the uncertainty in the photocounts. Recall that the temperature is given as the sum of two terms, one of which requires an estimate of the uppermost point:

$$T(h) = T(h_{\max}) \frac{n(h_{\max})}{n(h)} + \frac{mg}{kn(h)} \int_h^{h_{\max}} n(h') dh'. \quad (69)$$

This ultimately leads to the appearance of two terms in the temperature uncertainty. By following the derivation of *Gardner* [1989], we find that the uncertainty yields

$$dT = \frac{\partial T}{\partial T_{\max}} dT_{\max} + \frac{\partial T}{\partial n_{\max}} dn_{\max} + \frac{\partial T}{\partial n} dn =$$

$$\frac{n_{\max}}{n(h)} dT_{\max} + \frac{T_{\max}}{n(h)} dn_{\max} - \left( \frac{T_{\max} n_{\max}}{n(h)} + \frac{mg}{kn(h)} \int_h^{h_{\max}} n(h') dh' \right) \frac{dn}{n(h)} + \frac{mg}{kn} \frac{\partial}{\partial n} \left( \int_h^{h_{\max}} n(h') dh' \right) dn$$
(70)

where the value in the parenthesis returns  $T(h)$ . Looking at the last term on the right, we let  $c=mg/k$ , getting

$$\frac{c}{n} \frac{\partial}{\partial n} \left( \int_h^{h_{\max}} n(h') dh' \right) dn.$$
(71)

If  $\partial/\partial n = d/dn$  (as there is only one variable), then  $dn = (dn/dh) dh$ , and  $dn/dh = -(n/H)$ . Equation 71 reduces to

$$\frac{c}{n} \left[ n(h_{\max}) \frac{dh_{\max}}{dn} - n(h) \frac{dh}{dn} \right] = -\frac{c}{n} \left[ n(h_{\max}) \frac{H_{\max}}{n(h_{\max})} - n(h) \frac{H}{n(h)} \right] = -\frac{c}{n} [H_{\max} - H].$$
(72)

This term is 0 for a constant scale height,  $H$ .

Therefore, the temperature variance is

$$\sigma_T^2 = \left[ \frac{n_{\max}}{n(h)} \right]^2 \sigma_{T_{\max}}^2 + \left[ \frac{T_{\max}}{n(h)} \right]^2 \sigma_{n_{\max}}^2 + \left[ \frac{T(h)}{n(h)} \right]^2 \sigma_n^2$$
(73)

which can be rearranged as

$$\sigma_T^2 = T^2 \left( \frac{\sigma_n}{n} \right)^2 + \left( \frac{n_{\max}}{n} \right)^2 \sigma_{T_{\max}}^2 + \left( \frac{T_{\max}}{n} \right)^2 \sigma_{n_{\max}}^2.$$
(74)

If the number density  $n$  increases with decreasing altitude by scale height  $H$ , i.e.,

$$n = n_{\max} e^{(h_{\max}-h)/H},$$
(75)

then

$$\sigma_T^2 = T^2 \left( \frac{\sigma_n}{n} \right)^2 + \left[ \sigma_{T_{\max}}^2 + T_{\max}^2 \left( \frac{\sigma_{n_{\max}}}{n_{\max}} \right)^2 \right] e^{-2(h_{\max} - h)/H} \quad (76)$$

where  $T$  and  $n$  are the temperature and number density at  $h$ , and  $T_m$  and  $n_m$  are the temperature and number density at the top altitude,  $h_m$ , and  $H$  is the atmospheric scale height which we have assumed to be constant at 7 km. The first term is the expected relationship following the ideal gas law, i.e.,  $\sigma_T/T = \sigma_n/n \equiv \sigma_p/p$ . Beyond this expected relation, there is a second term based on the estimate and uncertainty of the uppermost temperature that decreases exponentially with the scale height. The middle term on the right is the error of the initialization temperature,  $\sigma_{T_m}$ , and is difficult to evaluate. Because it decreases rapidly as the integration evolves downward, it is not very important at lower altitudes. If we further assume that our initial temperature model is very accurate, we can safely ignore this term.

In addition to the precision of the temperature averages, arising from Poisson statistics from the photocounts, there is variability that arises from the day-to-day variability of the atmosphere itself. This geophysical variability is estimated in the usual way

$$s_{GP} = \sqrt{\frac{\sum_{n=1}^N (T_n - \langle T \rangle)^2}{N-1}}. \quad (77)$$

If there were no geophysical variation, then  $s_{GP}$  would in the limit approach  $s_{(T)}$ . However, the atmosphere does vary with the result that  $s_{GP}$  is greater than  $s_{(T)}$ , but the amount by which it is bigger varies with season and altitude. It should increase with altitude because both  $s_T$  and wave amplitudes for long period gravity waves, tides, and planetary waves increase with altitude, and  $N$  decreases at the highest altitudes. This is generally what is seen, except at the very top where  $s_{GP}$  is artificially reduced because many of the profiles have almost the same  $h_{\max}$  and hence  $T(h_{\max})$ . A minimum or relative minimum occurs much of the time between 50 and 60 km. In summer it is the order of 2 K and extends down to the lowest altitude.



As a final note, validation of the data-reduction algorithm was performed with a simple simulation. A density profile was constructed from the MSISe90 model and range squared corrections were introduced into the densities to form a constant-composition photocount profile. Our data-reduction program was run using this fabricated photocount profile and a starting altitude of 90 km. Doing this we retrieved the MSISe90 temperature profile corresponding to the original MSISe90 density profile.

## 5. Observations

The results presented in this dissertation are from data collected by the USU Rayleigh lidar starting in the fall of 1993 at Logan, UT (41.75° N, 111.80°W) in the 40–90 km range. The low altitude was finally set at 43 to eliminate variability in the signal as the PMT gain is switched on near 35 km. The top altitude was determined by the unacceptably low signal-to-noise ratio. While this altitude averaged near 90 km, on some nights an acceptable S/N was recovered up to 100 km. The numbers of nights and hours per month included in the analysis are given in Table 2. Observations were restricted to cloud-free periods during nighttime. Temperature results and comparisons with other lidars are presented in the next chapter.

**Table 2.** Observation Summary

Month	Nights	Hours
January	17	159
February	15	134
March	25	150
April	4	24
May	3	13
June	6	26
July	7	36
August	12	55
September	25	163
October	10	79
November	6	35
December	8	57

## CHAPTER 5

## MESOSPHERIC TEMPERATURE PROFILES

## 1. Introduction

In this chapter, extensive temperature results obtained from a Rayleigh-scatter lidar [Wickwar *et al.*, 1997a] situated in the middle of the Rocky Mountains, in northern Utah, are reported. The monthly mean temperatures are given in Table 3 at 3 km intervals and are displayed as solid curves in Figure 11 at 112.5 m intervals, but smoothed over a 3.0 km range. The following section is concerned with comparisons of mid-latitude temperature profiles. The next one compares mid-latitude and high-latitude temperature profiles. Our conclusions are presented in the final section.

## 2. Mid-Latitude Comparisons

Few independent sources of averaged temperature profiles exist for comparison purposes. A major one is the MSISE90 model [Hedin, 1991]—an empirical model providing global coverage. We will

Table 3. Monthly Averaged Temperatures Above USU (K)

Ht.	Jan	Feb	Mar	Apr	May	Jun	Jul	Aug	Sep	Oct	Nov	Dec
43.	252.4	264.2	262.0	260.6	270.5	270.8	270.6	267.0	260.7	254.0	242.8	250.5
46.	251.8	259.8	261.9	263.5	270.5	271.2	271.3	265.7	262.5	256.2	248.2	254.6
49.	250.7	255.6	260.2	264.4	271.8	269.2	268.6	264.2	262.0	255.9	249.4	258.6
52.	246.3	251.7	256.3	262.0	269.3	265.2	264.5	258.9	258.8	253.4	249.4	256.8
55.	240.2	246.7	250.9	254.0	265.2	258.9	257.1	252.5	252.7	248.8	247.0	249.5
58.	232.5	241.2	244.2	247.6	256.6	250.4	249.0	244.5	244.9	243.0	243.4	240.2
61.	224.4	235.5	238.7	241.0	245.7	240.8	241.2	236.3	236.6	237.5	241.9	234.5
64.	220.0	230.6	232.5	235.3	234.9	227.5	229.9	226.9	227.4	233.8	238.6	229.9
67.	221.3	230.7	227.7	229.2	222.5	215.8	217.0	218.7	218.6	231.5	235.4	227.8
70.	223.8	233.4	226.5	225.15	213.8	202.6	205.2	211.0	213.2	229.0	230.6	230.4
73.	227.2	233.5	225.1	217.9	207.2	194.9	194.0	208.8	209.0	224.5	222.4	231.0
76.	228.3	225.9	219.8	210.5	200.0	187.7	184.6	203.1	207.1	217.2	219.2	231.8
79.	229.8	217.6	211.8	200.4	192.7	180.8	180.9	203.2	207.7	210.6	212.6	229.6
82.	224.4	214.0	204.4	194.6	187.2	177.5	181.2	197.7	210.2	209.4	209.4	221.2
85.	226.8	206.1	198.3	193.4	181.6		179.2	197.9	211.5	208.6		220.8
88.		209.9		205.1			185.2	198.2		211.0		216.7
91.		207.8		202.4						212.2		

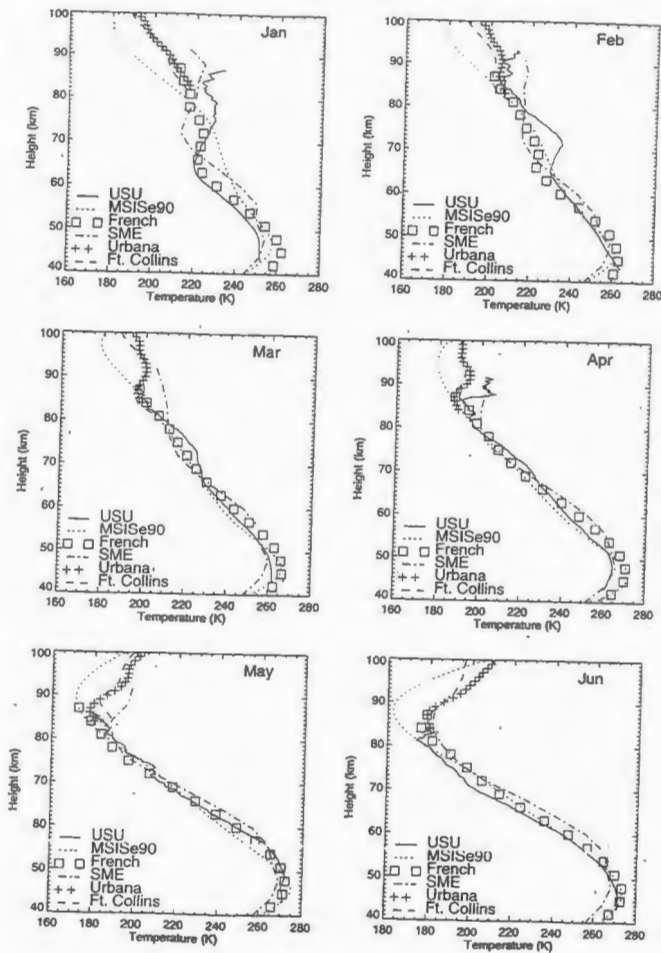


Figure 11. Comparisons of monthly-averaged mesospheric temperatures. The USU results are given by a solid curve. The other results are identified in the figure and discussed in the text.

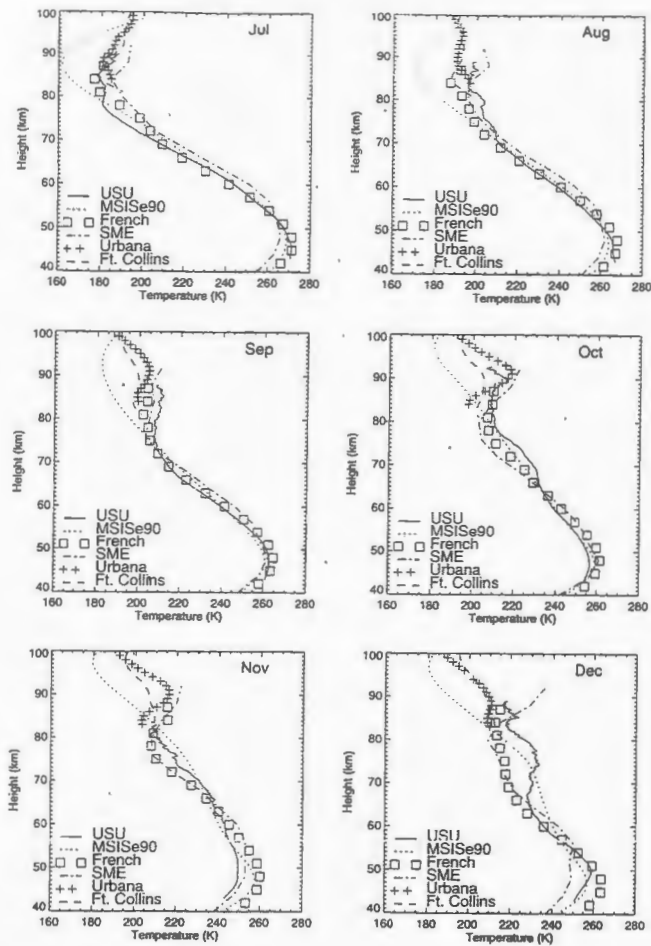


Figure 11. (Continued)

compare our lidar temperatures to it and we will use it to provide reference curves in many of the figures. To a great extent it is based on zonally averaged satellite-borne observations (limb and nadir viewing IR) compiled by *Barnett and Corney* [1985a] that became the basis of the low-altitude portion of the CIRA-1986 model *Fleming et al.*, 1990] and of the MSIS-86 thermospheric model [*Hedin et al.*, 1988] that became the high-altitude portion of the CIRA-1986 model. However, additional data were included from balloon-borne observations (radiosondes), rocket-borne instruments (grenades, falling spheres, pressure sensors, and mass spectrometers), high-altitude sodium lidar, accelerometers on the shuttle, and low-altitude (90–130 km) data from incoherent-scatter radars, and the middle atmosphere analysis was constrained to obey hydrostatic equilibrium. The full data set includes data acquired between 1947 and 1986, but the core satellite data set comes from 1973–1981 [*Barnett and Corney*, 1985b]. Another source of mid-latitude temperatures is the pair of French Rayleigh-scatter lidars at Haute Provence (44°N, 6°E) and Biscarrosse (44°N, 1°W) [*Hauchecorne et al.*, 1991]. The data to which we are comparing were acquired between January 1984 and December 1989 and cover the altitude range from 33 to 87 km. Another source is the SME satellite [*Clancy and Rusch*, 1989; *Clancy et al.*, 1994]. Limb-scan data in the near UV and visible spectra are used to construct Rayleigh-scatter profiles of density that are inverted, like the lidar data, to obtain temperatures between 40 and 92 km. The data were acquired between 1982 and 1986 in selected longitude intervals and over a range of latitudes. They were analyzed in 5° latitude intervals, and we are comparing to results from the interval centered on 40°. Between approximately 82 and 103 km, mid-latitude temperature profiles are available from sodium lidars operating at Fort Collins, CO, (40.6°N, 105°W) [*Yu and She*, 1995] and Urbana, IL, (40°N, 88°W) [*Senft et al.*, 1994]. They cover the periods from January 1991 to February 1994 and from January 1991 to August 1993, respectively. It should be noted that these other data sets were not included in the MSIS model.

In Figure 11, we show 12 monthly-averaged temperature profiles of our results and the comparison results just described. The curves are identified as follows: Rayleigh lidar at USU (solid lines), MSIS90 model (dots), French lidars (squares), SME satellite (dot dash), sodium lidar at Fort Collins (dashes), and sodium lidar at Urbana (plus signs). The USU, MSIS90, French, and SME profiles

for the months May through August all have smooth, monotonically decreasing temperatures between 50 and 80 km and appear very similar to one another. The differences among these curves increase at lower altitudes in passing from the mesosphere into the stratosphere. In going to higher altitudes, towards the mesopause, temperatures from the Ft. Collins and Urbana sodium lidars also become available. The profiles become more structured and differences among the curves increase significantly. For the other months, but especially for December through February, the profiles are much more structured and time variable giving rise to significant differences in appearance. These curves provide the starting point for much of the analysis that follows.

### 3. Summer Comparisons Between 50 and 70 km— Validation or Long-Term Trends

The intent here is to carefully compare temperatures from the several sources. Hence, we select a time period and an altitude region where they are determined with high precision and accuracy, and where there is minimal geophysical variability. Accordingly, we selected the period from May through August and the altitude region from 50 to 70 km. Our nightly precision is high, the French precision is slightly higher [Hauchecorne *et al.*, 1991], and the SME monthly precision is 2 K at both 60 and 70 km [Clancy and Rusch, 1989]. Because 70 km is considerably below the maximum altitude, the accuracy of the lidar temperature is excellent. It is harder to discuss the precision and accuracy of the MSISE90 model, except to say that it fits the 0–80 km, zonally-averaged, monthly temperatures compiled by Barnett and Corney [1985a] with a standard deviation of 3 K [Hedin, 1991]. The geophysical variability is low in these months as seen in our results (Table 4), the French results [Table 4, Hauchecorne *et al.*, 1991], and in Figure 11, which shows no evidence of the highly variable inversion layers [Schmidlin, 1976; Hauchecorne *et al.*, 1987; Hauchecorne and Maillard, 1990; Meriwether *et al.*, 1994; Clancy *et al.*, 1994; Whiteway *et al.*, 1995] in this altitude range for these months. This almost complete absence of inversion layers below 70 km is supported by the figures on daily occurrence height in Hauchecorne *et al.* [1987] and Whiteway [1994].

Table 4. Geophysical Variability of the Temperatures (K)

Height	Jan	Feb	Mar	Apr	May	Jun	Jul	Aug	Sep	Oct	Nov	Dec
43	12.7	8.3	8.6	3.1	1.4	1.8	3.7	4.0	3.8	3.9	6.1	10.5
46	8.2	4.2	5.7	2.0	1.1	1.7	2.2	3.4	2.6	3.4	5.2	8.8
49	4.6	4.5	5.8	1.6	2.8	1.8	2.1	2.4	2.1	2.6	5.0	9.3
52	4.1	5.6	4.9	3.4	2.0	1.5	2.5	2.3	1.7	2.6	5.8	7.7
55	5.8	4.1	4.7	2.1	6.2	1.8	3.2	2.5	1.9	2.5	8.8	5.2
58	6.7	4.5	5.1	3.1	5.9	3.2	4.2	2.4	2.6	4.2	7.7	4.6
61	8.4	3.8	5.6	3.5	2.9	3.8	3.2	3.1	3.6	5.2	10.4	5.1
64	11.9	6.4	6.7	4.5	2.3	4.0	1.5	4.4	3.5	7.1	12.0	7.1
67	16.1	6.5	5.8	7.2	6.7	5.2	3.6	4.8	5.0	6.4	9.6	10.6
70	15.7	8.9	7.4	9.6	4.8	4.7	4.8	7.2	5.9	6.1	9.0	12.8
73	15.1	11.6	9.4	12.6	6.5	5.6	7.1	6.4	8.9	5.4	10.9	11.2
76	16.6	14.7	8.6	11.1	10.8	7.0	11.2	7.1	7.0	6.5	11.0	14.0
79	15.5	15.7	11.3	15.7	3.5	10.2	7.6	4.9	5.0	9.0	10.2	16.3
82	14.1	9.6	15.1	10.8	11.7	10.6	8.2	8.6	11.1	13.4	6.1	24.6
85	16.6	7.5	12.3	13.6	3.8		6.8	10.4	13.0	14.6		26.8
88		13.3		21.4			6.1	14.4		14.8		20.4
91		13.2		24.8						11.1		

In Figure 11, we see what appears to be good agreement among our results, those from the MSIS90 model, and those from the French lidars. Except for an offset, good agreement also exists with the results from SME. These comparisons are shown more formally in Figure 12. Part (a) compares our results with the MSIS90 model temperatures, part (b) our results with the French lidar results, and part (c) our results with the SME results. The French and SME temperatures are available every 3 and 4 km, respectively, while ours are available every 112.5 m. To make these plots, we selected from our temperatures the ones that were within 56.25 m of the altitudes of the others. For the MSIS comparison, we selected every 20th of our temperatures, i.e., every 2.25 km, and computed the corresponding model temperatures. (Having smoothed our data over 3.0 km, these points are almost, but not totally, independent of each other.) To distinguish among the months, different symbols are used. If the temperatures were identical, the points would all fall along a 45° line through the origin. To a first approximation, the points fall along that line or one with a small offset with very little scatter. The uniformity in appearance of each comparison reflects small error bars (high precision). In fact, the error

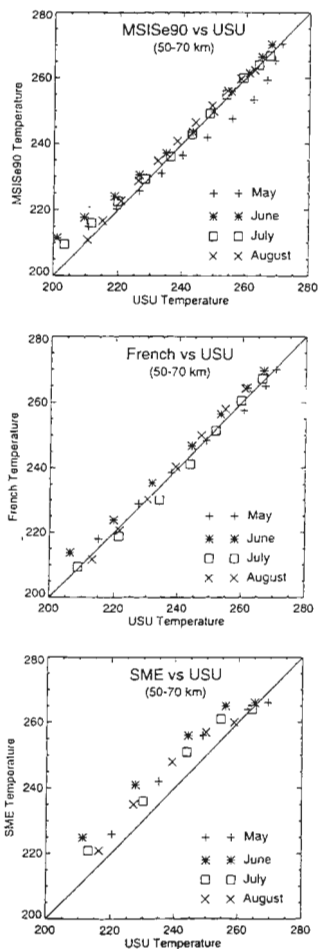


Figure 12. Temperature comparisons between 50 and 70 km for the period May–August. Refer to the labels in each part of the figure and to the discussion the text.



bars for the four sets of observations are equivalent to or smaller than the size of the plotting symbols.

Therefore, they have not been included.

In a straightforward comparison of these curves, very good agreement is found among the USU, French, and MSISe90 temperatures. The latter two temperature sets are approximately 2 K warmer than ours. While this exceeds the precision of our observations or the French, it is as good as has been reported among Rayleigh-scatter lidars. A comparison between the two French lidars for 65 nights yielded differences less than 2 K between 30 and 80 km [*Hauchecorne et al.*, 1991] and similarly 169 nights of simultaneous observations yielded differences between 1 and 2 K between 50 and 70 km [*Keckhut et al.*, 1993]. Another comparison with "simultaneous" data between 31 and 53 km for 18 nights yielded a standard deviation just below 2 K and with "nonsimultaneous" data for 12 nights just above 3 K [*Keckhut et al.*, 1996]. A comparison between the average temperatures from the Goddard Space Flight Center mobile lidar and the French lidar at OHP for 18 periods of simultaneous, co-located data shows an offset of 2 K for most of the region between 50 and 70 km [*Singh et al.*, 1996]. Thus the agreement among these three curves appears to be excellent. The agreement of the two lidars with MSISe90 is particularly important because the MSISe90 profiles are based on totally different measurement techniques.

The other comparison in Figure 11 is with temperatures from the SME spacecraft. Instead of the good agreement found with the others, the SME temperatures are systematically almost 8 K greater than ours and 6 K greater than the French and the MSISe90 temperatures. However, near the highest temperatures, near 50 km, the differences approach zero as the SME profiles approach a higher altitude stratopause. Another consequence of this higher altitude stratopause is that the SME stratospheric temperatures above 43 km are considerably colder than those in the other curves.

Because of the good agreement among our observations, the French observations, and MSISe90, we are looking for an explanation as to why the SME results are different. An obvious difference in the observations is that the SME data are from approximately 1400 local time (LT), whereas all the others are more representative of the middle of the night, essentially a 12-hour time difference. That raises the question of diurnal tides. At lower altitudes, a combination of diurnal and semidiurnal tides has been able

to reduce differences among observations [Wild *et al.*, 1995; Keckhut *et al.*, 1996]. Despite the MSISE90 model being largely dependent on zonally averaged data, it does include some time dependence. Near 70 km, it shows a 1-K increase in going from 1400 LT to 0200 LT; near 50 km it shows a negligible change. This is too small a correction and it is in the wrong direction. Tidal amplitudes and phases have been deduced from winter observations with the ISAMS instrument on UARS [Dudhia *et al.*, 1993]. In going from 1400 LT to 0200 LT, it predicts approximately a 2-K reduction in temperature. This is in the correct direction, but very small, and it is for winter instead of summer. A theoretical summer correction can be calculated using the Global-Scale Wave Model (GSWM) [Hagan *et al.*, 1995]. It shows a correction of 2.5 K in the proper direction near 50 km, turning into a 1.3 K correction in the wrong direction by 70 km. A GSWM winter calculation does not help to relate the winter ISAMS result to a summer one, because the altitude variations are different. However, the GSWM and ISAMS magnitudes are roughly the same. Even if the deduced corrections all had the correct sign, the magnitude of the correction would only be 2 K. Thus, at this stage of our understanding of tides, they do not appear to be able to account for this 6–8 K temperature offset.

Similar types of differences—offset between SME and both the French lidars and the CIRA 1986 model, and the stratopause altitude—were reported and discussed by Clancy *et al.* [1994]. Using older tidal information, they thought it might explain much of the offset. They then attributed the difference in stratopause altitude to the much coarser altitude resolution of the IR measurements used in CIRA 1986. In the present analysis, it does not appear that tides can explain the offset. As for the stratopause altitude, the two sets of lidar data have better altitude resolution than the SME data, and they agree with the MSISE90 model. Instead of saying that all four sets of data are consistent with one another, it appears that the SME temperatures are different. The French also found unexplained differences [Keckhut *et al.*, 1993], even when working with the colder values presented in Clancy and Rusch [1989] than those in Clancy *et al.* [1994]. While the SME data are from Rayleigh scatter, they are acquired by limb scanning. A consequence of that is a far more complicated data reduction procedure. We have no way of examining

this procedure, but we note that an altitude reduction of just over 2 km would bring the SME data into much closer agreement with the other data in both the mesosphere and stratosphere.

Thus, for this highly selected situation—May through August and 50 to 70 km—we have found very good agreement among our temperatures, the French temperatures, and the MSISE90 temperatures. We have also found a significant difference with the SME temperatures. At this point we would usually conclude that enough differences in technique, date, and location exist that this very good agreement among three of the data sets validates the results. And it may, but there is another consideration—the 11-year solar activity cycle and long-term trends.

Much progress has been reported in these areas, particularly by using the long and uninterrupted French lidar data set. Solar cycle variations have been treated by [Hauchecorne *et al.*, 1991]. Long-term trends have been treated by Chanin *et al.* [1987], Aikin *et al.* [1991], Hauchecorne *et al.* [1991], and Keckhut *et al.* [1996]. Because the four data sets treated in Figure 12 and discussed above come from different time periods, we need to examine the possible role of these two variations. We have done this by calculating the temperature corrections that would have to be made to the other three data sets to bring them to the time frame of our observations. We compared the average levels of the adjusted 10.7-cm solar radio emission and the time intervals between the center times of each data set. These activity levels, time differences, and temperature corrections are listed in Table 5.

**Table 5.** Temperature Adjustments for Solar Activity and Long-Term Trends

Site	Period	$\langle F_{10.7} \rangle$	$\Delta T_{\text{SolarCycle2}}$	Center Time	Elapsed Years	$\Delta T_{\text{LongTerm3}}$	$\Delta T_{\text{Total}}$
USU	1993–1995	79		1994.5 <sup>4</sup>			
French	1984–1989	116	-1.0	1986.5	8.0	-3.2	-4.2
MSISE90	1973–1981 <sup>5</sup>	125	-1.2	1977	17.5	-7.0	-8.2
SME	1982–1986	111	-0.9	1984	10.5	-4.2	-5.1

<sup>1</sup> Adjusted solar flux averaged over May–August for the years observed.

<sup>2</sup>  $\Delta T_{\text{SolarCycle2}} = 0.027$  K per unit change  $F_{10.7}$  in summer between ~55–70 km [Hauchecorne *et al.*, 1991].

<sup>3</sup>  $\Delta T_{\text{LongTerm3}} = -0.4$  K per year in summer btwn ~55–70 km [Hauchecorne *et al.*, 1991; Keckhut *et al.*, 1995].

<sup>4</sup> The center time is shifted later because the summer months come from only 1994 and 1995.

<sup>5</sup> This is the period for the core satellite data [Barnett and Corney, 1985b].

The solar-activity corrections for the French lidar and MSIS90 temperatures bring those two data sets and ours closer together. Thus the good agreement found above is unchanged. Even doubling those corrections, if they were the only corrections, would leave the good agreement among these three data sets intact.

The long-term trends, however, have a much larger impact. Combining them with the solar-activity corrections gives rise to large adjustments. The difference between the French profile and ours, over much of the altitude range, shifts from being 2 K warmer to being 2 K cooler. The significance of the difference does not change. The difference between the MSIS90 profile and ours, over much of the altitude range, shifts from being 2 K warmer to being 6 K cooler, which is significant. Thus the application of this long-term correction takes three curves that are initially very close together and separates them such that the two that are separated the most in time no longer agree. If the long-term trend were only half as large, i.e.,  $-0.2$  K per year, then the differences among these curves would be no bigger after the correction than before. Thus there is the suggestion, here, that the long-term trend derived from the French data is too big. This conclusion is not inconsistent with the French results. They have emphasized that the period they used to derive the trend is short, although it is the best available. In the above comparisons, we find the discrepancy when we introduce another type of data that is older. In addition, the uncertainty on their long-term trend is large. If we interpret their 95% confidence level as two standard deviations, then a trend of  $-0.2$  K per year is only just beyond the one standard deviation level.

By considering the SME temperatures again, the application of the corrections in Table 5 does not reconcile them to the other temperatures. The correction for solar activity is small enough that it has no impact on the comparisons. The correction for the combination of solar activity and long-term trends is slightly more complicated. While the separation between the SME profile and ours is reduced to the point that the difference is no longer significant within the precision of the two curves, the separation between the SME and the French profiles is just 1 K smaller, but between the SME and the MSIS90

profiles it is 3 K bigger. These differences are still very significant. Consequently, the problem of the warmer SME temperatures still exists.

Thus the comparisons in this carefully chosen season and altitude region provide useful results and a dilemma. First, we find a significant disagreement with the SME temperatures that we cannot reconcile or explain. Second, if we ignore solar-activity changes and long-term trends, we find good agreement among our temperatures, the French temperatures, and the MSISE90 temperature. Including the solar-activity changes deduced by the French has little impact because of the periods involved. However, including the long-term trend deduced by the French leads to a significant disagreement between our temperatures and the MSISE90 temperatures, but not between our temperatures and the French or between the French temperatures and MSISE90. This dilemma would be solved if the long-term trend, over the longer interval being considered, were half the size or smaller than what has been deduced. It would also be solved if the original temperatures that went into the MSISE90 model had been too small at the time they were determined.

### 3. Summer Temperature Fluctuations in the Lower Mesosphere

A question that arises in examining the low-altitude summer temperatures, as we examined in the previous subsection, is the apparent contradiction between a calculated precision far smaller than 1 K, which is consistent with the smooth averaged temperature profiles in Figure 11, and a geophysical variability in Table 4 that is the order of 2–5 K. The explanation is found by examining daily temperature profiles near the stratopause and lower mesosphere. Figure 13 shows seven all-night averages from July 1995 and the corresponding MSISE90 profiles. The left-most pair are plotted according to the temperature scale. To separate the profiles for the other days, 15 K has been added successively to the temperature values for each day. The errors bars are small enough that they only become visible near the top of the profiles, at 65 km. It is immediately apparent that significant temperature structures exist on all these days. However, the temperature structures are not as big as in winter, nor are they as coherent. The

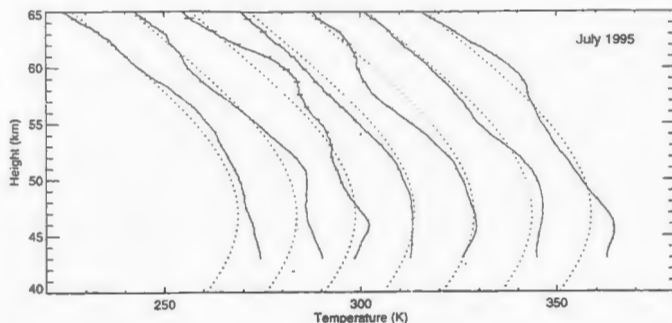


Figure 13. Daily temperature variations in summer near the tropopause and lower mesosphere. All-night temperature profiles for seven days from July 1995 between 40 and 65 km, with the data starting at 43 km. An increment of 15 K has been added to each successive curve starting with the second curve from the left.

structures vary from day to day such that they do not show up in the monthly averages. A major geophysical difference between summer and winter that may affect these structures is the reversal of the mesospheric jet, which will filter disturbances differently that are propagating upward from the troposphere or lower stratosphere.

#### 5. Relative Minimum Near 75 km in Summer— A Possible Zonal Difference

A closer look at the summer comparisons in Figures 11 shows a difference that stands out in the region between 68 and 78 km in June and July. The USU temperatures are consistently lower than the French and MSIS90 temperatures. This is seen clearly in Figure 14, which shows our averaged temperatures for June and July along with those from the French lidars and the MSIS90 model. Also shown for our temperatures are the uncertainties of the mean. The temperature differences are up to 7 K for much of this range and involve four to five independent points. While these data are from higher altitudes,  $h'_{\text{max}}$  is well above the altitudes of interest—82 km in June, 88 km in July—with the result that

the effect of the initial value should be much smaller than the observed differences below 78 km. Figure 15 gives a clear indication of what is happening. It shows the individual nightly averages for the six nights in June and the seven nights in July. In each case, a couple of the curves show the uncertainties. Because of possible confusion from overlapping error bars, they have been left off the other nights. However, they are essentially the same for all the June nights and for all the July nights. (They are much smaller for July than for June because all the June nights are from 1994 and the July nights from 1995. In the intervening year, we improved the receiving portion of the lidar system considerably.) Below approximately 77 km, an important point is that our nightly temperature curves are distributed between the French and MSIS90 temperatures and temperatures that are as much as 20 K colder. The biggest differences are seen in July near 76 km. A corollary to this point is that in going from 65 to 80 km, there is a big increase in the geophysical variability. This is seen directly in the curves in Figure 15 and in Table 4. By referring to *Hauchecorne et al.* [1987], *Whiteway* [1994], and *Whiteway et al.* [1995], what appears to be happening is that inversion layers are occurring with temperature maxima above 70 km. These maxima are associated with temperature minima at lower altitudes, which give rise to the temperature spread and the colder average that we are seeing. These low temperatures below inversion layers are most clear on three of the days in July.

Thus the occurrence of inversion layers with their vertical wave-like structure appears to account for the low temperatures that we see near 76 km compared to the French and MSIS90 temperatures. But why does the occurrence of inversion layers over USU lead to lower temperatures on average near 76 km than in the French or MSIS90 profiles? A possible explanation lies in the statistics of small numbers, i.e., that with 13 days total from these 2 months from 2 years we have not fully sampled the geophysical variability. By contrast, the French have 139 nights from a combination of two sites in 6 years [*Hauchecorne et al.*, 1991]. However, these observations are from the summer when interannual variability is small compared to winter observations. Hence, fewer observations should be needed to obtain a good average. This possibility will be answered in time when we have more observations and have been able to analyze them.

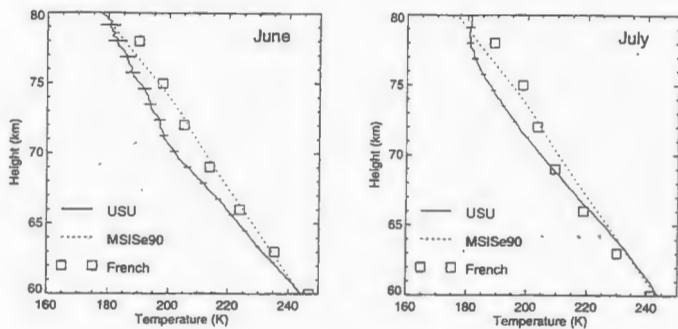


Figure 14. The relative temperature minimum between 65 and 78 km in June and July. Two figures showing USU, French, and MSISe90 temperature curves from 60 to 80 km.

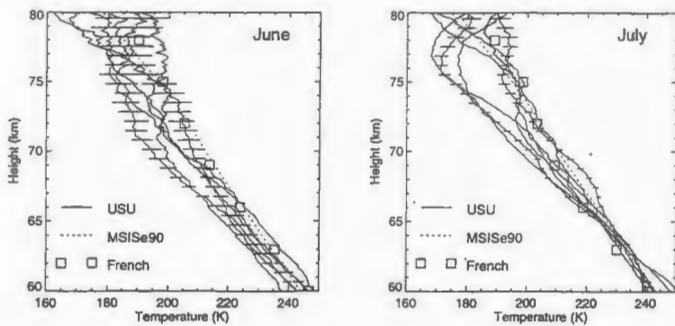


Figure 15. Daily temperature curves for June and July between 60 and 80 km. Two figures showing USU, French, and MSISe90 temperature curves from 60 to 80 km.



An alternative explanation, a more speculative one, is that zonal differences do exist because of our location, longitudinally situated in the middle of the Rocky Mountain Range. The idea is that because of the fairly extreme mountainous topography, more gravity waves and, possibly, stationary planetary waves are generated than elsewhere. As a consequence the inversion layers and the associated lower-altitude temperature minima are more pronounced than elsewhere. Consistent with this temperature minimum being part of an inversion layer, the average summer temperatures just above 80 km at USU are slightly higher than the French temperatures. (We are paying more attention to the relative minima than to the relative maxima because they are in a better altitude region for making detailed comparisons.) The role of orography in the generation of gravity waves [Nastrom and Fritts, 1992; Bacmeister, 1993] and standing planetary waves [McLandress and McFarlane, 1993] has been studied and discussed, as has the relationship between gravity waves and the inversion layer [Hauchecorne et al., 1987; Hauchecorne and Maillard, 1990; Whiteway et al., 1995]. The effect of orography on tropospheric winds was shown clearly in Nastrom and Fritts [1992]. However, it has been difficult to examine the effects of orography at higher altitudes and in widely separated geographic regions. Using the SME data, Clancy and Rusch [1989] looked for differences in the temperatures at 65 km between 95°W to 125°W and 10°W to 20°E. They found differences, but also enough other variations that they could draw no conclusions. If we have found a longitudinal difference, it would imply that some aspect of the Rocky Mountains produces a bigger effect than the Alps. It would also imply that differences should be seen between USU temperatures and those that would be observed in the eastern U.S. or Canada. It would further imply that we should have a colder relative minima and a warmer inversion layer in winter than those in the French and MSISe90 profiles. This effect would shift downward with the inversion layer in winter.

## 6. Low MSISe90 Temperatures Between 80–90 km

Moving upwards, the next region to examine is between 80 and 100 km. Our averaged Rayleigh data and the French data extend to at most 90 km, thereby overlapping with the sodium data from Urbana and Ft. Collins that span the region from 83 to just above 100 km. The curves in Figure 11 clearly show a discrepancy between the MSISe90 model temperatures and the observations for every month, with the

observations being as much as 10 to 30 K warmer than the model. Several different effects arise out of this discrepancy. In May, June, and July, the observed mesopause is both warmer and at a lower altitude than in the model. In October, November, and, possibly, September, an inversion layer appears with a peak centered at 90 km and a minimum between 80 and 85 km. Hints of this relative peak also occur for most months between December and April. In the period between September and February, or, possibly, between August and March, the mesopause occurs at a higher altitude than predicted by MSIS90. This set of comparisons thus shows the boundary between the mesosphere and the thermosphere to be very different and far more complicated than in the MSIS90 model.

While much of the above discussion is based on the sodium observations, our Rayleigh temperatures support and confirm them up to almost 90 km and integrate them with what is happening in the mesosphere below 83 km. For 8 months—January through March, July through October, and December—our average temperature profiles reached approximately 90 km. As previously explained, that means half the daily profiles started at a higher altitude, some as high as 100 km. Because our initial values are based on the Ft. Collins sodium temperatures, as also explained earlier, it might be thought that our results are not independent of theirs. However, to a great extent they are. First, as already indicated, half of our daily curves go higher than the maximum altitude  $h'_{\max}$  indicated. Consequently, they have up to 10 km for the role of the initial value  $T(h_{\max})$  to diminish, with the result that the averaged highest-altitude temperature shown  $\langle T(h'_{\max}) \rangle$  will at least reflect whether the actual temperature is higher or lower than the curve from which the initial values were selected. For most of the 8 months for which our profiles end near 90 km,  $\langle T(h'_{\max}) \rangle$  is bigger than the Ft. Collins temperature. If the real initial temperatures were closer to the colder MSIS90 model temperatures, then  $\langle T(h'_{\max}) \rangle$  would have been smaller than the Ft. Collins temperatures. To further examine this argument, we reexamined the September data to formally determine the effect of the initial temperature. We selected the 19 days from 1995, all of which have good observations that extend to at least 90 km. In one analysis we used initial values based on the Ft. Collins data, as usual, and in the second analysis we used initial values based on

the MSIS90 model. The results are shown in Figure 16 along with the MSIS90 curve. The curve initiated with Ft. Collins temperatures is almost identical to the one in Figure 11. The temperatures are much greater than the MSIS90 temperatures and, in fact, greater than the Ft. Collins temperatures. The curve initiated with the MSIS90 temperatures shows colder temperatures than the other at the highest altitudes, but the temperatures are still significantly above the MSIS90 temperatures. These two curves merge at 77 km, at which point they are still warmer than the MSIS90 profile. Thus, our Rayleigh temperatures confirm the much warmer temperatures found by the sodium lidars above 80 km than given by the MSIS90 model.

By extending the high-altitude Rayleigh temperatures to their current limit, our October results support the temperature maximum seen by the sodium lidar. At 93 km in Figure 11 (i.e., at  $h'_{\max}$ ), the Rayleigh temperature is already well above the Ft. Collins temperature. By 90 km it reaches its maximum, overlapping the Urbana temperatures, and then decreases to a minimum near 85 km.

Having seen such good agreement between the MSIS90 model and Rayleigh-scatter lidars in the altitude range 50–70 km, we ask the obvious question: What happened between approximately 80 and 100 km? How did the model miss these major temperature differences and the complexity of this region? In constructing the model, one of the problems was a lack of good observations between 80 and 100 or so km [Hedin, 1991]. The satellite techniques produced good observations below 80 km [Barnett and Corney, 1985b]. Although used for this interval [Hedin, 1991], the rocket results are fairly limited in this region [see discussion in Lübken *et al.*, 1994, and references therein]. The incoherent-scatter radars cannot contribute much below 100 km. Very limited lidar data were used, and only then from high latitudes [Hedin, 1991]. Thus the profiles between 80 and 100 km are largely the result of fitting smooth curves of density and temperature, which were constrained to obey hydrostatic equilibrium, to the data from lower and higher altitudes. This apparently accounts for much of the discrepancy between the model and observations in this altitude region. The study of this transition region, or mesopause region, will depend greatly on observations by both Rayleigh and resonance lidars.

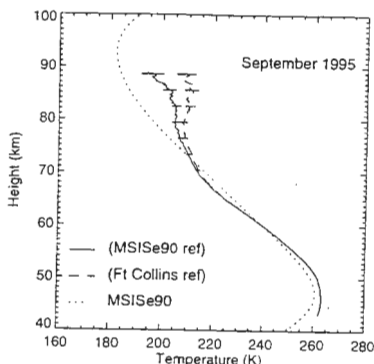


**Figure 16.** The September temperature profile initiated with Ft. Collins temperatures and with MSISe90 temperatures. The results show that the MSISe90 model temperatures are too cold near 85 km at mid-latitudes.

#### 7. Annual Temperature Cycles in the Stratopause and Upper Mesosphere

The change from summer to winter temperatures is shown in Figure 17. The four summer months (May–August) are shown with solid lines, and the four winter months (November–February) are shown as dashed lines, and the remaining four equinox months are shown as dotted lines. The temperature curves are the monthly averages from Figure 11. But, presented in this way, they provide considerable information about the seasonal transition throughout the mesosphere. In the lower mesosphere and stratopause we see an annual cycle ranging over 18 K with a hot summer and cold winter. In the upper mesosphere the opposite or inverse occurs: We see an annual cycle ranging over 45 K with a cold summer and hot winter. The reversal in behavior between the lower and upper mesosphere appears to occur at 62 km.

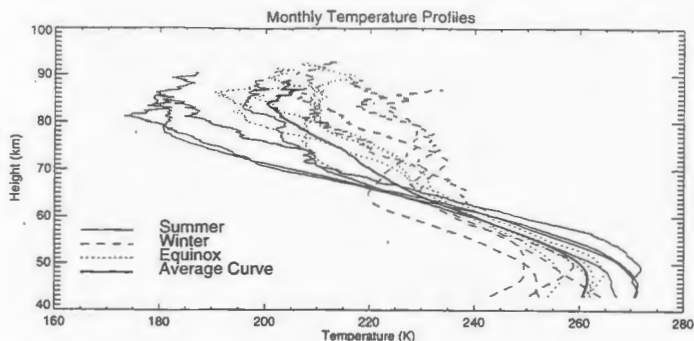


**Figure 17.** The annual variation in monthly averaged temperatures and the annual averaged temperature for USU. This shows an 18 K variation near the stratopause and a 45 K variation in the upper mesosphere, with a minimum variation near 62 km. At lower altitudes, the temperatures are hotter in summer than in winter. At higher altitudes, they are hotter in winter.

This difference in seasonal temperature behavior is a basic characteristic of the mesosphere. Just as we can examine it, so can other instruments. In Tables 6 and 7 we compare the annual cycles observed in the stratopause (and lower mesosphere) and in the upper mesosphere, respectively. For the lower altitude region, we have included data from USU, from the French lidars [Hauchecorne *et al.*, 1991], and from SME [Clancy *et al.*, 1994]. The latter data are included because, despite the temperature offset in the previous comparison, their behavior is similar enough to the lidars that relative measurements may be more accurate. For the upper altitude region, we have included these same three sources, plus the sodium lidars at Urbana [Senft *et al.*, 1994] and at Ft. Collins [Yu and She, 1995]. All the values in Tables 6 and 7 were determined in the same way. The analyses of the French and CSU groups showed that the annual variation dominates the semi-annual variation in the chosen altitude regions. Accordingly we chose

periods 6 months apart that gave the biggest seasonal change when using the tabulated data. Depending on the instruments, the best pair of months

would shift by one. By averaging two months in each season, we were able to treat each data source the same way. However, we did find a significant shift between the two altitude regions. The maximum seasonal variation occurred a month later in the upper mesosphere than in the lower mesosphere. The lower altitude was found to be fairly broad, 44–49

km, for the maximum variation. In the upper altitude region, the different altitude behaviors of the summer and winter temperature profiles give rise to a narrow region near 85 km for the maximum variation. For the Rayleigh lidars, we used the tabulated values centered at 84 or 85 km. For the sodium lidars, we averaged the values between 84 and 86 km.

In each region, the summer temperatures were fairly similar and the winter temperatures were more variable. Thus variations in the winter temperatures are what give rise to the different seasonal variations. In the stratopause region the USU variation is 50% greater than the French variation and the same as the SME variation. Hence there is a suggestion that the French data might reflect the effects of more or larger stratospheric warmings over Europe than over North America. In the upper mesosphere, the sodium lidars have one variation and the instruments depending on Rayleigh scatter have a larger variation, the largest coming from our temperatures. The magnitude of our variation is somewhat surprising, because the Ft. Collins temperatures from only a few km higher are used for the initial values. This appears to imply much higher winter temperatures over Utah, at least for the two winters

**Table 6.** Comparison of Stratopause Annual Temperature Variations—44 to 49 km

Source	Summer <sup>1</sup> [K]	Winter <sup>2</sup> [K]	Change [K]
SME	267	249	18
France	272	261	11
USU	271	253	18

<sup>1</sup>Summer = Average of May and June temperatures

<sup>2</sup>Winter = Average of Nov. and Dec. temperatures

**Table 7.** Comparison of Upper Mesospheric Annual Temperature Variations—84 to 85 km

Source	Summer <sup>1</sup> [K]	Winter <sup>2</sup> [K]	Change [K]
SME	183	218	-35
France	176	213	-37
USU	179	224	-45
Urbana	182	212	-30
Ft. Collins	181	212	-31

<sup>1</sup>Summer = Average of June and July temperatures

<sup>2</sup>Winter = Average of Dec. and Jan. Temperatures

contributing to these averages. Additional data and more analysis will resolve this question. But the sense of the difference between the Rayleigh and sodium instruments is still there. Both are operating near the limit of their altitude range. Hence it appears possible that the difference has an instrumental origin. This can only be solved by additional comparisons, preferably by co-located Rayleigh and sodium lidars and by a more sensitive Rayleigh lidar.

An extension of this discussion of the transition from summer to winter is that we can find a mean temperature profile for the year. It is given in Figure 17 by the heavy solid line. This profile can be compared to the annual mean profiles found by the French and CSU. We found a stratopause temperature of 260 K, whereas the French found 266 K. At the minimum near 85 km we found the temperature to be 205 K, whereas the French found 198 K. CSU found almost the same temperature as the French at 85 km, 196 K. These differences come about largely because of variations in the winter temperatures, as first discussed. Compared to the others, we found a colder stratopause and a warmer upper mesosphere, which is consistent with the inverse temperature relationship between the stratopause and upper mesosphere.

## 8. Variability of the Winter Temperature Profiles

The other aspect of the seasonal transition that stands out in Figure 17 is the change from smooth variations with altitude in summer to highly structured altitude profiles with what often appear to be large oscillations. For example, the lone curve that stands out because of its low temperatures between 50 and 65 km is for January. More generally, this large variability is also reflected in Figure 11 in large differences between our observations and the model profiles, among the different sets of observations, from one month to the next, and in Table 4 in the geophysical variability. Unlike the summer, the geophysical variability increases in going downward from 55 to 43 km. The French have attributed this to stratospheric warmings in January and February. However, the variability is there at low altitudes from November through March in our data and theirs. The variability also increases at all altitudes in going from summer toward winter, particularly November through February. Thus the greatest variability is in the warm, winter, upper mesosphere. The French have examined this extensively and attributed much of it to planetary waves [Hauchecorne and Chanin, 1983; Chanin *et al.*, 1987; Hauchecorne *et al.*, 1991].

The basic idea is that propagating planetary waves will have a phase velocity toward the west such that they will not have a critical layer interaction in winter with either the tropospheric or mesospheric jets that are both propagating from west to east. They can then propagate upward into and through the mesosphere. With periods of 2, 5, and 16 days, they are not averaged out like many gravity waves in our 11-night integrations. Hence they will give rise to considerable variability. In summer, in contrast, many of them have a critical layer interaction with the mesospheric jet, which is now directed from east to west, and they are filtered out.

In the mesosphere, the feature that stands out most strongly in the winter profiles in Figure 11 is a temperature increase centered between 65 and 80 km. Also apparent in the averages for January and December is a temperature decrease centered 10 to 15 km below the maximum in the increase. By examining shorter sequences of temperature profiles—1-hour and nightly intervals—it is evident that this winter variability results from the mesospheric inversion layer [Schmidlin, 1976; Hauchecorne *et al.*, 1987; Hauchecorne and Maillard, 1990; Meriwether *et al.*, 1994; Clancy *et al.*, 1994; Whiteway *et al.*, 1995]. For a given night, the inversion layer appears as a temperature increase with respect to the MSISE90 model of 10 to 50 K. Nonetheless, because it usually has a downward phase progression during the night and varies in altitude from night to night, its appearance in a monthly average is smaller than in a 1-hour or a one-night average. However, it has to have considerable coherence during the month and a certain amount of year-to-year repeatability to show up in these monthly averages. The same is true for relative temperature minimum below the inversion layer peak.

The larger apparent variability in the USU averages than in the other data sets, particularly the French and the MSISE90 model, also suggests great year-to-year, or interannual, variability. The USU data are averaged over 2 years whereas these other two data sets are averaged over 5 to 8 years. These two inversion-layer features, the relative maximum and minimum, together give the appearance of a vertical wave with respect to the model temperature profile. A more detailed discussion of our inversion layer observations is beyond the scope of this dissertation.



Another aspect of the winter variability is the stratopause temperature. Whereas in the summer period from May through June, the stratopause temperatures from USU, France, and the MSIS90 model differ by no more than 4 K, and usually by much less, the winter temperatures regularly differ by 10 to 15 K. The largest differences in the averages occur between November and January, but they also occur in October and between February and April. The lowest stratopause temperatures are seen at USU and the highest in France. The MSIS90 temperatures tend to fall anywhere in between these two extremes, but are usually closer to the French results. Thus the USU winter stratopause temperatures appear to be systematically lower than the French observations and the MSIS90 model.

This difference appears to be real. The earlier summer comparisons between 50 and 70 km showed excellent agreement, and summer stratopause comparisons show almost as good an agreement. With the 43 km lower altitude limit, there should be no problem from PMT saturation. Even if there were, it would give rise to temperatures that are too hot, not too cold. Furthermore, as we will see below for 1-4 January 1995, in some shorter averages our temperatures are greater than the MSIS90 temperatures. As mentioned above, that our yearly mean was colder than the French mean implies that our winter temperatures were colder. Combining all these factors, we conclude that the USU winter stratopause temperatures are truly lower than the other two sets.

We can gain insight into what is happening in this apparent interannual variability by looking at shorter averages. As shown in Figure 18, these winter temperature profiles differ tremendously from one year to the next. This figure compares monthly averaged temperatures for January 1994 and 1995, and for February 1994 and 1995. In both cases we see the averaged inversion-layer peak at a lower altitude in 1994 than in 1995. We see, using the MSIS90 profiles for reference, that the higher altitude peak shows a greater temperature enhancement. In January we also see that the temperature minimum is at a lower altitude and smaller in 1994 than in 1995. (For our chosen temperature reference, a temperature minimum is not obvious in either February.) Thus we see large interannual variability in the winter profiles, and we see more wave-like disturbances. In addition, in the two Januarys we see a difference in the stratopause temperatures. In 1994, the year with the smaller and lower altitude mesospheric

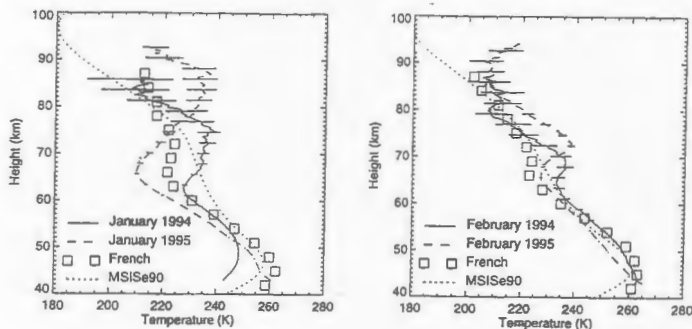


**Figure 18.** Average temperatures for January 1994 and 1995 and for February 1994 and 1995. The inversion later is at a higher altitude and the variation greater in 1995 than in 1994.

disturbances, the stratopause temperature is considerably below (almost 10 K) the MSISE90 temperature whereas in 1995 the stratopause temperature is much warmer, almost equal to that of the model. Thus, this is a situation where the inverse relationship does not hold between the stratopause temperature and the upper mesopause temperature.

To try to determine more about this large winter variability, we examined the January 1995 data more extensively. In that month, we had a series of observations near the beginning and a series near the end. The individual profiles in the two time periods are similar, but the profiles in the two periods differ significantly from one another. The average profiles for 1–4 and for 20–23 January are shown in Figure 19. (In contrast, in February 1995, we observed for eight nights in a nine-night period. All the profiles were very similar to one another throughout the period.) The mesospheric disturbance for 20–23 January is smaller than for 1–4 January and the stratopause temperature for 20–23 January is smaller than for 1–4 January. These mesospheric and stratopause differences within 1 month are very similar to the

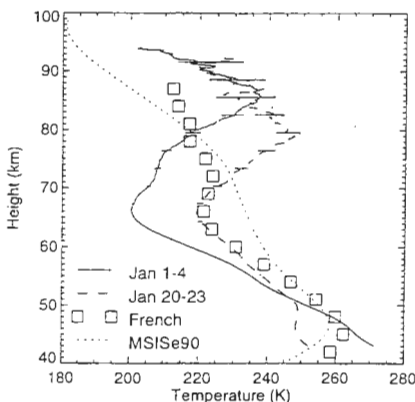


**Figure 19.** Short-term winter temperature variations—averages from 1–4 and 20–23 January 1995. The variability in 2–3 weeks is comparable to the observed interannual variability.

interannual differences. Thus, on the scale of 10–20 days, major changes can occur in the temperature profiles, and these changes may well account for much of the interannual changes. (We are currently investigating whether these changes are related to planetary wave activity or the passage of weather fronts.) In addition, changes in the stratopause appear to be linked in yet another way to changes in the mesosphere. When the stratopause temperature is higher, the negative and positive excursions in the mesosphere appear to be larger.

### 9. Possible Zonal Differences

Returning to the stratopause and upper mesosphere temperatures and extending the discussion to the full winter period, it appears that from October through April (with one exception) the USU stratopause temperatures are lower than the French and MSIS90 temperatures and that the USU temperatures between 70 and 80 km (with one exception) are greater than the French and MSIS90

temperatures. This behavior is similar to the inverse relationship described by the French between stratopause temperatures and upper mesospheric temperatures [*Hauchecorne and Chanin, 1983*]. In describing some of their mesopause temperatures, the French [*Hauchecorne and Chanin, 1983*] discuss a series of minor stratospheric warmings during the winter—particularly in January and February—that would have been included in their averages. Perhaps fewer of these minor warmings occurred during the winters of 1993/1994 and 1994/1995 than occurred on average during the period of the French observations and the difference between their data and ours reflects the sparse sampling in our data. That seems unlikely. Besides, the period with the low stratopause temperatures extends 2 months on both sides of the two primary winter months when most of the minor stratospheric warmings are supposed to occur, enough that the average can be significantly biased. Except for the possibility that a 2-year sample is too small, it appears that the stratopause temperatures are lower at USU than in the two comparison curves and that the upper mesosphere temperatures are warmer. If true, this would imply a zonal difference. In support of the possibility of a longitudinal difference in the middle atmosphere above USU is the observation of a different wind behavior from 87 km above BLO in winter than elsewhere [*Wickwar et al., 1997b*]. This OH wind result strengthens the argument that the difference is real and not a feature created by limited sampling as the OH wind results are based on four winters, each with many more samples. Furthermore, the temperature difference implies a larger winter-summer variation at the longitude of USU than elsewhere, which would, in turn, imply a larger dynamical contribution to the winter-summer variation in this longitude region at mid-latitudes.

#### 10. High-Latitude Comparison

In the literature there is another set of monthly temperature profiles with which to compare. The profiles come from northern Norway [*Lübken and von Zahn, 1991*], from Andenes at 69° N where the Andoya rocket range and the ALOMAR lidar facility are located. The temperatures come from several rocket techniques—passive falling spheres, ionization gauges, mass spectrometers—and from pre-ALOMAR sodium lidar observations [e.g., *Fricke and von Zahn, 1985*]. They were acquired between 1980 and 1990, and extend from 50 km up to almost 105 km. Because of the 27° latitude difference, we

expect to see differences. The two sets of monthly averaged profiles are shown in Figure 20: only nine are available from Andenes and the corresponding USU ones are the same as in Figure 11. For simplicity of presentation, no other curves are shown. However, reference will be made to the other mid-latitude curves shown in Figure 11.

Starting as close to equinox as possible, i.e., in March and October, we see that the profiles are very similar at the two locations. In fact, these are the two most similar pairs of profiles. However, there is a hint that the stratopause is 5–10 km higher at Andenes. This is the direction we would expect for radiative equilibrium and a bigger zenith angle at higher latitudes. (For a similar distribution of absorbing constituents, the same optical depth will occur at a higher altitude.) The upper mesosphere and mesopause region appears less structured at the higher latitudes, especially in October (compare to Figure 11). The mesopause appears to be just below 100 km at the higher latitudes, which is at a lower altitude than in the Ft. Collins and Urbana data, and the curves do not show either the relative minimum near 85 km or the relative maximum just above 90 km that appear in the lower latitude data. However, there is a hint of both of these in the October profile. But there is no such hint of these features in the November or December profiles. This suggests that the relative minimum and maximum form one feature and that it is a mid-latitude feature. That this feature may be present at high latitudes in October, but not in the two subsequent months, is consistent with it resulting from chemical heating, which depends on photolysis of both  $O_2$  and  $H_2O$ , as argued by *She et al.* [1995] and *Meriwether and Mlynczak* [1995].

In summer—June through August—major differences appear in the comparison. Despite being sunlit nearly 24 hours a day, the high-latitude mesopause is much colder than the mid-latitude mesopause. In this case, in June and July, the mesopause at Andenes is 45 K colder than the mid-latitude mesopause, 130 K versus 175 K. Its altitude at 88 km is approximately 3 km higher than shown for mid-latitudes in Figure 11. This is a classic illustration of the importance of the upper mesospheric region, the fact that its temperature structure is dominated by dynamics instead of radiation. In contrast to the mesopause, the lower mesosphere near the stratopause is almost 20 K warmer at high latitudes, as would be expected when radiation dominates the heating process. Structure exists near 60 km in the high-latitude profiles

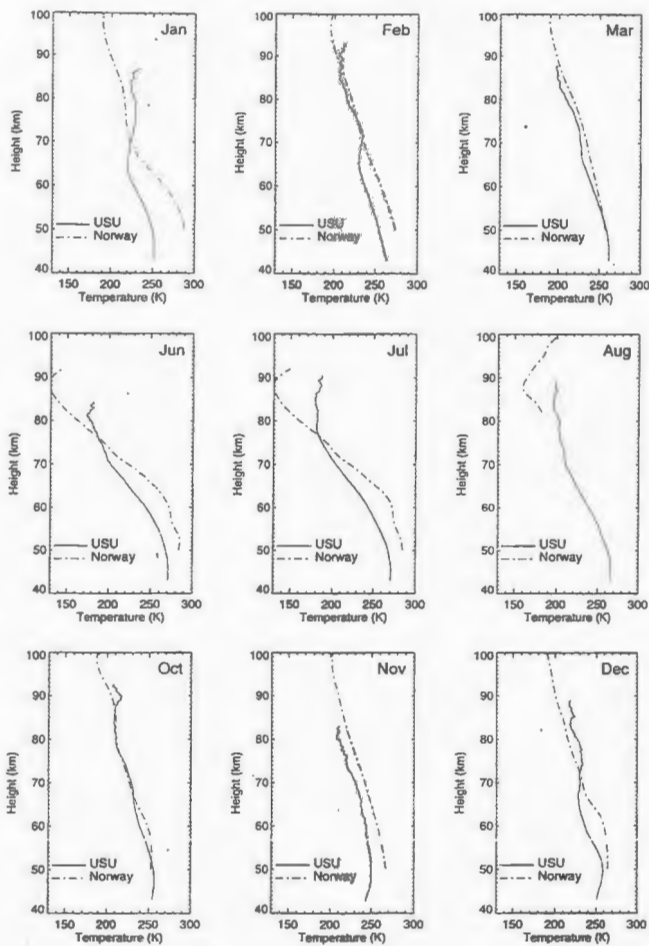


Figure 20. Comparison of mid- and high-latitude temperatures. The high-latitude temperatures are adapted from *Lubken and von Zahn [1991]*.

that reflects something more complicated in either the composition, and hence the radiative heating, or in the dynamics. Because of the warmer stratopause and colder mesopause, the high-latitude lapse rate in the mesosphere is greater. However, there is also a difference in the shapes of the lapse rates. The high-latitude curves show it to be smoothly varying and nearly constant between 60 and 85 km, whereas the mid-latitude curves show what appear to be two regimes. Between 50 km and someplace between 70 and 80 km, the lapse rate is smoothly varying and nearly constant, albeit with a smaller value. Above that altitude, it becomes much smaller and more structured. This suggests different physical processes occurring in this altitude region at mid-and high-latitudes.

In winter—December through February—as at mid-latitudes, the high-latitude average profiles are more variable than during equinox and summer. Again, the greatest departure from the other profiles, the greatest variability, occurs in January. Unlike the summer profiles where such a large systematic temperature difference exists between the high- and mid-latitude profiles above 75 km, the values in winter are reasonably similar. In December and January, the high-latitude temperatures are approximately 10 K cooler than the mid-latitude temperatures and in February they are approximately 5 K warmer. If we include November, its high-latitude temperatures are approximately 10 K warmer. The high-latitude data do not show any sign of the 92-km relative maximum that appears in the mid-latitude data. (While this maximum was particularly big in October and November, it is there but much smaller in December and February.) Given the variability in both latitude regimes, these profiles show good agreement above 75 km. However, descending towards the stratopause, the high-latitude temperatures are consistently 10 to 40 K warmer than at mid-latitudes. In December and February the temperature at 50 km are 10 K warmer than at mid-latitudes, but cooler than in summer. However, in January they are 40 K warmer than at mid-latitudes and the same temperature as in summer. Thus in winter the high-latitude stratopause temperatures are warmer than at mid-latitudes, despite being in darkness, and the January temperatures are the same as in summer. These are good indications that the high-latitude winter stratopause is not in radiative equilibrium, i.e., that there is another heat source, presumably from dynamics.

## 11. Summary and Conclusions

We have obtained high quality, middle atmosphere temperatures with Rayleigh-scatter lidar above Logan, UT, which is situated in the middle of the Rocky Mountain range. As a result of analyzing these temperatures and comparing them to other data sets, we have a number of conclusions relating to both the instrumentation and to middle atmosphere research.

While this technique provides absolute temperatures, the successful use of it depends critically on how it is implemented. Consequently we went to considerable lengths to describe our implementation and to devise a good comparison that would effectively validate the results. We chose to use the May–August temperatures between 50 and 70 km because this part of the year has minimal geophysical variability and because this altitude range is well separated from possible PMT saturation effects at lower altitudes, potential background problems at much higher altitudes, and inaccuracies in the initial temperature. We found good agreement among our temperatures, the French temperatures, and those in the MSIS90 empirical model. However, when we took into account the solar-activity cycle (0.027 K per unit of  $F_{10.7}$ ) and the long-term trend (-0.4 K per year) found by the French [*Hauchecorne et al.*, 1991; *Keckhut et al.*, 1995], using data from much of a solar cycle, a significant portion of this apparent agreement disappeared. This leads to difficulties with respect to resolving the problem of whether or not long-term changes—natural or anthropogenic—are occurring in the middle atmosphere. The differences could be reconciled if the original observations contributing to CIRA 1986—hence, to MSIS90—produced temperatures that were significantly too small (6K) and the French temperatures were too small (2 K), or the MSIS90 temperatures were too small (3 K) and our temperatures were too big (2 K); if the long-term trend used were at least a factor of two too large; or if the long-term trend changed from solar cycle 21 to 22 and were much smaller in solar cycle 21.

A conclusion from these comparisons is that there is a very good agreement at the 1–3 K level. To do much better, i.e., to improve the accuracy, it is essential to explore all possible sources of systematic error and to reduce them to the order of 0.1 K. Another conclusion is that at the present level of accuracy, it is very difficult to use the temperatures from several instruments to say much about the long-term trend



found by the French. There is a hint that it may be too big, but it is not more than a hint. To say more, long time-series of consistent observations are needed at several individual lidar sites. For determining trends in the upper mesosphere, it will also help if new observations can be made with the next generation of more powerful Rayleigh-scatter lidars, especially if the initial temperature value can be obtained from simultaneous, co-located resonance lidar observations.

Some differences appear in our temperatures compared to the French observations and the MSISE90 model that are hard to explain without invoking zonal differences in the temperature structure. Our monthly-averaged mesospheric temperatures from June and July from near 75 km are systematically lower than those from the other two sources. Nightly curves indicate that the monthly averages are lower because of the occurrence of a 10–20 K temperature minimum below a high-altitude summer-time inversion layer on approximately half the nights. On the other nights the temperatures are comparable to those from the other sources. The summer months are so free of major temperature disturbances compared to the winter months that we assume this difference is a general feature as opposed to an artifact arising from the use of data from only 2 years. Another difference between our temperatures and those from the other two sources occurs in winter. It appears in the monthly averages as lower temperatures near the stratopause and as higher temperatures in the upper mesosphere thus exhibiting the usual inverse temperature relationship between these two altitude regions. Because of the large winter variability it may reflect the fact that our averages are biased due to a limited sampling period covering only 2 years instead of six or more years. That these differences represent real differences and represent a zonal difference is supported by the results of 4 years of OH-wind observations from 87 km at BLO [Wickwar *et al.*, 1997]. Because of the location of the lidar and BLO longitudinally in the middle of the Rocky Mountains, it is reasonable to speculate that a zonal difference might arise from the orographic generation of gravity waves. The resolution of this possibility will require a longer time series of lidar and wind observations, additional mesospheric observations, and extensive comparisons with similar observations at other mid-latitude sites.

Wintertime conditions in the middle atmosphere are highly variable, the major feature being the temperature inversion layer and its associated minimum approximately 15 km lower in altitude. This variability peaks in December, January, and February. In our 2-year average, we obtained a much more structured profile than apparent in the French results of the MSISE90 model, each of which include data averaged over many more years. We also had considerable variation from one winter to the next. Accordingly we wondered about interannual variations and, perhaps, the QBO [e.g., Chanin *et al.*, 1989b]. However, a closer examination of the variability within one year goes a long way towards explaining the observations. From sets of observations on successive nights (or almost successive nights), we found that these temperature structures appear to have lifetimes of the order of 1 to 2 weeks. After that period the structures may change significantly. Thus we found two periods 3 weeks apart in January 1995 with temperature profiles almost as different as those we had from one year to the next. (We are examining these variations in an attempt to establish their cause.) While there appears to be a large interannual variation, it may arise from variations within a month and the frequency of our observations. To properly determine the nature of the winter variability, it is essential to observe as often as possible.

In the summer, despite extremely smooth monthly averages, the geophysical variability in the lower mesosphere far exceeds the precision of the observations. Nightly averages show that this comes from temperature fluctuations with a magnitude of approximately 5 K. Consistent with the smooth monthly averages, but unlike the winter inversion layers, these fluctuations on successive nights appear to be randomly located in height and to have randomly varying altitude separations. Thus there are extensive, small amplitude, summer fluctuations that appear in the lower mesosphere, which are very distinct from the fluctuations produced by the winter inversion layers.

A comparison between our mid-latitude temperature profiles and high-latitude temperature profiles provides more information on the effects of the meridional circulation. The profiles are remarkably similar at the two equinoxes, but their behavior is not symmetric about the equinoxes. In the upper mesosphere, the high-latitude temperatures in mid-winter are only slightly warmer than ours. But in mid-summer, they are much colder. Thus the larger annual temperature variation at high latitudes.

compared to mid-latitudes, arises mainly because of much lower temperatures in summer. These lower summer temperatures arise in part because of a nearly constant lapse rate between 60 and 85 km. In contrast, at mid-latitudes the lapse rate decreases in magnitude sharply at 70–75 km. It is as though the vertical motion and associated expansion cooling goes to a higher altitude at high latitudes. Near the stratopause, the high-latitude temperatures in summer are warmer than ours, as would be expected for radiative control and many more hours of sunlight than at mid-latitudes. The high-latitude stratopause is also at a higher altitude than ours, as would be expected for radiative control and a much bigger solar-zenith angle than at mid-latitudes. However, in winter, the high-latitude stratopause is warmer than at mid-latitudes, and in January it is even warmer than in summer. Thus, there is clearly considerable dynamical control of the high-latitude, winter, stratopause temperature structure. In the high-latitude, winter mesosphere, there is only a hint of a temperature inversion, i.e., in January. However, a small temperature increase occurs in October just below 90 km, much as it does at mid-latitude. Its disappearance in November with bigger solar zenith angles fits better with chemical heating than with dynamical heating, and thus supports that explanation for the 90 km inversion layer seen by the sodium lidars at mid-latitudes in winter [Senft *et al.*, 1994; She *et al.*, 1995].

Between 80 and 90 km, our temperatures confirm the findings by sodium lidars [Senft *et al.*, 1994; Yu and She, 1995] that the temperatures are not as cold as suggested by the MSIS90 model; the differences can be as large as 20 K. One consequence is that we find that the mid-latitude summer mesopause is at a lower altitude than in the MSIS90 model. Another consequence is that the deduced meridional circulation, which is so important for explaining the upper mesospheric temperatures, would be different from what has been deduced using the MSIS90 model. This problem arose, basically, because of the lack of good temperature data between 80 and 110 km. That problem remains unresolved and with the exception of special rocket campaigns, can only be solved by a combination of resonance-scatter lidars and the next generation Rayleigh-scatter lidars.

In addition to the above differences between our temperatures and the MSIS90 temperatures, we also found differences with the SME temperatures and with the temperatures from the sodium lidars. In

the summer comparisons between 50 and 70 km, the SME temperatures were systematically hotter than the others by 5–6 K, while in the stratopause region, they were systematically colder. Invoking diurnal tides, the solar-activity cycle, and long-term trends, we could not resolve the discrepancy. Our speculation is that it may arise from a small altitude error in the SME data reduction. However, the shapes of the temperature profiles are very similar to the others. Hence relative measurements may still be very good. In comparing annual temperature variations among techniques, we found that in the upper mesosphere near 85 km, the Rayleigh lidars, and SME found larger variations than the sodium lidars. Enough data were averaged together, in time and altitude, that the differences are statistically significant. Because the Rayleigh lidars are operating at the top of their altitude range and the resonance lidars are operating at the bottom of theirs, this difference looks suspiciously like an instrumental one. Rayleigh measurements at high altitude can be compromised by instability of the PMT background level, as pointed out by several authors [Keckhut *et al.*, 1993; Singh *et al.*, 1996; this study]. On the other hand, the resonance measurements of temperature, particularly near the upper and lower boundaries of the sodium layer, can be adversely affected by noise errors in what has been essentially a two-point fit to the complex sodium resonance spectrum. These potential measurement problems will best be investigated with co-located Rayleigh and resonance lidars making simultaneous observations, and by using the next generation Rayleigh lidar with its much improved signal such that 85 km is no longer at the top of the altitude range.

Thus, we have obtained very useful information from our mid-latitude temperature observations. We have also indicated how to improve the results by obtaining more observations (more frequent and over more years); by moving to the next generation Rayleigh lidar; and by making simultaneous, co-located Rayleigh and resonance observations. However, while temperature observations are extremely useful for learning about the middle atmosphere, even more progress can be made if we could simultaneously measure the winds throughout the middle atmosphere. We could then directly examine, for instance, the filtering process and the relationship between temperature inversions and turbulent layers. This case has been made eloquently by Whiteway and Carswell [1995]. In many ways, the lidar technique stands where the incoherent-scatter radar technique stood almost 30 years ago, when it first

became possible to make ion-velocity observations and, therefore, to deduce electric fields and to some extent neutral winds. There is much to do, and the tools exist for doing it.

## CHAPTER 6

## COMPARISON OF OBSERVATIONS AND MODEL CALCULATIONS

**1. Introduction**

There exists a strong link between temperature, radiative processes, and chemistry in the middle atmosphere. Solar radiation leads to temperature changes. These temperature increases can then induce an increase in thermal cooling, which moderates the impact of the increased heating on temperature. Thermal changes also lead to changes in the dynamics and can be associated with significant changes in the mean circulation and in waves of all scales.

Radiative changes ultimately affect chemical species through modification in transport by the eddies or mean circulation, and through changes in the production/loss rates either by temperature dependent reaction rates or by feedback of the changes in the chemical composition. Changes in the distribution of photochemically active gases can impact radiative heating/cooling and affect the dynamical structure of the middle atmosphere via temperature changes.

Within the upper mesosphere and mesopause region, energy, momentum, and atmospheric constituents are redistributed by the mean circulation and gravity wave forcing. The importance of dynamic sources such as gravity waves, tides, and planetary waves in determining both large-scale circulation and temperature structure and small-scale eddy and molecular diffusion is widely recognized. Upward propagating gravity waves, tides, and planetary scale waves can break and deposit momentum and energy, mix composition, enhance radiative cooling [Ward and Formichev, 1993] and chemical heating [Mlynczak and Solomon, 1993], and significantly influence the photochemistry of the region through the vertical transport of minor species via eddy diffusion [Garcia and Solomon, 1985]. Modification of thermodynamic equilibrium results from adiabatic cooling at summer latitudes and heating at winter latitudes via a mesospheric circulation. The circulation is driven by the interaction of gravity waves with winds and tides and their ability to deposit energy in the mesosphere [Lindzen, 1981]. Those gravity waves that are not filtered out in the stratosphere propagate from the troposphere and generate this diabatic circulation through wave breaking and dissipation processes. Energy and momentum may be exchanged throughout the region due to the same gravity wave breaking and dissipation [Vincenz, 1984;

*Hauchecorne and Maillard*, 1990], heat flux from overturning gravity waves in the upper mesosphere [*Walterschied*, 1981], tidal breaking in the mesosphere [*Groves and Forbes*, 1984], and meridional excursions of planetary waves to mid-latitudes [*Hauchecorne and Maillard*, 1990], thereby modifying the vertical distribution of temperature. Thus, the seasonal variation of the mesopause temperature depends more on the variation of the rate of deposition of momentum from below through the breaking of small-scale gravity waves propagating into the mesosphere than on the variation of the rate of radiative heating, especially at high-latitudes.

As an example, during the equinoctial period, while the stratospheric zonal flow is reversing direction (with both eastward and westward flows coexisting at different heights within the stratosphere), the stratospheric filtering imposed on eastward and westward traveling gravity waves reduces the strength of the pole-to-pole circulation cell in the mesopause region. This filtering system is less severe during the solstices, but a summer-winter difference does exist. Thus, eddy diffusion and wave drag are much stronger in summer and winter and weaker during the equinoxes [*Garcia and Solomon*, 1985]. Such variability in transport has important consequences for the seasonal and latitudinal distribution of constituents in the region as diffusive control of species may surpass photochemical control at times.

Considerable progress in modeling the mesopause region has been made during the past decade with the inclusion of gravity wave breaking and dissipation [e.g., *Lindzen*, 1981; *Holton*, 1983; *Fritts*, 1984] and the contribution of tidal wave and tidal wave fields into circulation models of the upper mesosphere and lower thermosphere [e.g., *Miyahara and Forbes*, 1992; *Hagan et al.*, 1995]. These processes can be further examined by making detailed comparisons between observations and first principles model calculations. Identifying and distinguishing tidal effects from gravity wave effects is difficult because both are present in the observations as well as interactions among the prevailing winds (including planetary waves), tides, and gravity waves. It is the absence or presence of these interactions that is expected to modulate the propagation of the tides through the mesosphere. Changes in atmospheric transport associated with seasonal changes in gravity wave breaking will affect seasonal and latitudinal distributions of chemical species at upper mesosphere and mesopause heights. A

convenient feature of this region is the occurrence of various airglow emissions that provide an indication of the chemical and dynamical structure.

In this chapter, an analysis of the current state of understanding of these middle atmospheric processes is conducted by comparing observations to a first principles global circulation model. In principle, a fully coupled, three-dimensional model that calculates the mean circulation, eddy forcing, and chemical evolution is sufficient for studying the state of the middle atmosphere [Garcia and Solomon, 1994]. We are able to take advantage of multiple co-located instruments that can make observations of three separate variables—temperature, horizontal wind velocities, and airglow emission intensities—in order to simultaneously compare results of very different types of processes.

The model we used is the TIME-GCM [Roble and Ridley, 1994]. Observations included airglow intensity collected by an imaging Fabry-Perot interferometer (FPI), horizontal winds at 87 km deduced from these measurements, and temperatures from lidar observations, taken approximately 40 km from the FPI, but well within the field of view. The OH intensity comparisons involved developing a photochemical model of the mesospheric OH layer and calculating the emission intensities. The model was initiated with temperature and mixing ratio values from the TIME-GCM.

An important aspect of these comparisons is that there are several of them. If there were just one, then a model can often be adjusted to account for it or, similarly, many plausible explanations can be found. However, this is a complex coupled system. The atmosphere responds in a variety of ways to perturbations in solar or wave forcing. Taking advantage of nearby instrumentation which provides several types of observations greatly limits the range of possible interpretations. Another important aspect of these comparisons is that they extend over four seasons: winter and summer solstices, spring and fall equinoxes. Hence annual variations in forcing functions (e.g., solar radiation) and filtering functions (e.g., gravity wave filtering by the mesospheric jet) can be examined. Again, this limits the possible range of interpretations.

The analysis consists of four sets of tests:

- 1) Temperature profiles. This involves many aspects of the system: radiation, dynamics, and chemistry. The average temperature in the lower mesosphere is going to be greatly dependent on absorption of



solar energy by  $O_3$  and on radiation to space by  $CO_2$ . In turn, the concentration of  $O_3$  will be greatly dependent on the  $O_3$  chemistry. In the upper mesosphere, dynamics becomes crucially important in several ways. For example, the global circulation directed from summer to winter leads to the cold summer mesopause and hot winter mesopause. Also, the role of gravity waves, which are excited at much lower altitude and give rise to this global circulation and a temperature inversion frequently seen in the winter mesosphere between 65–75 km. It also involves chemistry at much higher altitudes, where a small peak in the profiles has been associated with chemical heating, mostly from  $O_3 + H \rightarrow O_2 + OH$ .

2) Time variation of temperature. This involves the generation, primarily, of semidiurnal tidal variations in tropospheric  $H_2O$  and in stratospheric  $O_3$ , and their propagation to higher altitudes. The generation could vary with season because of a variety of factors including mixing ratio and solar radiation. The upward propagation could be affected by a variety of factors, including the background wind, planetary waves, tides, and gravity waves.

3) Winds at 87 km. The underlying wind pattern is due to radiative forcing, but it is greatly modified by the transfer of momentum from breaking gravity waves. This comparison will be largely a test of gravity wave effects. It differs from the tests involving the temperature profiles in that it is more direct, includes both the meridional and zonal components, and provides precise and accurate measurements at a higher altitude. The gravity waves are necessary for closing the mesospheric jet, which is observable in the background wind. Tidal patterns, normally present in the mesosphere, may also be disrupted by gravity waves as they travel through the region.

4) Intensities at 87 km. This is a test of both chemistry and dynamics. As will be discussed, the OH intensity arises from  $O_3 + H \rightarrow OH^* + O_2$ . However, the  $O_3$  and H densities depend on the breaking gravity waves. Availability of atomic hydrogen depends on turbulent mixing from below while that of atomic oxygen depends on diffusive transport from above. Accordingly this comparison tests another aspect of the role of gravity waves.

The lidar and FPI observations are discussed in Section 6.2. The TIME-GCM model used in the work is discussed in Section 6.3. The calculations of the OH intensities involve a separate model that was developed

specifically for this work. It is discussed in Section 6.4. The results are presented in Section 6.5 and discussed in Section 6.6. Conclusions are presented in Section 6.7.

## 2. Observations and Data Analysis

### 2.1. Rayleigh-Scatter Lidar

The Rayleigh-scatter lidar provides nighttime relative density and absolute temperature profiles from 40 to ~100 km. The profiles are acquired by emitting a laser pulse into the atmosphere and counting the backscattered photons as a function of time, returned to the collecting receiver at the ground. Temperature profiles are recovered from density profiles assuming hydrostatic conditions for an ideal gas then integrating downward from the top altitude using a model or other observations for the top temperature as the constant of integration. Range gating allows for discrete vertical temporal increments enabling the derived temperature observations to provide information on what happens to gravity waves and tides in the stratosphere and mesosphere. The USU Rayleigh lidar has been described in Chapter 4.

### 2.2. The Imaging Fabry-Perot Interferometer

An imaging Fabry-Perot interferometer (FPI) [Rees *et al.*, 1989] located at the Bear Lake Observatory (BLO, 41.93°N, 111.42°W, 2-km alt.) provides relative intensity of the OH Meinel (6, 2) P<sub>1</sub>(3) emission line at 843 nm. Airglow emissions (nonthermal radiation emitted by the earth's atmosphere as a result of chemical reactions) allow ground-based observations that reflect the state of the atmosphere in the region of emission. The Meinel vibrational-rotational spectrum [Meinel, 1950] of hydroxyl (OH) dominates the airglow near the mesopause region and arises from the photochemistry of atomic and molecular oxygen, atomic hydrogen, and ozone. These species develop significant concentrations in the mesopause region as determined by a combination of photochemistry and thermodynamics specific to the region and the constituent, thus OH emissions are normally confined to a specific layer of the atmosphere. Both in situ and satellite-based observations suggest the OH layer to be centered at 87 km with an average thickness of 6 km [Baker and Stair, 1988; Lowe *et al.*, 1996]. Basic agreement of OH winds to MF radar wind observations supports the assumption

that OH observations do provide a good measure of what is happening in the vicinity of 87 km [Wickwar *et al.*, 1997b]. Mesospheric winds derived from the FPI OH observations [Wickwar *et al.*, 1997b] provide insightful information on the tides and gravity waves reaching the mesopause (or at least reaching 87 km).

The imaging Fabry-Perot interferometer uses an optical path difference between different segments of a light beam to create a characteristic interference pattern. These natural emissions measured by the FPI come from species that tend to reach statistical (thermal) equilibrium with the surrounding media, making it possible to observe both variations of intensity and wind in the region of emission. Emissions from the upper atmosphere are typically weak; therefore, to avoid strong daytime Rayleigh-scattering interference from sunlight, we restrict the Fabry-Perot interferometer measurements to nighttime only. The FPI is well suited for airglow research due in part to its large spectral resolving power and its sensitivity.

The OH (6,2) observations were made with an imaging FPI using 15 cm,  $\lambda/200$ , thermally controlled plates with 20.49 mm zerodur spacers; a five-position filter wheel for 2-inch filters; an ITT imaging detector with a 25 mm, GaAs photocathode and a resistive anode; a Peltier cooler; and a water/glycol heat exchanger. The etalon chamber is slightly evacuated, the effective f-number of the system is 10, and the detector is cooled to  $-30^{\circ}\text{C}$ . The OH filter is centered at 843.2 nm and is 1.0 nm wide. The two-dimensional fringe pattern is circularly integrated to make a one-dimensional spectrum.

Data were acquired between November 1991 and June 1995 from the FPI and between August 1993 and July 1995 from the lidar. Temperature observations were averaged over 3 km. A detailed analysis of the lidar temperature observations was discussed in Chapter 5. Details of the FPI instrumentation, methods for extracting OH intensities, and the derivation of winds have been previously documented [Rees *et al.*, 1989; Vadrails, 1993; Wickwar *et al.*, 1997b; Monson, 1997].

### 2.3. Data Analysis

Intensities are measured at a  $30^{\circ}$  elevation angle and at eight azimuths each  $45^{\circ}$  apart. The usual integration time in each position is 4 minutes with a full set of observations every 40 minutes. All eight positions were combined to construct a single intensity curve for the night. Background intensities are normally uniform

across the entire sky (intensities  $\sim 15$  counts/sec) and have been removed. OH winds were combined to give a zonal and meridional component for each hour. These nightly curves are further averaged over several nights into monthly mean values interpolated for each hour.

Seasonal means were obtained by averaging nightly USU lidar profiles or BLO FPI data (both intensity and winds) over a 3-month period centered on the 15th of December, March, June, and September, thus representing the mid-point of winter, spring, summer, and fall, respectively. A 1-month average centered on the same date is computed in order to discern any characteristics that may show up over a shorter averaging time period. For hourly averaged curves at a particular altitude, data were sorted into 1-hour bins, representing only those data collected over the same 1-hour period each night, then averaged into 1-month and 3-month seasonal means.

Wind measurements are made by measuring the Doppler shift of the OH emissions. The Doppler shift corresponds to the line-of-sight (LOS) motion of the emitting layer so it must be resolved into the desired components. In order to obtain wind and intensity curves from OH measurements, it is assumed that the emission layer resides at a constant altitude, the average horizontal wind field is uniform, vertical winds are small compared to the horizontal winds (i.e., nearly zero), and the wind field changes smoothly in time (i.e., no discontinuities). The eight positions observed by the FPI make it possible to examine the uniformity of the wind field. Sets of three LOS speeds are used to derive the vector wind in different parts of the sky. For instance, observations to the NW, N, and NE can be combined to estimate the vector wind in the north; observations to the N, NE and E can be combined to estimate the vector wind in the northeast. These vector winds are then averaged into monthly zonal and meridional components as deduced from the LOS measurements for the night. As with intensities, seasonal values represent an average over the months of the season.

Temperature measurements from the USU lidar are represented as 1- and 3-month mean profiles. The 1-month profiles were obtained from averaged all-night profiles and monthly hourly-mean curves taken from 1-hour averages during each night. In the latter method, the data representing a 1-hour period were collected within the specified hour beginning on the hour. The 3-month profiles are averages of the monthly profiles for

the three months inclusive of the season. although these seasons do not match the observation-based seasons presented in *Wickwar et al.* [1997b].

### 3. Model Calculations of Temperature and Winds

The theoretical specification of temperature, composition and circulation relies on simulations from the three-dimensional thermosphere-ionosphere-mesosphere-electrodynamics general circulation model (TIME-GCM), described in *Roble and Ridley* [1994] and *Roble* [1995]. The TIME-GCM is a physics-based global one-dimensional model that extends from 30 to 500 km and includes sufficient physics and chemistry for the thermosphere, ionosphere, and middle atmosphere. The model was developed in order to examine the mesosphere-thermosphere region and allow for dynamical, chemical, and radiative couplings and provide a focus on the interaction between the dynamics and chemistry of the airglow region without major boundary influences. The main forcings within the model include solar EUV and UV heating and a specification of the amplitude and phase of the propagating diurnal (1,1) at the lower boundary and zonally symmetric annual tide. No semidiurnal tide is specified so any semidiurnal structure present is generated by interactions with gravity waves and in situ generated tidal components within the model. Planetary waves are not included. The only adjustable parameters are the assumed eddy diffusion profile and the Prandtl number. Wave drag was first introduced into the model as a Rayleigh friction parameterization uniform in latitude and longitude. Since simulations completely damped the diurnal tide or failed to close the zonal mean jet due to the omission of gravity wave-tidal interactions, the Rayleigh friction was soon replaced by the gravity wave parameterization developed by *Fritts and Lu* [1993]. This parameterization specifies the momentum deposition, heating, and turbulent energy associated with gravity waves interacting with the general circulation, and uses a latitudinal variation of gravity wave flux energy in order to ensure closure of the jet and production of the semidiurnal tide in the upper mesosphere. The model solves for distributions of temperatures, velocities, and chemical compositions in the stratosphere, mesosphere, ionosphere, and thermosphere. It calculates longitudinal variations in composition associated with wave dynamics similar to structures observed from UARS. The eddy diffusion profile is designed to obtain agreement of calculated H<sub>2</sub>O, CO, O, O<sub>3</sub>, and Ar with profiles from observations.

In order to simulate the double minimum in winter mesopause sodium lidar temperature profiles, a complex radiative balance was required consisting of  $\text{CO}_2$  and O infrared cooling,  $\text{O}_3$  heating, heating from exothermic reactions, gravity wave heating and turbulent cooling [She *et al.*, 1995]. A winter gravity wave energy flux four times larger than the summer value was required for the model to mimic the observed climatology.

The TIME-GCM was run under solar cycle minimum and geomagnetic quiet conditions during two geophysical conditions: perpetual equinox and December solstice. The assumption of latitudinal symmetry enables winter (northern hemisphere) and summer (southern hemisphere) outputs from the same model run to provide a consistent set of calculations for the three seasons: winter, summer, and equinox. With only one equinox, there is no allowance made for any equinoctial asymmetry. The results for BLO and its southern hemisphere stand-in were extracted from the global results.

#### 4. OH Intensity Model

We developed a kinetic model that populates the vibrational levels of active  $\text{OH}(\nu)$  using parameters extracted from the latest version of the TIME-GCM and then calculates OH emission intensity from these values. These input values included latitude- and longitude-specific vertical profiles of  $[\text{H}]$ ,  $[\text{N}_2]$ ,  $[\text{O}_3]$ ,  $[\text{O}_2]$ , and  $[\text{O}]$  in addition to temperature,  $T$ , and winds for the BLO location. The TIME-GCM includes the solution to the transport equation for  $\text{O}_3$  (previously not included) in addition to O and  $\text{O}_2$ . Thus we have elected to use these values of  $[\text{O}_3]$  rather than solving for  $\text{O}_3$  explicitly using a separate continuity equation. Figure 21 shows the profiles of the species of interest as produced by the TIME-GCM at 0700 UT for winter. Thus, at least part of the variation in intensity should be consistent with the dynamical behavior. We then compare the results to those measured from the BLO facility.

The OH bands arise from vibrational transitions within the ground electronic state. Molecules can store energy in rotational and vibrational states as well as electronic states. This ability leads to multiple rotational transition lines occurring within each vibrational transition, resulting in vibration-rotation bands and thus allowing molecules to possess more complex emission spectra than atoms.

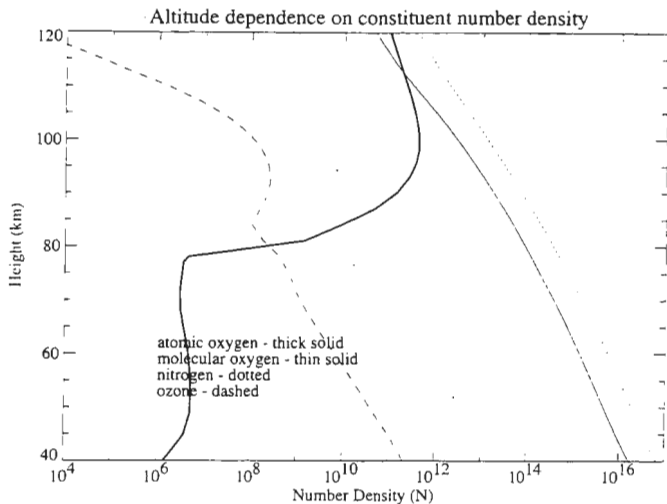


Figure 21. Profiles of the species of interest calculated by the TGCM at 7 UT for winter.

In the ground state, each molecular band contains three branches, P, Q, and R, based on angular momentum selection rules where  $\Delta J = -1, 0$ , and  $1$ . Each branch holds two subbranches due to the effective total orbital angular momentum about the internuclear axis. Beyond these splittings of the molecular band spectra, a hyperfine structure can be observed in certain molecules, resulting from the interactions of the nucleus with the orbiting electron.

Within the OH band system, a single vibrational transition and its associated rotational transitions permit the P, Q, R bands with substates  $1(\pi_{3/2})$  or  $2(\pi_{1/2})$ . Most of the hydroxyl emissions are radiated from the transitions of  $v' \leq 9$ . The nighttime OH emission described in this research is the Meinel (6,2)  $P_1(3)$  line at 843 nm, which is the third line in the  $P_1$  branch of the  $6 \rightarrow 2$  ( $v'-v''$ ) vibrational transition spectrum. With sufficient spectral resolution, the OH hyperfine structure can be observed.

The number density of  $\text{OH}(v)$ ,  $N_v$ , is determined by the continuity equation

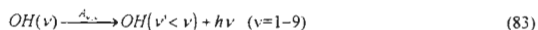
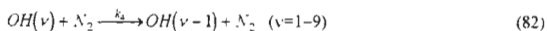
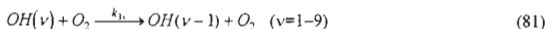
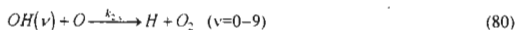
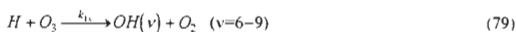
$$\frac{\partial N_v}{\partial t} = Q_v - L_v N_v - \text{div}(N_v \mathbf{V}) \quad (78)$$

where  $Q_v$  the production rate for vibrational level  $v$ ,  $L_v$  the loss rate for level  $v$ , and  $\mathbf{V}$  the velocity field which includes friction and the thermal, eddy, and molecular diffusion coefficients.

Bates and Nicolet [1950] first suggested that vibrationally excited OH was a product of the reaction of ozone with atomic hydrogen. Production terms for vibrational state  $v$  include the reaction of hydrogen atoms with ozone, collisional cascading from higher levels, and radiative transitions from higher levels. Destruction processes include radiative transitions to lower levels, collisional cascading to lower levels, collisional quenching (deactivation of  $\text{OH}^*$ ), and chemical reaction with oxygen (which also deactivates  $\text{OH}^*$ ). Our OH intensity model generates a one-dimensional photochemical model that populates the number density profiles of excited OH for levels 9–1. Successive values of the concentration of species of interest are calculated by employing a step function in the equation. Combined with a set of chemical and photochemical reactions and the appropriate reaction rate constants, numerical simulations of OH emissions are created.

#### 4.1. Modeling the OH

To populate OH vibrational levels ( $v=1-9$ ), we used the following reactions.



#### 4.2. Source Mechanism of the Meinel System

This cycle of the hydrogen-oxygen family of reactions is considered to be the basic chain for OH nightglow emission in the mesosphere. The main source of  $\text{OH}^*$  is via the exothermic reaction (Equation 79)



where the resultant OH is in an excited state. This may be followed by either chemical deactivation by atomic oxygen (Equation 80), vibrational quenching through collisions with the background gas, particularly O<sub>2</sub> and N<sub>2</sub> (Equations 81, 82), or radiative cascade to lower vibrational states (Equation 83).

The principal reaction (Equation 79) allows production of OH at vibrational levels down to  $v=6$  preferentially populating levels 8 and 9 and, to a lesser extent, levels 7 through 4 [Streit and Johnston, 1976]. The lower vibrational states are populated primarily by the cascading of energy from higher vibrational levels and collisional quenching from the level immediately above rather than direct excitation [Le Texier et al., 1987].

Although it is widely accepted that Equation 79 is the major source of OH emission, repeated claims suggest a secondary chemical source of vibrationally excited hydroxyl must also be involved:



for  $v \leq 6$  modes. Attempts to confirm the involvement of this additional chemical source have been hindered by conflicting evaluations of the absolute Meinel band transitions probabilities and inadequacies in understanding how the OH vibrational distribution is controlled by radiative cascade, vibrational (collisional) deactivation, and chemical removal processes. There remains much controversy among theorists over the role of this reaction in the production of the OH nightglow. Opinions vary from the belief that the reaction does not produce vibrationally excited OH [Llewellyn et al., 1987; McDade and Llewellyn, 1987] to the belief that the vibrational levels are limited to the lower states [Kaye, 1988; Lopez-Moreno et al., 1987]. It has been suggested, however, [Le Texier et al., 1987] that differences between observations and models in the lower vibrational states (e.g.,  $v=6$ ) may arise due to the influence of this secondary production source. More recent examination of this process suggests its importance to be minimal. Johnston and Broadfoot [1993] modeled the perhydroxyl reaction and found that OH peaked at 80 km, 10 km lower than the peak using Equation 79. The extreme collisional quenching at this lower altitude would allow only a ~1% contribution from this reaction to the total OH nightglow. The belief that this secondary production reaction is assumed to produce insignificant levels of vibrationally excited OH together with the opinion that this mechanism is of relatively minor importance in the production of excited OH at night [Makhlouf et al., 1995] leads us to consider its role negligible in our model.

Assuming no background wind ( $I=0$ ) and unperturbed, steady-state conditions where  $\text{OH}(\nu)$  is in photochemical equilibrium [Le Texier *et al.*, 1987], the OH densities in the  $\nu$  vibrational level are given by the ratio of production over loss:

$$[\text{OH}(\nu)] = \frac{b_\nu k_{1\nu} [H][O_3] + k_{3,4(\nu-1)}^M [\text{OH}(\nu+1)][M] + k_{2, \nu-1} [\text{OH}(\nu+1)][O] + \sum_{\nu' > \nu} A_{\nu, \nu'} [\text{OH}(\nu')]}{\sum_{\nu' < \nu} A_{\nu, \nu'} + k_{3,4(\nu)}^M [M] + k_{2(\nu)} [O]} \quad (85)$$

where  $M$  is the density of the major species, i.e.,  $O_2$  and  $N_2$ ;  $k_\nu$  are the reaction rates,  $b_\nu$  is the branching ratio for the initial excitation, and  $A_{\nu, \nu'}$  are the Einstein coefficients for the spontaneous emission from  $\nu \rightarrow \nu'$ . This is an iterative process in which solutions of the higher excitation values are needed in order to find lower excitation densities. Obviously collisional cascade and radiative transition from higher levels will not contribute to  $\nu=9$ , but these will contribute at the levels  $\nu < 9$ , i.e., in order to get  $[\text{OH}(6)]$  one must first solve for  $[\text{OH}(9)]$ ,  $[\text{OH}(8)]$ , and  $[\text{OH}(7)]$ , respectively.

Determination of hydroxyl quenching mechanisms requires the knowledge of the production rate ( $k_1$ ) and branching ratios of the hydrogen-ozone reaction ( $b_\nu$ ), the radiative transition probabilities for the excited states ( $A_{\nu, \nu'}$ ), and the vibrationally dependent quenching coefficients ( $k_\nu$ ). While it is generally accepted that the reaction between ozone and atomic hydrogen is the major source of vibrationally excited OH [Johnston and Broadfoot, 1993], problems remain as to the extent to which collisions between the vibrationally excited OH radicals and the major atmospheric species  $O_2$ ,  $N_2$ , and  $O$  contribute to the production and loss of each level.

The rate coefficient and temperature dependence for the initial excitation is given by Rodrigo *et al.* [1991]. The branching ratios, which determine the shape of the vibrational distribution, are not clear. Various sets have been deduced and modified [e.g., Llewellyn and Long, 1978; McDade *et al.*, 1987] based on the inclusion or exclusion of Equation 85, thus allowing populations of level  $\nu=9$  down to  $\nu=6$  or below. While all sets scale somewhat with  $\nu$ , in our model, we populate vibrational levels  $\nu=9-4$  using the branching ratios of Ohoyama *et al.* [1985].

#### 4.3. Radiative Transition (Einstein) Coefficients

The OH\* produced can radiate (Equation 84) single quantum level ( $\Delta v=1$ ) or multi quantum level ( $\Delta v>1$ ) emission, with a transition probability of  $A_{ul}$  ( $s^{-1}$ ). The radiative transition probabilities determine the shape of the radiative cascade distribution and the absolute column density of an excited species given its emission density [Johnston and Broadfoot, 1993]. Reasonable agreement exists in much of the OH literature for the set of relative transition probabilities determined experimentally by Murphy [1971] rather than the more uncertain theoretical set of absolute values calculated by Miles [1974]. The problem in determining precise values of the transition probabilities lies in the estimation of the molecular wavefunctions necessary for the solution of the electric dipole moment integral from which the transition probabilities can be calculated. Transition probabilities were calculated by Turnbull and Lowe [1989] based on measurements of the dipole moment combined with airglow observations in order to determine the electric dipole moment function. Their published total radiative loss rates ( $\Sigma A_{ul}$ ) at  $T=200$  K [Turnbull and Lowe, 1989] are used in this model as shown in Table 8.

**Table 8.** Thermally Averaged Einstein Coefficients  $A_{ul}$  ( $T$ )

$v'$	$T_{rot}$ (K)	$v'' = v'-1$	$v''=2$	$v''=3$	$v''=4$	$v''=5$	$v''=6$	Total
1	200	22.74						22.74
2	200	30.43	15.42					45.85
3	200	28.12	40.33	2.032				70.48
4	200	20.30	69.77	7.191	0.299			97.56
5	200	11.05	99.42	15.88	1.315	0.051		127.7
6	200	4.00	125.6	27.94	3.479	0.274	0.010	161.3
7	200	2.34	145.1	42.91	7.165	0.847	0.063	198.4
8	200	8.60	154.3	59.98	12.68	2.007	0.230	237.8
9	200	23.72	148.9	78.64	19.94	4.053	0.620	275.9

#### 4.4. Quenching

Quenching processes govern night airglow emissions near the mesopause. Radiative transition probabilities of the excited molecular states are so small in comparison to the collision frequencies at the altitudes where airglow is present, that quenching severely depopulates these states. Le Texier et al. [1987] found the inclusion of quenching of OH\* by O and the collisional deactivation of OH\* by O<sub>2</sub> and N<sub>2</sub> improved

comparisons between their modeled results and observations. Collisional quenching may account for up to 80% of the loss of  $\text{OH}^*(v=9)$  while radiation accounts for 15% and O quenching only 5% [Johnston and Broadfoot, 1993].

#### 4.5. Collisional Deactivation

Disagreement exists over the reaction rate coefficients for collisional deactivation of vibrationally excited OH, mostly centered on the way the deactivation is treated. In many earlier Meinel band studies, a conventional model of vibrational distribution was generally assumed. In this model, referred to as the collisional cascade model, vibrational distribution is controlled by radiative cascade and all collisional losses due to the major atmospheric species,  $\text{O}_2$  and  $\text{N}_2$  (Equations 81, 82), correspond to single-quantum vibrational deactivation steps. Any losses due to atomic oxygen were assumed to correspond to either chemical reaction or complete deactivation to the  $v=0$  level. An alternate approach, sometimes referred to as the sudden death model, assumes that all collisional losses result in the total removal of vibrationally excited OH species. Therefore, quenching by M may entail either the step-wise loss of a single quantum of vibrational excitation, multi-quantum loss, or reactive deactivation of  $\text{OH}^*$  [Dodd *et al.*, 1990]. It is not yet possible to identify the preferred model.

McDade *et al.* [1987] compared both models and found that in the conventional model, a reasonable vibrational level dependence of the vibrational deactivation coefficients was exhibited similar to those obtained in previous studies. By using the sudden death quenching model, the apparent dependence between vibrational level and the total loss coefficients can be only explained if the reaction  $\text{HO}_2 + \text{O} \rightarrow \text{OH}(v) + \text{O}_2$  is involved as a sink for vibrationally excited OH. Their results suggest that for the collisional cascade mechanism to be acceptable, the radiative lifetime of  $\text{OH}(v=9)$  would have to be shorter than  $\sim 15$  ms and for sudden death mechanism to be acceptable, it must be shorter than  $\sim 3$  ms.

Additionally, there are those who determine a collisional quenching rate employing the total atmospheric density [e.g., Johnston and Broadfoot, 1993], thus combining  $\text{N}_2$ ,  $\text{O}_2$ , and other atmospheric species into one reaction, or include a temperature dependence with the rate coefficient [e.g., McDade *et al.*, 1987], or a

vibrational dependence [e.g., Dodd *et al.*, 1991], or extrapolation and interpolation between measurements [e.g., Makhlouf *et al.*, 1995], or even a combination of one or more of these methods.

We have followed the approach and values found in Makhlouf *et al.* [1995] in combining results from various works to arrive at a set of vibrationally dependent quenching coefficients for Equations 82 and 83. Finlayson-Pitts and Kleindienst [1981] have shown that  $O_2$  collisional quenching is more than 20 times faster and more efficient than  $N_2$  in removing all vibrational levels and although we have included reaction 6 in our model, its reaction rates are a factor of  $\sim 25$  less than the corresponding rate for reaction 5. Atomic oxygen is not an effective quencher of  $OH^*$  compared with  $O_2$  since  $[O]/[O_2]$  is  $\geq 1$  only above 100 km and this ratio decreases rapidly with decreasing altitude ( $\sim 0.01$  at 90 km) [Howell *et al.*, 1990]. Our model used the conventional single quantum approach and the collisional cascading values of Johnston and Broadfoot [1993].

The dominance of the collisional quenching of  $OH^*$  has important repercussions to the contribution of the perhydroxyl reaction to the nightglow. The modeled peak of the perhydroxyl reaction is at  $\sim 80$  km, 10 km less than the modeled peak of the hydrogen-ozone reaction. Because of the relatively low altitude of this reaction, the quenching by  $m$  is extreme, which implies the perhydroxyl mechanism contribution is at most only  $\sim 1\%$  of the OH Meinel night airglow [Johnston and Broadfoot, 1993]. Deactivation by ozone is negligible for nightglow [Le Texier *et al.*, 1987]. The vibrationally dependent quenching rate coefficients will affect the shape and magnitude of the vibrational population.

#### 4.6. Chemical Deactivation

Chemical deactivation by reaction with atomic oxygen plays a minor role, mainly at altitudes above the emission peak. In the nightglow emission layer centered around 85–90 km, this form of quenching is negligible compared to radiative cascade and collisional relaxation [Le Texier *et al.*, 1987].

Observations of the various hydroxyl emissions show little to no correlation, which implies that the emissions are uncoupled by quenching [Johnston and Broadfoot, 1993]. If a number of states populated by a single reaction were depopulated by a single process, the relative populations of these states should be constant. Thus a population variation within states populated by one reaction may only be obtained by having competitive

Table 9. OH( $v$ ) Production/Loss Reaction Rate Constants

Rate Constant	Rate	Reference
$k_1$	$1.4 \times 10^{-10} \exp(470/T) b_{v,i} \text{ cm}^3 \text{ s}^{-1}$	<i>DeMore et al.</i> [1985] where $b_{v,i}$ is the branching ratio(s) given by <i>Ohoyama et al.</i> [1985] $b_9 = 0.32, b_8 = 0.27, b_7 = 0.21, b_6 = 0.08,$ $b_5 = 0.06, b_4 = 0.06, \text{others} = 0.0$
$k_3$	$f_{v,i} \times 10^{-13} \text{ cm}^3 \text{ s}^{-1}$	multiple sources* where $f_{v,i}$ is the branching ratio $f_9 = 170., f_8 = 98., f_7 = 54., f_6 = 30.,$ $f_5 = 17., f_4 = 8.8, f_3 = 5.2, f_2 = 2.7, f_1 = 1.3$
$k_4$	$3.3 \times 10^{-11} \text{ cm}^3 \text{ s}^{-1}$	<i>Westenberg et al.</i> [1970]

\**Dodd et al.* [1990] ( $v=1-6$ ); *Knutsen and Copeland* [1993] ( $v=7-8$ ); *Chalamala and Copeland* [1993] ( $v=9$ ).

multiple sink paths. The observed decoupling is probably caused by secondary sinks of chemical removal by O and radiative cascading which may be significant [Johnston and Broadfoot, 1993]. Meriwether [1989] suggested that the O quenching of OH\*, low  $v$ , is near the top side of the OH nightglow layer and collisional quenching of OH\*, high  $v$ , is near the bottom side, thus producing an observed separation of the OH( $v'$ ) profiles. Reaction rates and coefficients used in our model, as well as the relative branching ratios, are given in Table 9.

#### 4.7. Model Summary

This model populates hourly density profiles of OH( $v=9-1$ ), based on the continuity equation for OH( $v$ ) using temperature and number density profiles of the constituents extracted from the TIME-GCM model, and reaction rates as listed in Table 9. The profiles extend from 75–115 km with discrete vertical steps of 1 km each and are separated into three seasonal periods: wintertime, summertime, and the equinoctial seasons.

#### 4.8. Intensity Determinations

Once OH( $v$ ) profiles are determined, the model then provides simulations of emission in the OH(6,2) band. The volume emission rates or intensities,  $I_{v,v'}$ , between two vibrational states are simply the product of the population density of the upper vibrational level,  $N_v$ , with the corresponding Einstein coefficient,  $A_{v,v'}$ ,

$$I_{v,v'} = A_{v,v'} N_v. \quad (86)$$

But we would like the  $P_1(3)$  line emission radiance of the OH(6,2) band emission intensity. This is the third spectral line of the  $3/2\pi$  ( $J'-J=1$ ) spin state of the OH(6,2) band where  $J=5/2$  and  $J'=7/2$ . In order to calculate the intensity of a specific rotational vibrational spectral line emission, we need

$$I_{JJ'} = A_{JJ'} N_J \quad \text{such that} \quad I_{\omega} = \sum_{JJ'} I_{JJ'} \quad (87)$$

where  $A_{JJ'}$  represents the rotational-vibrational Einstein coefficient and  $N_J$  the population of the vibrational state  $J$  of the total population  $N_v$ . In other words, not only does the number density of the OH(6) state need to be found, but the OH(6) $_{J=5,2}$  state must be determined from this value

$$N_{J'} = \frac{N_v 2(2J+1) \exp[-E_J / kT]}{Q_r} \quad (88)$$

where  $E_J$  is the energy of the specified rotational-vibrational level (the energy of the upper  $v$  state rotational value) and  $Q_r$  is the rotational partition function in band  $v$

$$Q_r = \sum_{J'} (2J'+1) \exp[-E_{J'} / kT] \quad (89)$$

summed over all rotational states in the band. We have chosen to use the rotational-vibrational Einstein coefficients of *Turnbull and Lowe* [1989] and the upper state rotational term values of *Coxon and Foster* [1982]. The next step is to try to combine the theory and observations.

## 5. Results

In this section, the mean seasonal temperature and horizontal wind components are compared with reference temperatures and winds from the TIME-GCM. Seasonally averaged observations of OH emissions are compared with those calculated from the OH emission intensity model described in the previous section. This is not an attempt to "tweak" the model into fitting our observational results, but rather to discern any discrepancies between the model and observations and draw conclusions from them.

### 5.1. Temperature Profiles

In presenting the comparisons, it should be emphasized that the extensive analysis of the USU lidar temperatures in Chapter 5 assures us that the lidar profiles are very accurate and compare extremely well to observations provided from other measurement techniques. Therefore, we could say the lidar temperatures are

the reference values and the model temperatures are being compared to these. Figure 22 contains four plots showing temperature profiles for all four seasons. Each plot contains three profiles representing local midnight conditions (7 UT) identified as: 1-month average from the USU lidar (dashed line), 3-month average (solid line), and seasonal curve (dotted line) from the TIME-GCM. During all four seasons the observations of the lower mesosphere and stratopause are cooler than the TIME-GCM by 6–8 K.

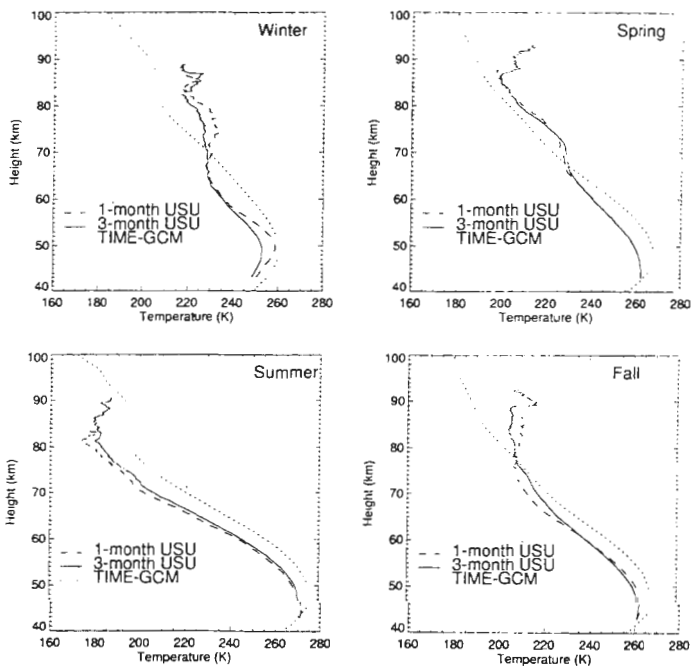


**Figure 22.** Temperature profiles for the four seasons. Each season contains three profiles, a 1-month (dashed line) and a 3-month (solid line) average from the USU lidar observations from 40 km to near 90 km, and a reference curve (dotted line) from the TGCM empirical model. All temperature curves portray local midnight conditions (7 UT).



In summer, there is good qualitative agreement between the structure of the observations and the model in which temperatures decrease monotonically from the stratopause up to the inversion at 82 km. The TIME-GCM appears to overestimate temperatures throughout the profile by 6 K near the stratopause and nearly 10 K in the upper mesosphere, near 85 km. The temperature bulge near 85 km—seen in both observed and modeled profiles—is attributed to chemical heating. The minimum near 100 km—seen in the model—is from strong CO<sub>2</sub> cooling from collisions with O [Roble, 1995]. The 1-month summer (June) lidar profile is cooler than the 3-month average by 3 K throughout much of the mesosphere as expected since the coldest annual mesopause temperatures occur during summer solstice.

During winter, spring, and fall the lidar and model temperatures show significant disagreement above the mid-mesosphere as warming is taking place in the lidar profiles. Above this region (65–75 km) the lidar temperatures switch from being cooler than the model to warmer than the model with a difference of nearly 20 K at the tops of the profiles. The winter lidar profiles reveal an inversion at 65–75 km. This inversion is stronger in the 1-month (December) average and is often seen in winter profiles at this altitude range [Schmidlin, 1976; Hauchecorne *et al.*, 1987; Hauchecorne and Maillard, 1990; Clancy *et al.*, 1994; Meriwether *et al.*, 1994; Whiteway *et al.*, 1995]. The winter inversion has often been associated with gravity wave activity in the mesopause. The variability of the inversion from night to night and year to year will be smoothed during the averaging process but the fact that it is present in the average attests to its strength. The TIME-GCM on the other hand, shows no indication of an inversion in the 65–75 km region and indicates only a minor warming above 80 km.

In spring, the lidar profile suggests a stratopause that is slightly lower than that seen in the model although this is difficult to confirm without lidar observations below 40 km. Midway up the profile, remnants of the winter inversion remain in the lidar observations, although it is weak, while the model has no sign of any heating taking place. Near the top of the profiles during both fall and spring, the mesopause appears near 85 km, confirming sodium lidar observations for equinox conditions (see Chapter 5), but occurs much higher in the TIME-GCM (above 100 km).

In discussing the seasonal differences between the model and the lidar temperatures, we can further demonstrate the variations with a comparison between the TIME-GCM and other atmospheric models. In Figure 23 we compare TIME-GCM temperature profiles with profiles taken from the lidar and two other atmospheric models, the MSISE90 and a NASA-GSFC model. The NASA-GSFC is a physics-based, time dependent, three-dimensional, spectral global circulation model incorporating both tidal specification, gravity wave forcing, and a parameterization of the  $O_3$  distribution. The MSISE90, as mentioned in Chapter 5, is an empirical model based on various observational methods. These models were used to simulate seasonal average temperatures for  $40^\circ N$ .

This comparison is shown to emphasize the general disagreement among the models themselves in both the winter and the summer middle atmosphere temperatures. In summer, the greatest variation occurs in the vicinity of the mesopause, from 80–100 km. In this region there is no similarity among the models and the temperature difference between profiles reaches nearly 40 K at 87 km. In winter, the models show as much variation but on a wider extent. Temperature differences are not as large as in summer but the dissimilarity among the profiles appears throughout the mesosphere. None of the models produce a winter profile significantly equal to the lidar temperature, including the heating that occurs in the inversion layers.

## 5.2. Hourly Averaged Seasonal Mean Temperature

In the absence of critical levels or gravity wave activity, upward propagating tides may reach the upper mesosphere. At these higher altitudes, tidal amplitudes are reasonably large and may contribute to large atmospheric fluctuations. Analysis of hourly averaged temperatures, winds, and airglow emissions through the nighttime observing period at several altitudes help determine the presence or influence of tides at the observed altitude. Tides may also emerge as pseudo-tides whereby interactions of gravity waves with the tides may enhance the tidal amplitude [Walterscheid, 1981]. If no distinct tidal period is seen, one may infer that interactions between tides and gravity waves or tides and background winds caused the propagating tide to dissipate before reaching the observation height.

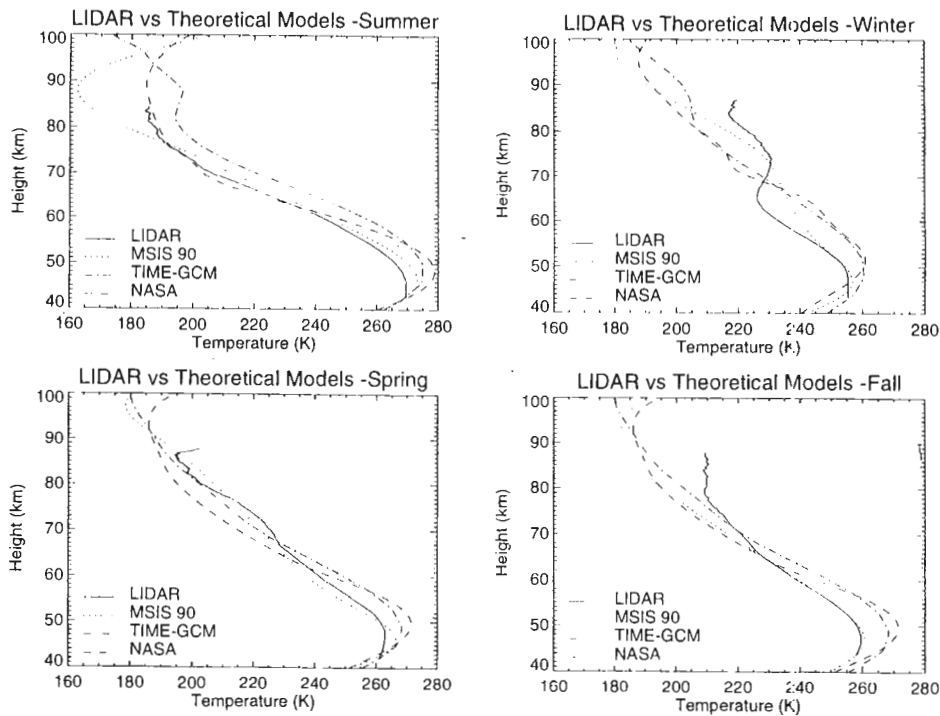


Figure 23. Comparison of TIME-GCM seasonal temperature profiles with profiles from USU lidar, the MSIS90, and NASA-GSFC model.

The next four figures (Figures 24–27) show the nighttime hourly average, seasonal mean temperatures at six altitudes between 55–80 km. The curves are identified as: 1-month average (dashed), 3-month average (solid), and TIME-GCM values (thick solid). Each figure represents one season. Initial analysis indicates a diurnal variation below 70 km in the model temperatures for all seasons, with a phase that moves earlier with increasing altitude (consistent with a downward phase progression).

Wintertime curves are shown in Figure 24. The lidar values are consistently cooler than TIME-GCM temperatures below 70 km and warmer above, as noted earlier in the temperature profiles. The remarkable aspect of these plots is that, even with considerable variability in the lidar values, the general phase and period of the lidar temperature curves below 75 km are similar to diurnal period of the TIME-GCM at these altitudes. The 3-month lidar temperature average is smoother than the 1-month average suggesting that with larger data sets, the lidar curve may closely resemble the TIME-GCM curve. (It is difficult to draw many conclusions about the curves at 80 km because of the large variability in the winter lidar observations at this altitude.) The wintertime TIME-GCM diurnal tide has a 40-km vertical wavelength and by 75 km a semidiurnal period has replaced the diurnal mode. This is consistent with lidar measurements in France in which a semidiurnal tidal mode was reported up to 80 km [Gille *et al.*, 1991]. At 80 km an 8-hour period is present.

In summer, there is little resemblance between the phase of the lidar and that of the TIME-GCM. The summer diurnal tide of the TIME-GCM has a very shallow diurnal amplitude and a tidal phase progression with altitude, while the lidar temperature variation has a larger amplitude and a phase regression with height noticeable from 65–80 km that appears to move in the wrong direction. The reverse phase gradient of the lidar temperatures suggests there is tidal mode mixing or reflection or the presence of very short wavelengths. If there is a semidiurnal period in either the observations or the model for equinox or summer, it is very difficult to interpret between 75–80. Although higher modes may develop in summer, the amplitudes may be in the noise.

For spring and fall, Figures 26 and 27, the TIME-GCM features a diurnal period throughout the altitude range and a phase progression with altitude in agreement with an upward propagating diurnal tide. The similarity that exists in spring between model and lidar temperatures at 60 and 55 km begins to fade by 65 km. At this height, the lidar temperatures exhibit a spring maximum between 8–9 UT while the TIME-GCM

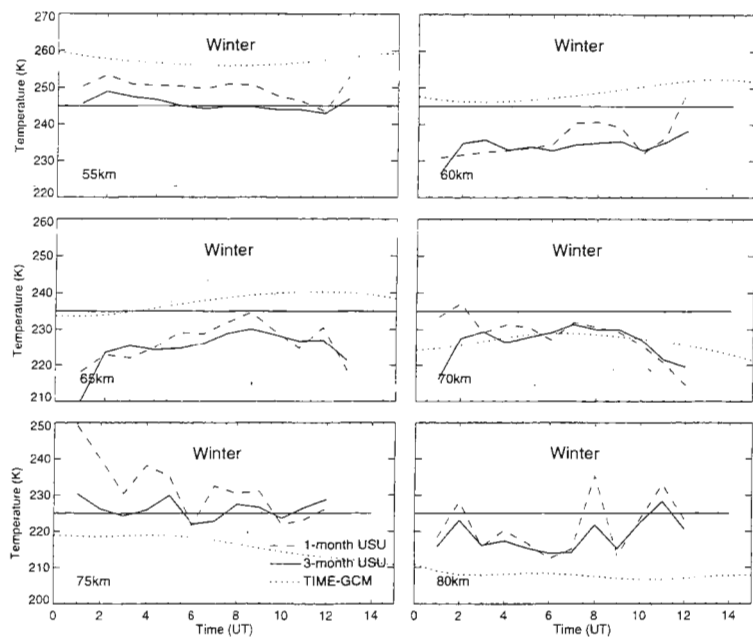


**Figure 24.** Nighttime hourly average, winter mean temperature values at six different altitudes between 55–80 km. The three curves: 1-month average, 3-month average, and TGCM values, for a 50 K temperature range.

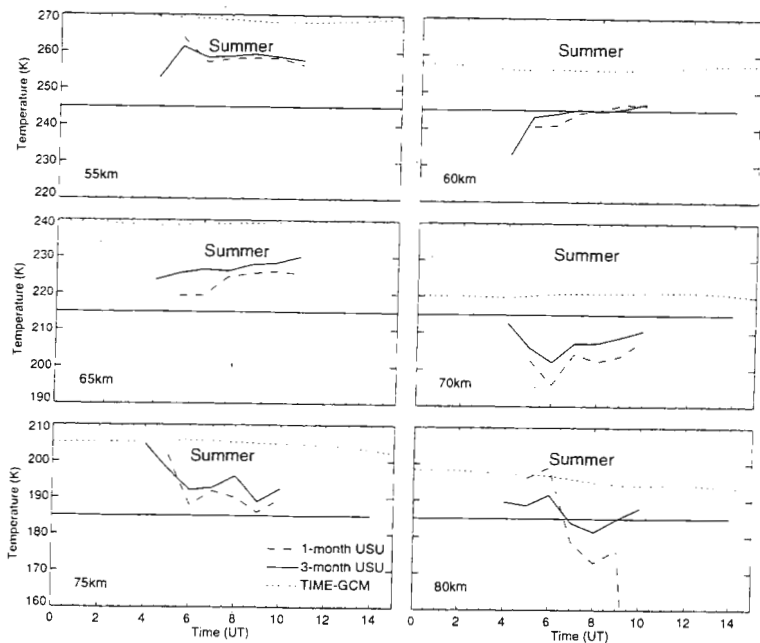


**Figure 25.** Nighttime hourly average, summer mean temperature values at six different altitudes between 55–80 km. The three curves: 1-month average, 3-month average, and TGCM values, for a 50 K temperature range.

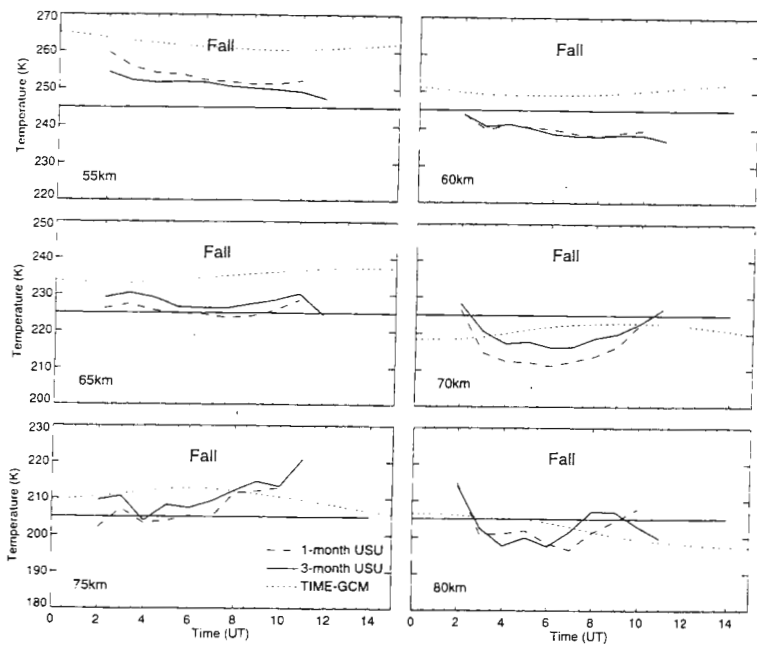


**Figure 26.** Nighttime hourly average, fall mean temperature values at six different altitudes between 55–80 km. The three curves: 1-month average, 3-month average, and TGC values, for a 50 K temperature range.

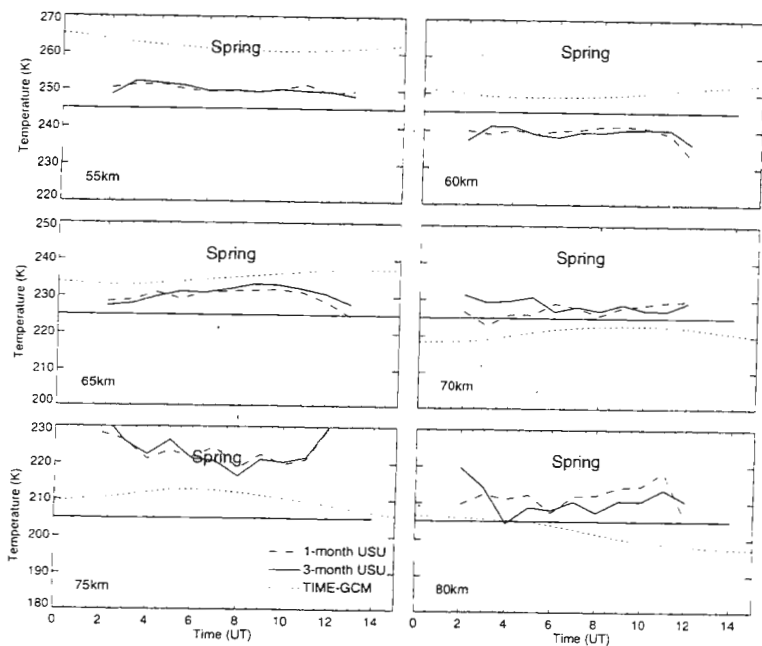


**Figure 27.** Nighttime hourly average, spring mean temperature values at six different altitudes between 55–80 km. The three curves, 1-month average, 3-month average, and TGCM values, for a 50 K temperature range.



maximum occurs closer to 14 UT, demonstrating a phase difference of 5 hours between the lidar and the TIME-GCM temperature curves.

While the model is the same for the two equinox periods, the two lidar curves show distinctly different results for fall and spring. The fall curves are similar in appearance only at 55 km as temperatures decrease from 2–11 UT, but with different values. At 65 km, the phases are no longer similar, as the fall USU temperature minimum occurs at 8 UT and the TIME-GCM minimum occurs 5 hours earlier at 3 UT. The lidar fall temperatures are noticeably cooler than the spring values at and above 65 km and the curves are nearly  $180^\circ$  out of phase, indicating a definite asymmetry in the tidal behavior between spring and fall. At 70 km, the minimum in the lidar data occurs at 6 UT, about an hour earlier than at 65 km, while the TIME-GCM minimum occurs near 00 UT, thus regressing 3 hours and indicating different vertical wavelengths. At 75 km, the fall temperature variation is almost  $180^\circ$  out of phase with the TIME-GCM.

### 5.3. Horizontal Wind Components

In Figure 28, we compare the seasonal TIME-GCM horizontal wind components at 87 km with the hourly-averaged, seasonal-mean OH meridional and zonal wind components. Eight plots are presented representing the four seasons with curves shown as: 1-month average (x's), 3-month average (solid line), and model (dashed). Assuming that the diurnal tide is small at this latitude and altitude, the background wind may be taken as the average between the maximum and minimum reported values.

The winter components are seen in Figure 28. Both model and observations have northward and eastward background winds consistent with global scale mesospheric circulation in winter. The OH observations show a northward wind of 7 m/s and an eastward component of  $\sim 6$  m/s similar to other observations at this latitude [see Wickwar *et al.*, 1997b]. The winter solstice reveals little periodicity in the OH winds and amplitudes are less than 10 m/s for both components. However, on a day-by-day basis, large variations with distinct periodic amplitudes are observed [L'adnais, 1993; Wickwar *et al.*, 1997b], suggesting that the large day-to-day variability of the semidiurnal tide excited during winter becomes modified as it propagates so as to be almost unrecognizable and randomized at 87 km. It is not clear whether this is due to a greater amount of

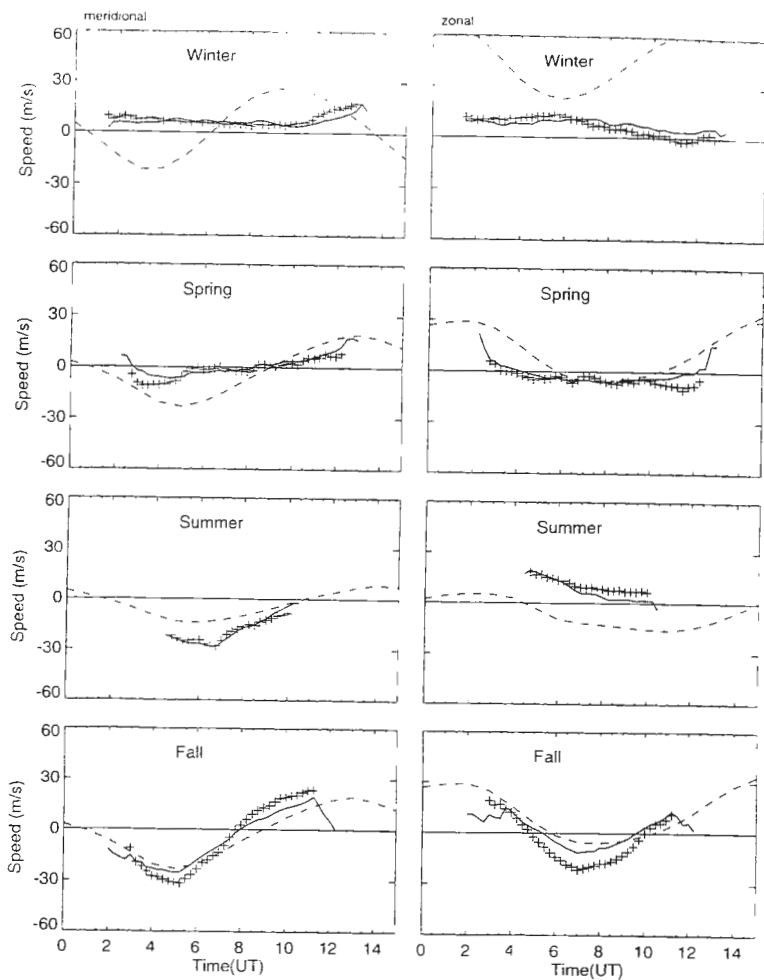


**Figure 28.** Time dependence of seasonally averaged meridional and zonal components of winds for each season shown as 1-month average (x's), 3-month average (solid line), and TGCM seasonal mean (dashed). Component winds for each season were extracted from the TGCM at 87 km and compared with the OH hourly averaged, seasonal-mean meridional and zonal wind components.

gravity wave activity during the winter at these altitudes or a filtering mechanism at work on the propagating tide in the lower mesopause or stratopause. It should be noted, however, that from 11–13 UT, there is an increase in the northward component, a phenomenon that, although weak, is real. The zonal component shows the same situation with a small but real maximum between 5–6 UT and a minimum near 11 UT in the 1-month average. This feature is less noticeable in the 3-month average. The model exhibits a distinct semidiurnal variation above 80 km for the zonal component and above 85 km for the meridional, so that the OH and TIME-GCM zonal winds are nearly four hours out of phase. Winds become westward briefly in the 1-month average near the minimum at 11 UT, but this is not observed in the smoother 3-month curve, suggesting this may be due to year-to-year variability in the tidal effects. In contrast, the TIME-GCM winds show a very strong semidiurnal mode in both components during winter. The zonal component of TIME-GCM, with its very strong eastward mean wind (~50 m/s), large amplitude, and a minimum between 7 and 8 UT, shows no similarity to the observed winds. On the other hand, the meridional component has a northward background mean centered at ~5 m/s similar to observations, but on top of which a semidiurnal variation is imposed with a phase of ~12 UT. In agreement with the model, HRDI observations also indicate a strong winter semidiurnal mode in the longitudinal mean at 87 km for 50°N but a maximum speed of only a 30 m/s eastward.

In the summertime (Figure 28), both model and OH winds have a southward direction in the mean background wind throughout the night, which is consistent with other sources of mid-latitude observations [Wickwar *et al.*, 1997b]. The observations favor a westward direction similar to mid-latitude summer upper mesospheric winds while the model tends to favor slightly an eastward wind. In fact, the TIME-GCM mean zonal background winds are eastward at 87 km for the entire year except during the summer, whereas OH background winds are eastward except for spring. The observations indicate the summer westward jet that is normally centered at 65 km has closed and reversed direction by 87 km. This reversal of direction at 87 km is not produced by the model during summer. The short observation period during summer makes it difficult to draw any conclusions on the amplitude or period. What we can tell is that the OH meridional wind component

phase occurs nearly an hour earlier than the TIME-GCM and the zonal components appear to be either out of phase with each other or in phase but with a greater eastward component than the observed winds.

Spring and fall appear to be transitory seasons. Spring marks the beginning of the seasonal meridional jet wind reversal from eastward in winter back to westward for summer. These summer westward winds begin weakening by October before switching direction again for winter. The OH winds are far from symmetric about the equinoctial periods. This is partly due to the rapid transition that takes place from winter to summer and vice versa within a one month period [Tsuda *et al.*, 1988].

The components for springtime show little resemblance between observations and model. In spring, the mesospheric jet undergoes a significant and rapid transition from winter to summer conditions, disrupting the tidal propagation during this period. This usually occurs in the March/April period. During spring, the either out of phase with each other or in phase but with a greater eastward component than the observed winds averaged OH background winds favor a *westward* direction, whereas the TIME-GCM produces a strong *eastward* component. Both model and observations indicate a southward background meridional component. While it is possible to extract a phase from the observations in April, it is difficult for February and March. Thus a phase is difficult to distinguish in the spring average for the zonal wind collected by the FPI. The meridional component begins to display signs of an oscillation that is out of phase with the TIME-GCM by 4 hours and a background value that is only slightly northward. This is compatible with the eventual progression to the southward summer pattern. In addition to these two comparisons, the results of Nielejewski and Killeen [1995] found a large amplitude semidiurnal variation in April and March unlike the BLO FPI data and also similar winter and summer amplitudes, again unlike our observations, but similar to the model.

The closest agreement between the observations and model occurs in the fall. Both model and observation illustrate a strong semidiurnal period with similar amplitudes. However, the TIME-GCM zonal component is moderately strong *eastward* all night versus the OH wind which oscillates from east to west through the night and is in fact, more *westward* during the nighttime in the 1-month (September) average. While the observed meridional wind has a larger amplitude than the model's results, the mean background

indicates a slight tendency toward a southerly flow for all curves. The model and observations are out of phase nearly 4 hours in the zonal component and 2–3 hours in the meridional component.

A neutral wind climatology for has been summarized by *Wickwar et al.* [1997b] in which three different seasonal periods and two transition periods are characterized each having a very distinctive behavior pattern. The seasonal variability is summed up as:

- 1) late summer (August and September): winds exhibit a strong semidiurnal tidal signature consistent over a large range of temporal scales to include with daily, monthly, and year-to-year averages.
- 2) summer (May–July): winds are variable from day-to-day but a semidiurnal pattern is observed often enough to show up in monthly and yearly averages.
- 3) winter (November–February): a semidiurnal pattern is observed occasionally but no particular pattern shows up consistently and the majority of nights are completely variable. Averaging over long periods tends to minimize any tidal structure. How this ties in to the inversion layer at lower altitudes is not understood.
- 4) transitional patterns in March–April and October.

The results of this climatology are similar to our seasons of fall, summer, and winter respectively. However, as we are using different months to represent the seasons in this dissertation, we lose some of the definition in the seasonal patterns as reported by *Wickwar et al.* [1997b]. In particular are the transition periods that are nominally very rapid and occur within a 1-month period. This transition period will no doubt greatly affect the appearance of the seasonal averages during the equinox.

Before moving on, let me illustrate an example of the usefulness of multiple observations using the temperature profiles of the lidar and the hourly mean wind averages. In winter, the seasonal temperature profiles maintain the appearance of an inversion through averages of many nights; however, the tidal variations, seen on a night-to-night basis in the OH winds, get averaged out in the seasonal hourly-mean. On the other hand, averaged summer temperature profiles tend to smooth out much of the observed nightly variation [*Bills et al.*, 1991], whereas the OH winds maintain the characteristics of a tidal variation when averaged over the summer. These two examples indicate the workings of two separate events during these two times of the year. Because of

the downward progression of tides through the night, a tidal variation may get averaged out in the nightly profile, assuming the observational period is long enough. But these same tides would show up very distinctly in the hourly plots if gravity wave forcing were weak. This appears to be the case in summer. Gravity waves on the other hand, have a random sequence of occurrence through the night. If the level of breaking is constant for a long period (e.g., weeks at a time), its effect will show up in the mean profile but would disrupt the tidal variations in the hourly mean plots. Such is the case with the winter observations. Thus there is more evidence of greater gravity wave activity in winter than summer.

#### 5.4. Relative OH Intensities

Comparisons of the observed hourly-mean, seasonal average OH (6.2) intensities and those generated by the TIME-GCM driven model, described in Section 7.4, are shown in Figure 29. The winter season seems to have the most distinct variation with an 8–10 hour period for both model and observations. However, the phase is  $180^\circ$  different (6 hours) between the two. This variation is curious since the observed winds show little to no discernible tidal node when averaged over the winter months, although the OH emissions do. Comparing the TIME-GCM winter wind component variations to those of the modeled intensities, one finds winds (both zonal and meridional) to have a 12-hour period and intensities to have an 8–10 hour period. In addition, the phase between the model intensity and the TIME-GCM winds are out of synch and there appears to be no correlation of the two parameters. Obviously, different mechanisms are at work in driving OH production and the winds at the same altitude.

In summer, both curves indicate that OH intensities decrease during the early part of the night. However, model OH intensities increase at the end of the night, a phenomenon not observed in the FPI data. The periods differ slightly with a semidiurnal oscillation for the observations and an 8-hour period for the model, though this is inconclusive with emissions of only 8-hour duration.

The closest resemblance between observation and model intensities occurs during spring equinox in what appears to be a semidiurnal period as intensities decrease during the first part of the night, reaching a minimum from 7–9 UT, then increase before sunrise.

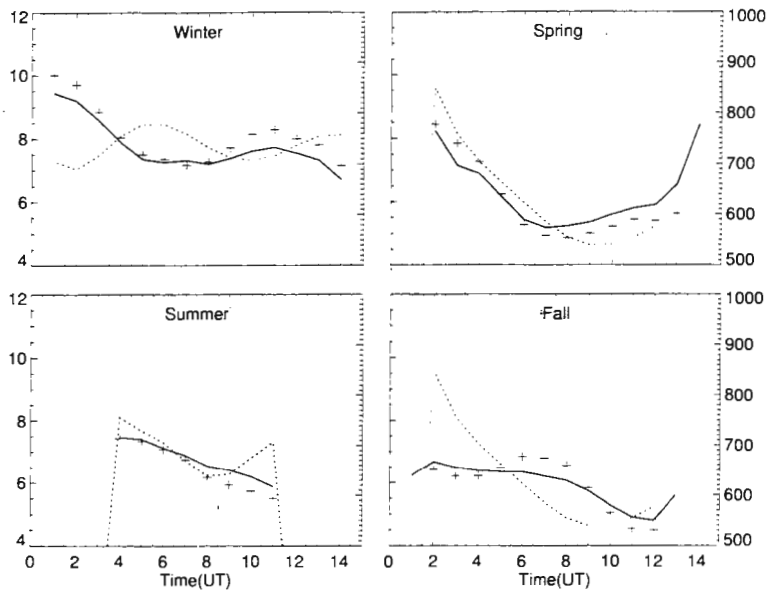


Figure 29. Comparisons of the hourly-mean, seasonal average OH (6,2) intensities from the FPI and model curves based on the TGCM driven model. The left side y-axis is in units of photons/sec for the FPI data while the right side y-axis is in Rayleighs/m<sup>2</sup> for the model calculations.

The fall period shows almost no agreement between the model and the FPI observations. The model curve for fall has the same appearance as spring and summer. An 8-hour period is suggested in the observations for the 1-month average but is less obvious in the 3-month average, which more closely resembles a semidiurnal period, as evident in the fall model intensities. In summer and fall, the model minimum occurs nearly 3 hours earlier than the observations, while in winter and spring, the FPI minimum occurs 2–3 hours earlier than the model.

The OH model has the strongest emissions occurring just after sunset in the summer and equinox while the FPI intensity observations have the strongest emissions after sunset during the two solstices and spring; thus winter and fall seem to be when most differences occur. The model intensities all show a minimum or "dip" occurring 2–3 hours before sunrise. It is uncertain whether this variation is due to seasonal transport and tidal motions or radiative and chemistry effects. It has been suggested [Lowe *et al.*, 1996] that the post-twilight exponential decay of OH may be attributed to chemistry. The atomic oxygen required to sustain OH production will be lost in its sink region below 86 km (from  $O + O_2 + M \rightarrow O_3 + M$ ) but remain fairly constant above. Thus the decay time constant of O (and therefore OH) is inversely proportional to the rate constant of the loss process.

Comparing the seasonal variation in modeled emission intensity, we see the greatest emission rates occur in winter and the lowest in spring and fall. This semiannual variation is opposite to the mid-latitude calculations made by *Le Texier et al.* [1987] in which the maximum intensities occurred during equinox. They argued that because atomic oxygen is controlled by dynamic diffusion above 87 km and chemical destruction below 87 km, slower diffusion during equinox would allow more O available at 87 km before reaching its sink region below 87 km. Thus, greater OH production occurs during this period. Their high-latitude findings indicated a maximum in winter resulting from greater advective transport in the 85–90 km region. However, our FPI intensities also show a maximum in winter thus suggesting that transport plays a greater role in the mid-latitudes than previously believed.

While the OH (6,2) emission layer is stable at 87 km [Baker and Stair, 1988; Lowe *et al.*, 1996], using species concentrations produced by the TIME-GCM, our model calculates an OH emission centered at 92 km



with a peak at 90 km (Figure 30). As with the winds, it is not yet known how this discrepancy in the OH peak altitude affects the intensity comparison between the model results and FPI observations.

Because the TIME-GCM generates an OH density maximum near 92 km, one may ask how winds at the predicted emission layer (92 km) matched the observed winds (from the OH layer at 87 km). These results, plotted in Figure 31, show that while many of the differences in the comparison with model results at 87 km are still noticeable, they are less severe. In fact, the fall period shows both components to be in excellent agreement in both phase and amplitude. The model equinoctial zonal components show more tendency for westward winds, summer more eastward, and winter remains eastward. Model winds have slightly larger amplitudes at the higher altitude as expected. The phase progression with height manifested in the model is enough to align the phase of the model winds at 92 km more closely with that of the FPI observations during summer and the equinoxes but the winter results are even further out of phase with the observations.

### 5.5. Discrepancies

Several discrepancies exist in the TIME-GCM when compared to observations of temperature, winds, and OH intensities. These include:

- 1) consistently warmer temperatures than the lidar in the stratopause and lower mesosphere;
- 2) except for summer, colder upper mesospheric and mesopause temperatures than the lidar values;
- 3) occurrence of the mesopause at 100–105 km for all seasons contrary to lidar observations and empirical models (e.g., MSISE90, CIRA 86), which indicate the winter and summer mesopause at 105 and 87 km, respectively, and a double minima at 87 and 102 km during equinox [Senft *et al.*, 1994; She *et al.*, 1993];
- 4) cooling above the summer inversion (80–87 km);
- 5) a winter inversion that is too weak and occurs at the wrong altitude (80 km vs. 65 km);
- 6) no inversion during equinox; and
- 7) phase differences in the hourly mean equinoctial temperatures between model and observations above 65 km. This phase difference is also an indication of the asymmetry between spring and fall seen throughout the various observations. The TIME-GCM uses a perpetual equinox thus prohibiting the detection of any spring fall asymmetry.

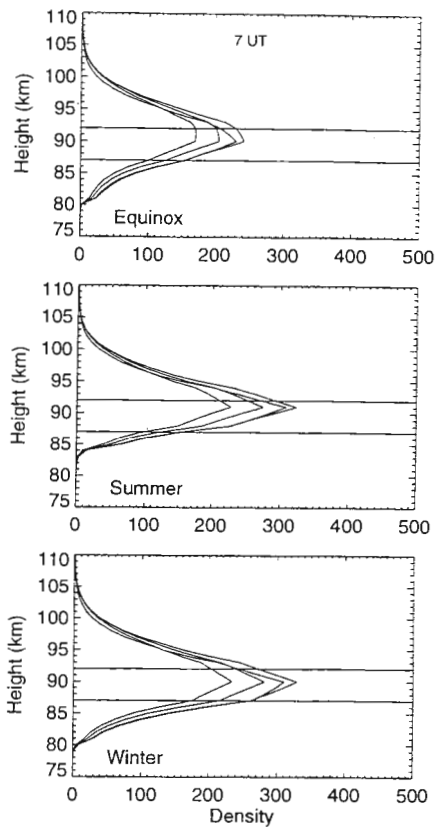
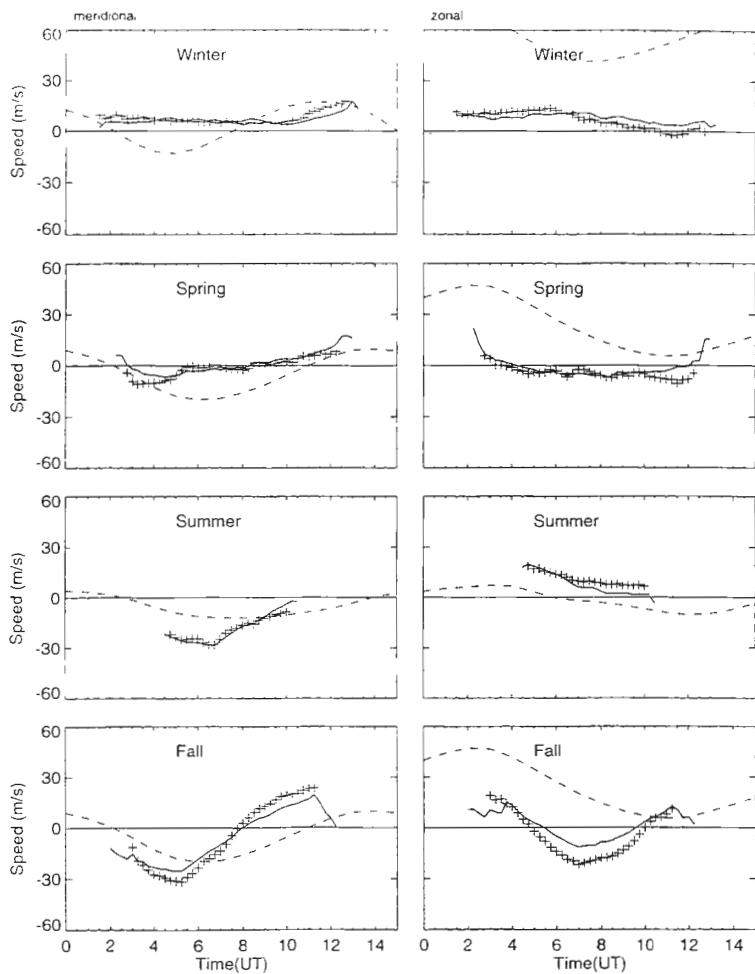


Figure 30. Calculated OH (9-6) densities based on the TGCM species concentrations.



**Figure 31.** Time dependence of seasonally averaged meridional and zonal components of winds for each season shown as 1-month average (x's), 3-month average (solid line), and TGCM seasonal mean (dashed). Component winds for each season were extracted from the TGCM at 92 km and compared with the OH hourly averaged, seasonal-mean meridional and zonal wind components.

Discrepancies in the TIME-GCM found in the wind comparisons include:

- 1) eastward zonal winds for the entire year except summer, whereas the observations indicate eastward winds except for spring, thus the observations allow closure and direction reversal of the meridional summer jet while the model does not;
  - 2) a distinct semidiurnal mode for both the zonal and meridional components in winter with large amplitudes, whereas observations have very shallow amplitudes for both components and a slight phase shift in the semidiurnal variation;
  - 3) much larger winter zonal background wind than observations imply;
  - 4) stronger fall zonal background wind than the observations with a slight phase difference between model and observations;
  - 5) excellent agreement between fall wind variations at 92 km in the model and observations at 87 km;
- and
- 6) the absence of a spring-fall asymmetry, as the observations show a larger amplitude in both fall wind components than evident in spring, and a zonal wind reversal between spring and fall, whereas the model cannot show these differences.

Discrepancies in the modeled OH emissions include:

- 1) the difference in periods during fall (8 vs. 12 hours);
- 2) phase differences between model and observations visible in winter, fall, and summer; and
- 3) strong increase in emission during the first few hours of the night, which does not always appear in the observations.

In the following section, we will address the inconsistencies between model and observations.

## 6. Discussion

Two primary causes may be responsible for the differences between model and observations: the interdependence of the dynamical, thermal, and chemical processes and insufficient or inaccurate terms, parameters, or boundary specifications. The parameters are not separate but part of a coupled system. The amount of wave forcing depends on, among other things, the mean zonal circulation. The radiative forcing will

be highly dependent on the chemical composition. Changes in the solar heating rate may trigger a response in temperature and circulation. These changes can be modified by feedback from gravity and planetary waves, which again depend on the mean wind and feedback to the temperature structure. Differences can be expected as the model must input fixed wave parameters at the boundaries, whereas in reality, tropospheric sources should generate a wide spectrum in wave number and phase velocities at the boundary region (however, arguments have been made [Garcia and Solomon, 1985] that only shorter wavelength gravity waves will propagate to great heights).

1) For instance, the annual modeled summer mesopause is too high, leaving the temperature variation near 87 km too small. This implies that the calculated global circulation, in particular the meridional wind, is too small, hence, decreased adiabatic cooling and warming in the mesopause region. This ties back to gravity waves whereby gravity wave breaking and forcing will drive the mesosphere away from radiative equilibrium through deposition of momentum in the zonal wind. An increase in gravity wave drag will strengthen the meridional circulation of the middle atmosphere, and through adiabatic warming and cooling, this cools the summer hemisphere and warms the winter hemisphere. Thus it is possible that the gravity wave-forcing mechanism of the model may be too small. An increase in wintertime gravity wave forcing will also allow closure of the meridional jet at an altitude consistent with our observations, reduce the tidal amplitude, and increase OH intensity after sunset in winter.

Differences can be expected as the model must input fixed wave parameters at the boundaries, whereas in reality, tropospheric sources should generate a wide spectrum in wave number and phase velocities at the boundary region (however, arguments have been made [Garcia and Solomon, 1985] that only shorter wavelength gravity waves will propagate to great heights). Garcia and Solomon [1985] found unreasonably large diffusion and momentum values due to their choice of wavelength and had to normalize their solutions to improve the model calculations. They also found that the diffusion and turbulence created by waves breaking at lower altitudes may cause structural modification to waves propagating through the region through wave-wave interactions.

Other factors also indirectly influence the gravity wave parameterization in models. The eddy diffusivity  $K_z$  is related to the gravity wave drag [Lindzen, 1981] and should in principle be altered as gravity wave parameters get modified in model simulations but the effectiveness of diffusivity on thermal and constituent fields is determined by the Prandtl number (ratio of eddy momentum to the eddy heat diffusivity). Is the modeled gravity wave parameter needed to close the mesospheric jets too large or small so as to inadequately handle the summer mesopause? There is evidence of an underestimated wave drag in summer as the model fails to reverse the zonal flow at 87 km. This is supported by the two-dimensional model of Garcia and Solomon [1985] in which they were able to reverse the summer easterlies above 85 km by increasing the gravity wave drag above 65 km. This leads to a stronger meridional circulation, a colder summer mesopause, and a warmer winter mesopause.

A clue could be in the horizontal wind components. Does the wind comparison support this interpretation of a weak meridional wind? Interestingly, the modeled winter zonal winds are strong at 87 km with large tidal variations. These high winds would result in greater than expected meridional winds. The summer zonal winds, however, are much weaker and should lead to weaker meridional flow. If this is the case, one would expect the model to give a much cooler mesopause in winter than summer due to the increased adiabatic cooling in the TIME-GCM winter hemisphere. But the model mean meridional component has nearly equal magnitude for both summer and winter and is much smaller in summer than that observed over Utah.

Additionally, two-dimensional model simulations have indicated that the strength of the meridional circulation depends on the ratio of Rayleigh friction and cooling [Garcia, 1987]. Together the dissipative processes of cooling and Rayleigh friction will decide if the atmosphere responds to forcing through a meridional circulation or changes in the mean zonal wind and temperature fields. If this ratio is under- or overestimated, the model may respond differently than the real atmosphere to a given forcing mechanism.

If meridional summer to winter winds agree (and they do), then circulation should induce the vertical winds and adiabatic warming/cooling unless heating rate is in error. Even with proper gravity wave flux values and circulation structure, this temperature difference may be underestimated if the radiative terms such as Newtonian cooling and the partitioning of solar radiation to allow for airglow emissions [Portman *et al.*, 1995]

are not properly accounted for. Difficulties occur in determining the airglow emission contribution because the heating efficiency of the  $H + O_3$  process is poorly understood. One must consider redistribution of atomic oxygen due to diffusive transport and varying ozone levels, normally observed to be higher in summer and weaker in winter [Meriwether and Mlynczak, 1995].

2) The model does not give rise to the "extra" heating high in the mesosphere in winter (or spring or fall). Does this "extra" heating account for the much larger seasonal variation in the data than in the model? And where would this "heating" come from?

The complexity of the inversion layer dynamics and the region of heating in the winter upper mesosphere remains a mystery. Exothermic reactions associated with  $HO_x$  chemistry provide heating above 80 km [Mlynczak and Solomon, 1993; Meriwether and Mlynczak, 1995] and  $CO_2$  infrared cooling balances ozone heating below 80 km. Dynamically induced heating (and cooling) from gravity wave-generated turbulence is expected to be small at equinox [She *et al.*, 1995] and summer but much stronger in winter as gravity wave sources are greater in winter and weaker in summer. Thus the heating below 80 km is believed by many to be caused primarily by the dynamics of the mesosphere and the strong meridional circulation.

Various dynamical effects have been postulated for the thermal sources of the heating mechanisms responsible for the formation of the inversion layer. Among the sources of heating, there are gravity wave breaking and dissipation [Vincent, 1984], dynamic cooling in topside mesosphere through downward heat flux due to overturning gravity waves [Walterscheid, 1981; Weinstock, 1982], thermal modulation based on nonlinear properties of convective overturning [Walterscheid and Schubert, 1990], energy deposited by breaking gravity waves over successive days [Hauchecorne *et al.*, 1987; Hauchecorne and Maillard, 1990], adiabatic heating from the meridional circulation [Hauchecorne and Maillard, 1990], and turbulent mixing [Whiteway *et al.*, 1995]. Thus, the initial input of the gravity wave flux from lower levels is essential in the overall atmospheric dynamics as it must also provide for the heating mechanism near the inversion layer. Are topographically induced gravity waves too location specific to be incorporated into a general circulation model or are they applied differently for various locations?

What is the role of a chemical heating mechanism on the region below 80 km? Several exothermic reactions may provide an equal or even greater rate of heat deposition in the heat budget of the mesopause region than direct solar radiation [Mlynczak and Solomon, 1993]. Of course, the available energy, whether acquired through radiation or exothermic reactions, may be reduced through airglow emission that decreases the heating efficiency of  $O_2$  and  $O_3$  solar absorption. If OH cooling is accounted for in the TIME-GCM, the height of the OH emission layer would be crucial in determining the overall temperature structure. Roble and Ridley [1994] acknowledge that stratospheric chemistry is limited for the TIME-GCM and crudely accounted for in the boundary conditions below. If the mesospheric effects (i.e., exothermic heating) of stratospheric or lower thermospheric reactions and their responsible constituents are not sufficiently understood or incorporated into the TIME-GCM, the temperature comparison would be poor. On the other hand, if a chemical source were the mechanism, why would the altitude of the layer not be stable year-round such as the airglow layers? In answer to that question, Bills *et al.* [1991] argue that no thermal peak is observed in winter because downward vertical circulation in winter prohibits transport of water up from its primary source in the stratosphere. So the mesosphere is drier in winter, hence a weaker chemical heating source and the absence of peak at 85 km. The two mechanisms may both be at work as the chemistry produces much of the heat energy and the dynamics related to gravity waves and tides redistribute the heat in accordance with a seasonal circulation pattern.

Does any evidence point to planetary wave activity in winter being responsible for the "heating" in the winter mesosphere? The TIME-GCM has no planetary wave input at the lower boundary even though it has been demonstrated [Huang and Smith, 1995] that increased planetary wave activity can decrease the mean zonal wind speed in the stratosphere. This then modifies the spectrum of gravity waves that can propagate into the mesosphere, thus weakening the meridional circulation and reducing the dynamical heating and cooling in the mesosphere. Thus, summer becomes warmer and winter becomes colder.

The possibility that planetary waves are responsible for the extra heating in the winter mesosphere has been considered in the analysis of the lidar data. The large difference between the January 1994 and 1995 monthly profiles (Figure 18) and, to a lesser degree, the February profiles for these two years indicates a large-scale transient perturbation. Although the exact mechanism is not known, because the temporal scale of the



temperature anomalies are consistent with those of planetary waves, we began a search for evidence of planetary waves. If these planetary waves, or Rossby waves, are responsible for the appearance of the wave-like pattern of the jet stream at the tropopause, it is feasible that one could trace this wave-like pattern into the middle atmosphere. As the jet stream pattern changed appearance, one might reasonably expect the temperature structure in the mesosphere to follow. By determining the state of the tropospheric and lower stratospheric regions, we could theoretically track these waves. This approach was attempted by conducting a case study for the two January periods using archived tropospheric wind data from the National Climatic Data Center (NCDC) with inconclusive results. A second consideration was to investigate a correlation of the temperatures between the tropopause (10–12 km) and the lower stratosphere (25 km) at several locations nearby the lidar site. Would planetary wave activity affect the correlation between the two layers? The assumption was that a long-term (~10 days) pattern in the temperature correlation would be detected thus providing additional support for the planetary wave theory of the inversion. Since archived data are only reported every 12 hours and the top altitude is erratic, many data sets reached only up to 16 km, thus making the comparison difficult. Again, the evidence to support this theory was not found.

Finally, the latitude variation of gravity wave energy flux specified in the TIME-GCM is based on measurements in Australia and Antarctica. The role of asymmetric hemispheric forcing of planetary waves was suggested by *Garcia et al.* [1992] whereby more realistic results were achieved in a two-dimensional model by using a weaker planetary wave forcing function in the southern hemisphere than in the northern hemisphere. If a parallel argument holds true for gravity wave energy flux—and there is no evidence that it should not—it could explain some of the solstice inconsistencies. In what parameters might this be most apparent? Further research should be conducted in order to determine what effect hemispheric differences of wave energy play in the global scale circulation and how these differences manifest themselves on the local scale.

There is also the question of the altitude of the “heating.” Dynamical sources should demonstrate a semiannual variability in accordance with the propagation of waves through the stratospheric critical layer. The breaking height will lie considerably higher for summer gravity wave propagation than for winter gravity waves as the spectrum of upward propagating waves is controlled by the stratospheric wind filtering [*Wilson et al.*,

1991; Taylor *et al.*, 1993]. If gravity waves break lower in winter, as has been demonstrated in Chapter 5, the meridional circulation should extend further down into the stratosphere during this time [Huang and Smith, 1995]. Thus maximum velocities will occur at lower altitudes, giving rise to a stronger winter inversion also at lower altitudes. Is this effect responsible for the seasonal difference in the mesopause altitude or the winter inversion layer observed between 65–75 km? A good check for future work would be to compare vertical velocities of the model with observations to fully understand the structure of the meridional circulation.

3) The higher model temperatures at the stratopause and in the lower mesosphere in all seasons suggest that the middle atmospheric chemistry may be deficient. Wave forcing can affect the distribution of chemical species directly through transport by the eddies or mean circulation, or indirectly by altering the temperature. Changes in the distribution of radiatively active gases can impact on radiative heating/cooling and affect the dynamical structure of the middle atmosphere. This can then allow changes in the production/loss rates either by temperature dependent reaction rates or by feedback of the changes in the chemical composition [Huang and Smith, 1995].

Suggestions for future studies might be to compare the model  $O_3$  to  $O_3$  from an empirical model. The impact of chemical changes, specifically  $O_3$ , on the temperature is large in this region due to the large ozone heating rate. Because  $O_3$  has a short lifetime in the upper stratosphere and mesosphere, it is influenced more by photochemical than transport processes. The effect of increased solar radiation is a greater temperature. This increased temperature accelerates the ozone destruction, thus lessening the amount of solar heating and then lowering temperatures. The process is complicated and if all the connections are not included, the results could be unreasonable. Another impact of the higher temperatures is greater scale heights that give rise to bigger densities of  $N_2$  and  $O_2$  at a given altitude in the upper mesosphere. This may be what leads to the peak of the OH emission coming from 92 instead of 87 km. This would also become the justification for looking at the winds at a higher altitude, e.g., 92 km instead of 87 km.

There is also evidence that increased radiative cooling occurs in the 65–100 km range due to the larger number of  $CO_2$  molecules observed than previously thought [Meriwether and Mlynczak, 1995]. If the TIME-GCM uses an insufficient  $CO_2$  profile, the temperatures in the region may be off. Calculations using increased

CO<sub>2</sub> densities show an increase in the meridional circulations due to changes in gravity wave filtering and diabatic heating [Portmann *et al.*, 1995]. The result is dynamical cooling in summer mesosphere and warming in winter mesosphere.

4) Another comparison is with the tides seen in the temperatures, winds, and OH intensities. If the TIME-GCM only includes a semidiurnal excitation from O<sub>3</sub> solar absorption, the omission of H<sub>2</sub>O solar absorption might explain the phase shift during winter and fall. (Recall that the superposition of two waves of the same frequency, but different phases, leads to a wave of the same frequency but at yet a different phase.) If the O<sub>3</sub> chemistry is wrong and there is a big diurnal variation, that might also explain a phase shift. Or, if the O<sub>3</sub> density is too big all the time, it would give too big an O<sub>3</sub> contribution to the semidiurnal tide compared to the H<sub>2</sub>O contribution. Whatever gives rise to a phase in the temperatures should also give rise to a phase shift in the winds. Are they in the same direction with roughly the same number of hours? Our winds are observed at 87 km while the noise in the seasonal hourly mean temperatures makes comparisons between the two at that height unconvincing. We suggest further research is needed into comparisons of temperatures and winds at the same altitude to analyze the phase difference between the two parameters and effect of H<sub>2</sub>O solar absorption on mesospheric tidal variations.

5) Another comparison involves the intensities, which show very large differences for all seasons. Many mechanisms have been suggested as being responsible including the seasonal changes in the solar zenith angle, meridional transport, vertical advection, and the annual periodicity of wave and vertical eddy diffusion activity. These mechanisms link the dynamics and the photochemistry of the mesopause region [Garcia and Solomon 1983, 1985], which then influence the OH densities.

The annual variation of intensity should be related to the gravity wave forcing and upward propagation. Physically, OH nightglow intensity variations should closely follow variations of the atomic oxygen mixing ratio, and therefore, should exhibit a similar seasonal variation [Le Texier *et al.*, 1987] to that of the vertical diffusion coefficient since vertical diffusion,  $K_{zz}$ , provides the primary transport of O downward from its source region in the 80–150 km region where it is produced by photodissociation of O<sub>2</sub>. Calculations of the eddy diffusion coefficient in the 80–100 km region show a strong semiannual period characterized by maxima during the

solstices and minima during the equinoxes [Garcia and Solomon, 1985]. The winter maximum is weaker than summer due partly to filtering of gravity waves in the stratosphere. Because diffusion is slow in spring and fall, atomic oxygen will build up in the 85–90 km region, and as the diffusion maximizes in winter and summer, the concentrations decrease around 85–90 km, even though the thermospheric source is strongest in summer. Le Texier *et al.* [1987] predicted dynamical signatures for the seasonal variation of the OH intensity for the mid-latitudes and found reasonable agreement between the modeled seasonal variations and the variations found in a limited set of ground based observations as well as a similarity between the concentration of O and the OH intensities.

Our observations as well as the modeled intensities are contrary to results of Le Texier *et al.* Our results indicate maximum intensities in solstice and minimum values during equinox. This strongly suggests a dependence on downward transport. Seasonal variability of wave-induced diffusion has important effects on distribution of chemical species. Since the mixing ratio of atomic oxygen increases rapidly with height in this region, convective transport of O due to medium-scale vertical winds [Clemesha *et al.*, 1991] in addition to eddy diffusion would allow a downward (upward) vertical wind to increase (decrease) the concentration of O and also increase (decrease) the atmospheric temperature due to adiabatic heating (cooling). At equinox the mesospheric zonal flow reverses direction, thus allowing the filtering of both westward and eastward gravity waves. With reduced wave activity in the mesopause region, the pole-to-pole circulation is weaker. This weak meridional circulation cell, together with the diffusion of atomic oxygen from the lower thermosphere, causes a buildup of O in the mesopause region [Meriwether, 1989], which is observed as an increase in the green line airglow intensity at equinox [Cogger *et al.*, 1981]. However, transport modeling in the mesopause region is difficult as planetary waves, thermal tidal modes, and the instabilities that generate turbulence and attenuate gravity waves are not well understood [Fritts, 1984]. Many questions remain unanswered. How is chemical transport handled by the model? Garcia and Solomon [1985] considered only vertical eddy transport for chemical species. What is lost by this limitation? Is the seasonal variation of gravity wave breaking properly affecting the distribution of chemical constituents? Is it possible that the gravity wave filtering system in the model also influences the meridional circulation and thus the vertical transport at mid-latitudes? If so, do these dynamical effects properly

lead back once again to the fact that dynamic variability in the mesosphere is closely related to gravity waves? Is a mechanism in place to allow feedback to the temperature or the winds, which also depend on gravity wave forcing? The question remains unanswered as to how the OH emission relates to what may be a chemistry-induced bump on the modeled temperature profiles near 90 km. Further studies on OH intensities and O profiles should address how well the OH intensity calculations parallel the TIME-GCM atomic oxygen density at 87 (or 92) km.

The nightly variations show major differences between model and observations. The diurnal process of OH production is driven by the availability of atomic hydrogen and ozone (oxygen) whose concentrations are influenced strongly by the processes that occurred when the atmosphere was sunlit and relax quickly after sunset [Rodrigo *et al.*, 1986]. Atomic hydrogen is controlled by upward diffusion of water vapor from the stratosphere and the subsequent production via daytime photolysis



Hydrogen may be recycled by



The concentration of H above 80 km shows little diurnal variation [Allen *et al.*, 1984]. Ozone, on the other hand, displays large diurnal variations within 70–85 km [Allen *et al.*, 1984] specifically at the terminator since ozone is rapidly depleted through reactions with solar radiation and with atomic oxygen. Ozone is produced mainly at night, especially at 80–90 km, through the three-body recombination



where M is an arbitrary third body, and depends on the availability of O. Ozone is short lived (except at the polar night region) at 85–90 km. Its loss depends on H concentrations and somewhat on O by



and dissociation during the day



Atomic oxygen produced via photodissociation of  $O_2$  in the daytime lower thermosphere by



is controlled at night by downward eddy diffusion from its source region. These daytime conditions determine the vertical distributions of the interacting species in the night. At night there is no photodissociation so production of atomic oxygen is independent of ozone and loss is controlled by the three-body recombination (Equation 15).

The limiting agent that controls the production of excited OH is the reaction that produces  $O_3$  at these heights, more specifically the availability of nighttime atomic oxygen. Therefore, because the nighttime supply of O atoms in the 60–90 km altitude region of OH emission is quite small, OH density is largely controlled by the atomic oxygen density [Le Texier *et al.*, 1987] rather than the reaction rate. But it is the general atmospheric circulation and temperature structure that determines the diurnal variation of the atomic oxygen as it is controlled by dynamics, specifically eddy diffusion, above 87 km and chemical destruction below 87 km. Less diffusion during equinox means more available O for OH production. Is this what is seen in the plots?

6) Another factor involves the  $N_2$  and  $O_2$  densities and the indirect influence they have on the emission layer. Quenching of OH by topside O and bottom side  $O_2$  and  $N_2$  would be felt most strongly at the lower altitudes, manifesting itself as an attenuation of the bottom side of the profiles and a raising of the peak altitude. How is quenching affected by gravity wave or tidal forcing? Does the response of emission reflect this? If the OH densities from the model are correct, is it possible that the  $O_2$  and  $N_2$  densities are overestimated, thus allowing for additional quenching at the bottom side? There is also the question of whether dynamics or tidal variations are being displayed in the OH intensities. As mentioned earlier, Lowe [1996] suggested a chemical cause for the post-twilight decay of OH. This sounds reasonable until one notices a definite wave pattern in the modeled winter intensities. Could this wave-like appearance be induced by processes elsewhere? This may not explain the reason for the increase in the pre-dawn intensities but does provide motivation for a future study.

One curious aspect arising from the multiple observations comes from a comparison of OH intensities and winds. Both are measured from the same altitude by the same instrument, but while the OH intensities

display an obvious tidal variation, the winds have an almost unrecognizable variation. This is further evidence of the fact that many processes may occur at the same location but affect the fields differently.

7) Another area of concern is the fall-spring asymmetry in the temperatures and winds. What might affect them both, but is not in the model? What has a long time constant? Gravity wave source? *Gille et al.* [1991] found strong diurnal and semidiurnal periods in mid-winter with much less pronounced tidal effects in early winter. Also, tides have been observed to undergo rapid equinoctial transitions from summer to winter as late as the end of November [*Tsuda et al.*, 1988], with strong phase transitions and significantly reduced amplitudes. The winter to summer transitions appear to occur rather quickly in the latter part of spring equinox [*Wickwar et al.*, 1997b] as observed in OH winds. Further evidence for the quick transitional period was reported by *Balslev et al.* [1983] in which MST radar echoes, attributed to the breaking of gravity waves, indicated a rapid transitional period between the solstice regimes. Thus, the appearance of very short, very quick transitional periods in the late equinox has the effect of carrying over some characteristics of the previous seasons. In other words, the spring will show a more winter-like appearance and the fall will show some characteristics of summer.

8) OH intensity and wind phase differences may be attributed to fluctuations in the height of the emission layer. However, these fluctuations seem unlikely as variations during equinox have only shown a change of 1 km or less [*Lowe et al.*, 1996]. A mixing of tidal modes may be another possibility. In the mid-latitude stratosphere and mesosphere, the propagating diurnal tide has small vertical wavelengths and therefore will not be dominant. The governing tidal mode at 85 km will be the semidiurnal mode for the mid-latitudes up to about 110 km. Although the diurnal tide is not a major component, it may still be observable along with the semidiurnal mode. Both are generally larger than the terdiurnal components, but *Teitelbaum et al.* [1989] argue that the terdiurnal component of the winds may be comparable to the diurnal mode during the winter. Thus, the phases observed in wind and intensities may contain a mixing of more than one tidal mode. This could be better determined with a complete spectral study of the OH observations.

## 7. Conclusion

We used the TIME-GCM as a reference model and compared temperature, wind, and OH intensity predictions with observations from a single location to investigate the effects of gravity waves, tides, and planetary waves in the mesosphere and mesopause region. Thus the combination of the Fabry-Perot and lidar observations gives us more insight into the interaction of gravity waves with the mean mesospheric flow than can be obtained from either instrument alone. The measurements were taken from multi-year collections of nighttime, hourly observations that were averaged into 1-month and 3-month seasonal means. The TIME-GCM simulated a mid-latitude location (BLO) for northern hemisphere winter and equinox and incorporated a gravity wave parameterization and tidal forcing in the lower levels. Summer values were calculated based on a symmetry in the model about the equator, and spring and fall were both considered to be represented by the equinoctial run of the model.

The overall comparisons showed many discrepancies. The TIME-GCM summer mesopause height is unlike mid-latitude observations; the inversion produced by the summer TIME-GCM is not normally observed by lidar or represented by other models (e.g., MSISE90); there is a spring-fall asymmetry present in the OH winds and lidar temperatures but the TIME-GCM treats the equinoctial periods as perpetual, allowing no difference between spring and fall; and a small, barely distinguishable tidal variation appears in the seasonal mean of the winter wind components, whereas the TIME-GCM has the greatest tidal amplitudes during the winter. During summer, the observations indicate the mesospheric jet has closed and switched directions but the model has only closed the jet and no directional change is seen at 87 km.

In the observations, winter winds display a great day-to-day variability but they approach a nearly constant wind when averaged over the season. At the same altitude, the winter OH intensities have a definite semidiurnal period in both the observations and the model but the post-twilight decrease in intensity was suggested as to be chemically driven. Model winds are much closer in agreement with observations when 92 km is used as a reference altitude; in fact the fall season observation and model results were nearly identical.

The feedback mechanisms in the model are quite complex; variations in most parameters will affect the entire atmospheric structure. Many global scale models are intent on getting the large-scale winds and



temperature patterns to agree with previous results but on the smaller, local scale, the way this is achieved may lead to misrepresentation. The effect of gravity waves appears to be the most important variable in the model; therefore, we suggest increasing the gravity wave forcing of the TIME-GCM. A slight increase in dynamic forcing would induce closure of the mesospheric winter jet, reversal of winds in summer, decrease in tidal amplitude during winter, an increased meridional circulation leading to a greater temperature difference near 87 km, a lowering of the mesopause during summer, and a stronger inversion layer near 65–75 km. This increase will show up in the OH emission intensities as the region responds to the increased vertical transport and diffusion. Gravity wave forcing is influenced by many parameters, including Prandtl number, vertical diffusivity  $K_z$ , strength of the mean zonal wind, etc. The appearance of a high summer mesopause and very weak winter inversion suggests these parameters are not quite right. Work in isolating various effects in the model may be needed and tested against observations in order to determine the best combination of all. These differences may also be linked to the influence of planetary waves as reported by others. The fact that the TIME-GCM excludes planetary wave interaction may cause unrealistic gravity wave forcing to occur in the mesosphere.

The asymmetry of fall and spring OH winds was reported by Wickwar *et al.* [1997b]. In order to examine seasonal differences, months were grouped together into "seasons" for which similar characteristics of the OH wind were observed. Different seasonal representations in our observations (e.g., beginning the season at solstice or equinox rather than centering them at these times) may eliminate this asymmetry.

A thorough check of the chemistry in the model would provide useful information on the possible causes of the differences between observations and modeled results. This would not only include O and O<sub>3</sub> but also the major species including N<sub>2</sub> and O<sub>2</sub> to eliminate any adverse influence they may be injecting in the results. This could be extended into the radiative budget of the TIME-GCM to ensure compliance with the latest studies.

Future comparisons should consider the importance of having a complete middle atmosphere profile from one location to stretch from 40 km to well above 100 km, which could be easily achievable with the simultaneous measurements of Rayleigh and sodium resonance lidars. The ability to measure winds derived from a Doppler lidar in order to make comparisons at several altitudes would increase the understanding of

interactions between layers of the middle atmosphere. The ability to obtain absolute intensities from the FPI would help quantify the OH intensity measurements with those calculated from model parameters and published reaction rates.

## CHAPTER 7

## SUMMARY

We have obtained middle atmosphere temperatures above Logan, UT, on over 130 nights over a 2-year period. The Rayleigh-scatter lidar technique was used to measure temperatures from 40–90 km. Thus we have ensured the accuracy of our Rayleigh backscatter lidar technique and have obtained very useful information from our mid-latitude temperature observations. These results have been applied here to study middle atmosphere's thermal structure, with emphasis on the properties and influence of gravity waves, tides, and planetary waves.

Considerable efforts were taken to assess the temperature retrieval method, to identify possible errors in the technique, to make true comparisons with other temperature observations including those at higher latitudes and empirical models, and to effectively validate the results. We have demonstrated the advantage of co-located instrumentation by comparing observations of different fields with a physics-based model. This has allowed many insights into the interdependency of the dynamics and chemistry of the atmosphere. As a result we have a number of conclusions relating to both the instrumentation and to middle atmosphere research. The main results can be summarized as follows.

- 1) A thorough analysis was performed on the temperature measurements themselves before comparing them to other measurements. This included careful inspection of such factors as the integration algorithm, the value of  $g$  and its altitude dependence, the effect of changing atmospheric composition on the Rayleigh backscatter cross section and on the derived temperatures, the evaluation of the background signal level, the evaluation of the ratio of the standard deviation to signal, and the value of that ratio for starting the temperature integration. Several potential systematic errors of between 0.5 and 3 K were identified and eliminated or reduced to a level below 0.1 K. We found it was necessary to use sodium lidar observations to initialize the temperatures at the upper level as these values are more representative of our findings. For an accurate depiction of long-term averages (multiple nights), we considered the effect of adding photocounts together and then deriving the temperatures versus a more conservative approach of deriving temperatures for smaller time intervals and averaging these together.

We have chosen the latter method since it is less sensitive to an unstable background. We have applied a rigorous analytical technique directly to the temperature integral in order to obtain temperature uncertainties rather than to the density measurements.

2) We found good agreement among our temperatures, the French temperatures, and those in the MSIS90 empirical model from examining the summer temperatures between 50 and 70 km at the 1–3 K level. These small differences are best explained by zonal differences in the observation locations or the fact that the French and MSIS used a larger database. To resolve these differences, a much longer lidar data set is needed in order to distinguish long-term temperature trends over Utah.

3) The major feature of winter was the development of a persistent fall-winter inversion in the 65–75 km region and its associated minimum approximately 15 km lower in altitude. There appears to be an interannual variation (based solely on winter 1994 and 1995) that was at first believed to be due to the quasi-biennial oscillation (QBO) [Hagan *et al.*, 1992]. However, a closer examination of the variability within one year shows that temperature structures have lifetimes of the order of a week or ten days. Thus, variations from year to year could arise from variations within a month during one year, and detection depends on the sampling, or observation frequency. This period has been associated with planetary waves but an analysis of the correlation with planetary waves in the troposphere was inconclusive. We suggest further investigations into this area.

4) Differences between our temperatures and the French temperatures during the winter appear as lower temperatures near the stratopause and as higher temperatures in the upper mesosphere. This might be a zonal difference, orographically induced, or it might be a reflection of the large winter variability in that our averages are only over two years instead of six or more years. It might also reflect the occurrence of more stratospheric warmings over Europe than over North America. This variability over Utah during winter is supported by large winter variability in wind observations from BLO at 87 km [Wickwar *et al.*, 1997b]. In addition, the amplitude of the semidiurnal tide was smaller than reported elsewhere. The differences in our summertime (June and July) mesosphere temperatures compared to the French data and the MSIS90 model—that they were lower—may also have a zonal origin. As more data

are collected and averaged, one would be able to determine whether these are truly zonal differences or whether they are a result of a sparse sampling bias in our data. However, 4 years of OH winds have shown a distinct winter difference, thus reinforcing this winter difference in the lidar data.

5) There appears to be a spring-fall asymmetry in the OH wind and intensity data, as well as the temperature profiles. This asymmetry may be due to our definition of the season, e.g., is the season centered on the month of equinox occurrence or does the season begin with this month? There is also a question of whether to use the 15<sup>th</sup> of the month as a center point or the 21<sup>st</sup>. The asymmetry may also result from the fact that the seasonal transitions are quick, and thus allow little time for development of any distinct characteristic of their own.

6) The equinoctial profiles of our mid-latitude temperature profiles and the high-latitude temperature profiles of Lübken and von Zahn [1995] are quite similar but their behavior approaching the equinoxes is different. The summer high-altitude temperatures are much colder than ours and the minimum occurs at a higher altitude, indicating vertical motions that cause these low temperatures occur higher in the high-latitudes. In contrast to strong evidence of dynamical control throughout the mid-latitude middle atmosphere, there is only a hint of a winter temperature inversion. The heating observed near 90 km during October fits more with the explanation of a chemical heat source instead of a dynamical one.

7) Between 80 and 90 km, our temperatures confirm the finding by sodium lidars [Senft *et al.*, 1994; Yu and She, 1995] that the temperatures are not as cold as suggested by the MSIS90 model. The differences can be as large as 20 K. One consequence is that we find that the mid-latitude summer mesopause is at a lower altitude than in the MSIS90 model. Another consequence is that the deduced meridional circulation, which is so important for explaining the upper mesospheric temperatures, would be different from what has been deduced using the MSIS90 model. This problem arose from the lack of good temperature data between 80 and 110 km when the model was developed. That problem can only be solved by a combination of resonance-scatter lidars and the next generation of more powerful Rayleigh-scatter lidars.

8) In addition to the above differences between our temperatures and the MSISE90 temperatures, we also found possible instrumental differences with the SME temperatures and those from the sodium lidars. In the summer comparisons between 50 and 70 km, the SME temperatures were hotter than the others by 6–8 K. Because the slope of the mesospheric temperature profiles were very similar to the others, we consider the discrepancy might arise from a small altitude error in the measurements. Hence relative measurements may still be good. In comparing techniques, we found larger annual variations in the upper mesosphere near 85 km, from Rayleigh lidars and SME than from sodium lidars. This may be an instrumental difference as the Rayleigh lidars are operating at the top of their altitude range in this region, and the sodium lidars are operating at the bottom of theirs. On the Rayleigh side, several groups [Keckhut *et al.*, 1993; Singh *et al.*, 1996], including ours, have discussed the importance of the stability of the PMT background level. On the resonance side, it would seem that one is asking too much to obtain good temperatures from just two points on a spectrum under noisy conditions. These points could be investigated with co-located Rayleigh and resonance lidars by making simultaneous observations and by using the next generation Rayleigh lidar with its much improved signal such that 85 km is no longer as close to the top of the altitude range.

9) The final objective of this dissertation was to compare seasonal averages from multiple observations using co-located instruments with a physics-based global circulation model, namely the TIME-GCM of Roble and Ridley [1994]. This model includes radiative, dynamical (gravity wave and tidal perturbations), and chemical processes to calculate temperature, circulation, and compositional structure. Various discrepancies have been addressed, including mesospheric temperature differences, the lack of a winter inversion in the model, and a summer mesopause that appears too high. The seasonal winds of USU at 87 km show the largest disagreement during winter and the closest similarity during fall. The model has a significant tidal amplitude in winter whereas we do not. The difference with the model is the lack of semidiurnal winter tide and small semidiurnal spring equinox tide. OH intensities show significant phase differences between model and observations throughout the year except spring, again an indication of the equinoctial asymmetry over Utah. The model consistently has increasing intensities near

the end of the night that are not observed in the FPI data. The model indicates a height of 92 km for the peak of the OH layer whereas observations have shown that it is rather stable near 87 km. The interesting aspect of this is that when model winds are calculated at 92 km, they are more similar to observations. Thus when we calculate winds at the same level at which the OH is calculated, the model matches the observations more closely.

Discrepancies have been attributed to lack of adequate chemistry in the TIME-GCM and insufficient gravity wave parameterization. The results at USU also suggest there are longitudinal differences on a small temporal scale but that these can be quite large from year to year and place to place. Causes include topographically induced gravity waves and planetary wave activity. The possibility of zonal differences should be pursued by making careful comparisons with the Purple Crow lidar, which is at the same latitude as the USU lidar, but far removed from the Rockies and any other significant mountain chain.

An increase in the gravity wave forcing is considered to be the most significant change that would produce calculated fields from the model similar to observations from the USU lidar and the BLO FPI. This would allow closure of the winter jet, reversal of the summer jet, creation of the winter inversion layer, lowering of the summer mesopause, and a larger temperature variation at 87 km. The parameterization of gravity waves has been useful but models must still rely on empirical data until further studies and observations will allow a complete understanding of the physics behind the workings. The first step in furthering our knowledge about this region is by making good reliable simultaneous observations of physical parameters that will offer insight into the appearance of the atmosphere. This includes not only measuring multiple fields at one particular height but also measuring over as wide a range of altitudes as possible. This can be done with a wind capability added to the lidar system. These observations can then be used for improving transport, chemical species distributions, and temperature variations in global-scale circulation models.

## REFERENCES

- Adriani, A., G.P. Gobbi, F. Congeduti, and G. Di Donfrancesco, Lidar observations of stratospheric and mesospheric temperature: November 1988–November 1989, *Ann. Geophysicae*, 9, 252–258, 1991.
- Aikin, A.C., M.L. Chanin, J. Nash, and D.J. Kendig, Temperature trends in the lower mesosphere, *Geophys. Res. Lett.*, 18, 416–419, 1991.
- Allen, M., J.I. Lunine, and Y.L. Yung, The vertical distribution of ozone in the mesosphere and lower thermosphere, *J. Geophys. Res.*, 89, 4841–4872, 1984.
- Andrews, D.G., J.R. Holton, and C.B. Leovy, *Middle Atmosphere Dynamics*, 489 pp., Academic Press, Inc., New York, 1987.
- Avery, S.K., The meteor radar as a tool for upper atmosphere research, *Adv. Space Res.*, 10, 193–200, 1990.
- Bacmeister, J.T., Mountain-wave drag in the stratosphere and mesosphere inferred from observed winds and a simple mountain-wave parameterization scheme, *J. Atmos. Sci.*, 46, 377–399, 1993.
- Baker D.J., and A.T. Stair, Jr., Rocket measurements of the altitude distributions of the hydroxyl airglow, *Physica Scripta*, 37, 611–622, 1988.
- Balsley, B.B., W.L. Ecklund, and D.C. Fritts, VHF echoes from the high latitude mesosphere and lower thermosphere: Observations and interpretations, *J. Atmos. Sci.*, 40, 2451–2466, 1983.
- Barnett, J.J., and M. Corney, Middle atmosphere reference model derived from satellite data, in *MAP Handbook 16*, edited by K. Labitzke, J.J. Barnett, and B. Edwards, pp. 47–85, SCOSTEP, Urbana, Ill., 1985a.
- Barnett, J.J., and M. Corney, Temperature data from satellites, in *MAP Handbook 16*, edited by K. Labitzke, J.J. Barnett, and B. Edwards, pp. 3–11, SCOSTEP, Urbana, Ill., 1985b.
- Bates, D.R., and Nicolet, M., The photochemistry of the atmospheric water vapor, *J. Geophys. Res.*, 55, 301–322, 1950.
- Beer, T., *Atmospheric Waves*, 297 pp., John Wiley & Sons, New York, 1974.
- Bills, R.E., C.S. Gardner, and C.Y. She, Narrowband lidar technique for sodium temperature and doppler wind observations of the upper atmosphere, *Opt. Eng.*, 30, 13–21, 1991.
- Booker, J.R., and F.P. Bretherton, The critical layer for internal gravity waves in a shear flow, *J. Fluid Mech.*, 27, 513–539, 1967.
- Brasseur, G., and S. Solomon, *Aeronomy of the Middle Atmosphere*, 441 pp., D. Reidel Publishing Company, Dordrecht, Holland, 1984.
- Bretherton, F.P., The propagation of groups of internal gravity waves in a shear flow, *Quart. J. Roy. Meteor. Soc.*, 92, 446–480, 1966.
- Bretherton, F.P., Momentum transport by gravity waves, *Quart. J. Roy. Meteor. Soc.*, 95, 213–243, 1969.
- Chalamala, B.R., and R.A. Copeland, Collision dynamics of OH ( $X^2\Pi_{1/2}$ ), *J. Chem. Phys.*, 99, 5807–5811, 1993.



- Chanin, M.L., A. Garnier, A. Hauchecorne, and J. Porteneuve, A Doppler lidar for measuring winds in the middle atmosphere, *Geophys. Res. Lett.*, **16**, 1273-1276, 1989a.
- Chanin, M.L., and A. Hauchecorne, Lidar observation of gravity and tidal waves in the stratosphere and mesosphere, *J. Geophys. Res.*, **86**, 9715-9721, 1981.
- Chanin, M.L., A. Hauchecorne, A. Garnier, and D. Nedeljkovic, Recent lidar developments to monitor stratosphere-troposphere exchange, *J. Atm. Terr. Phys.*, **56**, 1073-1081, 1994.
- Chanin, M.L., A. Hauchecorne, and N. Smires, Contribution to the CIRA model from Ground-based lidar, in *MAP Handbook 16*, edited by K. Labitzke, J.J. Barnett, and B. Edwards, pp. 305-314, SCOSTEP, Urbana, Ill., 1985.
- Chanin, M.L., A. Hauchecorne, and N. Smires, Contribution to the new reference atmosphere from ground-based lidar, *Adv. Space Res.*, **10**, 211-216, 1990.
- Chanin, M.L., P. Keckhut, A. Hauchecorne, and K. Labitzke, The solar activity—Q.B.O. effect in the lower thermosphere, *Ann. Geophys.*, **7**, 463-470, 1989b.
- Chanin, M.L., N. Smires, and A. Hauchecorne, Long-term variation of the temperature of the middle atmosphere at mid latitude: Dynamical and radiative causes, *J. Geophys. Res.*, **92**, 10933-10941, 1987.
- Chapman, S., and R.S. Lindzen, *Atmospheric Tides*, 200 pp., D. Reidel Publishing Company, Dordrecht, Holland, 1970.
- Charney, J.G., and P.G. Drazin, Propagation of planetary-scale disturbances from the lower to the upper atmosphere, *J. Geophys. Res.*, **66**, 83-90, 1961.
- CIRA 1972, *COSPAR International Reference Atmosphere 1972*, Akedemie-Verlag, Berlin, 1972 (Committee for COSPAR International Reference Atmosphere (CIRA) of COSPAR Working Group 4.)
- Clancy, R.T., and D.W. Rusch, Climatology and trends of mesospheric (58-90 km) temperatures based upon 1982-1986 SME limb scattering profiles, *J. Geophys. Res.*, **94**, 3377-3393, 1989.
- Clancy, R.T., D.W. Rusch, and M.T. Callan, Temperature minima in the average thermal structure of the middle mesosphere (70-80 km) from analysis of 40 to 92 km SME global temperature profiles, *J. Geophys. Res.*, **99**, 19,0001-19,020, 1994.
- Clemesha, B.R., H. Takahashhi, P.P. Bastista, Y. Sahai, and D.M. Simonich, The temperature dependence of airglow emissions from the upper mesosphere and lower thermosphere, *Planet. Space Sci.*, **39**, 1397-1404, 1991.
- Cogger, L.L., R.D. Elphinstone, and J.S. Murphree, Temporal and latitudinal 5577 Å airglow variations, *Can. J. Phys.*, **59**, 1296-1307, 1981.
- Coxon, J.A., and S.C. Foster, Rotational analysis of hydroxyl vibration-rotation bands: Molecular constants for OH X<sup>2</sup>Π, 6 ≤ v ≤ 10, *Can. J. Phys.*, **60**, 41-45, 1982.
- DeMore, W.B., J.J. Margitan, M.J. Molina, R.T. Watson, D.H. Golden, R.F. Hampson, M.J. Kurylo, C.J. Howard, and A.R. Ravishankara, Chemical kinetics and photochemical data for use in stratospheric modeling, *Evaluation No. 7, JPL, Pub 85-37*, 217 pp., Jet Propulsion Lab, Pasadena, Calif., 1985.

- Dewan, E.M., and R.E. Good, Saturation in the universal spectrum for vertical profile of horizontal scalar winds in the atmosphere, *J. Geophys. Res.*, **91**, 7242-7248, 1986.
- Dodd, J.A., S.J. Lipson, and W.A.M. Blumberg, Vibrational relaxation of  $\text{OH}(X^2\pi_{v=1,3})$  by  $\text{O}_2$ , *J. Chem. Phys.*, **92**, 3387-3393, 1990.
- Dodd, J.A., S.J. Lipson, and W.A.M. Blumberg, Formation and vibrational relaxation of  $\text{OH}(X^2\pi_{v=1})$  by  $\text{O}_2$  and  $\text{CO}_2$ , *J. Chem. Phys.*, **95**, 5752-5762, 1991.
- Dudhia, A., S.E. Smith, A.R. Wood, and F.W. Taylor, Diurnal and semi-diurnal temperature variability of the middle atmosphere, as observed by ISAMS, *Geophys. Res. Lett.*, **20**, 1251-1254, 1993.
- Dunkerton, T.J., Theory of internal gravity wave saturation, *Pageoph.*, **130**, 373-397, 1989.
- Ferrare, R.A., T.J. McGee, D. Whiteman, J. Burris, M. Owens, J. Butler, R.A. Barnes, F. Schmidlin, W. Komhyr, P.H. Wang, M.P. McCormick, and A.J. Miller, Lidar measurements of stratospheric temperature during STOIC, *J. Geophys. Res.*, **100**, 9303-9312, 1995.
- Finlayson-Pitts, B.J., and T.E. Kleindienst, The reaction of hydrogen atoms with ozone as a source of vibrationally excited hydroxyl radicals:  $\text{OH}(X^2\pi_v=2)$  for kinetic studies, *J. Chem. Phys.*, **74**, 5643-5655, 1981.
- Fleming, E.L., S. Chandra, J.J. Barnett, and M. Corney, Zonal mean temperature pressure, zonal wind and geopotential height as functions of latitude, *Adv. Space Res.*, **10**, 11-59, 1990.
- Forbes, J.M., Middle atmosphere tides, *J. Atmos. Terr. Phys.*, **46**, 1049-1067, 1984.
- Forbes, J.M., Atmospheric tides between 80 km and 120 km, *Adv. Space Res.*, **10**, 127-140, 1990.
- Forbes, J.M., M.E. Hagan, S. Miyahara, F. Vail, A.H. Manson, C.E. Meek, and Y.I. Portnyagin, Quasi 16-day oscillation in the mesosphere and lower thermosphere, *J. Geophys. Res.*, **100**, 9149-9163, 1995.
- Forbes, J.M., and F. Vial, Monthly simulations of the solar semidiurnal tide in the mesosphere and lower thermosphere, *J. Atmos. Terr. Phys.*, **51**, 649-661, 1989.
- Fricke, K.H., and U. von Zahn, Mesopause temperatures derived from probing the hyperfine structure of the D2 resonance line of sodium by lidar, *J. Atmos. Terr. Phys.*, **47**, 499-512, 1985.
- Fritts, D.C., Gravity wave saturation in the middle atmosphere: A review of theory and observations, *Rev. Geophys. Space Phys.*, **22**, 275-308, 1984.
- Fritts, D.C., A review of gravity wave saturation processes, effects, and variability in the middle atmosphere, *Pageoph.*, **130**, 343-371, 1989.
- Fritts, D.C., and W. Lu, Spectral estimates of gravity wave energy and momentum fluxes. Part II: Parameterization of wave forcing and variability, *J. Atmos. Sci.*, **50**, 3695, 1993.
- Fritts, D.C., and G.D. Nastrom, Sources of mesoscale variability of gravity waves. Part II: Frontal, convective, and jet stream excitation, *J. Atmos. Sci.*, **49**, 111-127, 1992.
- Fritts, D.C., and R.A. Vincent, Mesospheric momentum flux studies at Adelaide, Australia: Observations and a gravity wave-tidal interaction model, *J. Atmos. Sci.*, **44**, 605-619, 1987.

- Gao, X., J.W. Meriwether, V.B. Wickwar, and T.D. Wilkerson, Rayleigh lidar measurements of the temporal and vertical wavenumber spectra in the mesosphere height over the Rocky Mountain region, submitted, *J. Geophys. Res.*, 1997.
- Garcia, R.R., On the mean meridional circulation of the middle atmosphere, *J. Atmos. Sci.*, **44**, 3599-3609, 1987.
- Garcia, R.R., and S. Solomon, A numerical model of the zonally averaged dynamical and chemical structure of the middle atmosphere, *J. Geophys. Res.*, **88**, 1379-1400, 1983.
- Garcia, R.R., and S. Solomon, The effect of breaking gravity waves on the dynamics and chemical composition of the mesosphere and lower thermosphere, *J. Geophys. Res.*, **90**, 3850-3868, 1985.
- Garcia, R.R., F. Stordal, S. Solomon, and J.T. Kiehl, A new numerical model of the middle atmosphere 1. Dynamics and transport of tropospheric source gases, *J. Geophys. Res.*, **97**, 12,967-12,991, 1992.
- Gardner, C.S., Sodium resonance fluorescence lidar applications in atmospheric science and astronomy, *Proc. IEEE*, **77**, 408-418, 1989.
- Gardner, C.S., Diffusive filtering theory of gravity wave spectra in the atmosphere, *J. Geophys. Res.*, **99**, 20,601-20,622, 1994.
- Gardner, C.S., D.C. Senft, T.J. Beatty, R.E. Bills, and C.A. Hostettler, Rayleigh and sodium lidar techniques for measuring middle atmosphere density, temperature, and wind perturbations and their spectra, *World Ionosphere/Thermosphere Study Handbook 2*, 148-187, 1989.
- Geller, M.A., Dynamics of the middle atmosphere, *Space Sci. Rev.*, **34**, 359-375, 1983.
- Gille, S.T., A. Hauchecorne, and M.L. Chanin, Semidiurnal and diurnal tidal effects in the middle atmosphere as seen by Rayleigh lidar, *J. Geophys. Res.*, **96**, 7579-7587, 1991.
- Groves, G.V., and F.M. Forbes, Equinox tidal heating of the upper atmosphere, *Planet. Space Sci.*, **32**, 447-552, 1984.
- Hagan, M.E., J.M. Forbes, and F. Vail, On modeling migrating solar tides, *Geophys. Res. Lett.*, **22**, 893-896, 1995.
- Hagan, M.E., F. Vail, and J.M. Forbes, Variability in the upward propagating semidiurnal tide due to effects of QBO in the lower atmosphere, *J. Atmos. Terr. Phys.*, **54**, 1465-1474, 1992.
- Halliday, D. and R. Resnick, *Physics*, 827pp., John Wiley & Sons, Inc., New York, 1960.
- Hauchecorne, A., and M. L. Chanin, Density and temperature profiles obtained by lidar between 35 and 70 km, *Geophys. Res. Lett.*, **7**, 565-568, 1980.
- Hauchecorne, A., and M.L. Chanin, A mid-latitude ground-based lidar study of stratospheric warmings and planetary wave propagation, *J. Atmos. Terr. Phys.*, **44**, 557-583, 1982.
- Hauchecorne, A., and M.L. Chanin, Mid-latitude lidar observations of planetary waves in the middle atmosphere during the winter of 1981-1982, *J. Geophys. Res.*, **88**, 3843-3849, 1983.
- Hauchecorne, A., M.L. Chanin, and P. Keckhut, Climatology and trends of the middle atmospheric temperature (33-87 km) as seen by the Rayleigh lidar over the south of France, *J. Geophys. Res.*, **96**, 15,297-15,309, 1991.

- Hauchecorne, A., M.L. Chanin, and R. Wilson, Mesospheric temperature inversion and gravity wave breaking, *Geophys. Res. Lett.*, **14**, 933-936, 1987.
- Hauchecorne, A., and A. Maillard, A 2-D dynamical model of mesospheric temperature inversions in winter, *Geophys. Res. Lett.*, **17**, 2197-2200, 1990.
- Hedin, A.E., Extension of the MSIS thermospheric model into the middle and lower atmosphere, *J. Geophys. Res.*, **96**, 1159-1172, 1991.
- Hedin, A.E., N.W. Spencer, and T.L. Killeen, Empirical global model of upper thermosphere winds based on atmosphere and dynamics explorer satellite data, *J. Geophys. Res.*, **93**, 9959-9978, 1988.
- Hilsenrath, E., and B.M. Schlesinger, Annual variation of the ozone layer above mid-latitudes, *J. Geophys. Res.*, **45**, 3089-3096, 1981.
- Hines, C.O., Internal atmospheric gravity waves at ionospheric heights, *Can. J. Phys.*, **38**, 1441-1481, 1960.
- Hines, C.O., The saturation of gravity waves in the middle atmosphere. Part II: Development of doppler-spread theory, *J. Atmos. Sci.*, **48**, 1360-1379, 1991.
- Hodges, R.R., Generation of turbulence in the upper atmosphere by internal gravity waves, *J. Geophys. Res.*, **72**, 3455-3458, 1967.
- Hodges, R.R., Eddy diffusion coefficients due to instabilities in internal gravity waves, *J. Geophys. Res.*, **74**, 4087-4090, 1969.
- Holton, J.R., *An Introduction to Dynamic Meteorology*, 319 pp., Academic Press, Inc., New York, 1979.
- Holton, J.R., The role of gravity wave induced drag and diffusion in the momentum budget of the mesosphere, *J. Atmos. Sci.*, **39**, 791-799, 1982.
- Holton, J.R., The influence of gravity wave breaking on the general circulation of the middle atmosphere, *J. Atmos. Sci.*, **40**, 2497-2507, 1983.
- Holton, J.R., The generation of mesospheric planetary waves by zonally asymmetric gravity wave breaking, *J. Atmos. Sci.*, **41**, 3427-3430, 1984.
- Holton, J.R., and Lindzen, R.S., Updated theory for the quasi-biennial cycle for the tropical stratosphere, *J. Atmos. Sci.*, **29**, 1076-1080, 1972.
- Holton, J.R., and W.M. Wehrbein, A numerical model of the zonal mean circulation of the middle atmosphere, *Pageoph.*, **118**, 284-306, 1980.
- Houghton, J.R., The stratosphere and mesosphere, *Quart. J. Roy. Meteor. Soc.*, **104**, 1-29, 1978.
- Howell, C.D., D.V. Midhelangeli, M. Allen, and Y.L. Yung, SME observations of O<sub>2</sub> (1Δg) nightglow: An assessment of the chemical production mechanisms, *Planet. Space Sci.*, **38**, 529-537, 1990.
- Hoxit, L.E., and R.M. Henry, Diurnal and annual temperature variation in the 30-60 km region as indicated by statistical analysis of rocketsonde temperature data, *J. Atmos. Sci.*, **30**, 922-933, 1973.
- Huang, T.Y.W., and A.K. Smith, Dynamic and chemical feedback in a two-dimensional interactive model of the middle atmosphere, *J. Geophys. Res.*, **100**, 11,085-11,104, 1995.

- Jenkins, D.B., D.P. Wareing, L. Thomas, and G. Vaughan, Upper stratospheric and mesospheric temperatures derived from lidar observations at Aberystwyth, *J. Atmos. Terr. Phys.*, **49**, 287-298, 1987.
- Johnston, J.E., and A.L. Broadfoot, Mid-latitude observations of the night airglow: Implications to quenching near the mesopause, *J. Geophys. Res.*, **98**, 21,593-21,603, 1993.
- Jones, W.L., and D.D. Houghton, The coupling of momentum between internal gravity waves and mean flow: A numerical study, *J. Atmos. Sci.*, **28**, 604-608, 1971.
- Kaye, J.A., On the possible role of the  $O+HO_2 \rightarrow OH+O_2$  reaction in the OH airglow, *J. Geophys. Res.*, **93**, 285-288, 1988.
- Keckhut, P., and M.L. Chanin, Seasonal variation of the 11 year solar effect on the middle atmosphere: Role of the QBO, in *MAP Handbook 16*, edited by K. Labitzke, J.J. Barnett, and B. Edwards, pp. 33-38, SCOSTEP, Urbana, Ill., 1985.
- Keckhut, P., and M.L. Chanin, Middle atmosphere response to the 27-day solar rotation as observed by lidar, *Geophys. Res. Lett.*, **19**, 809-812, 1992.
- Keckhut, P., M.L. Chanin, and A. Hauchecorne, Stratosphere temperature measurement using Raman lidar, *Appl. Opt.*, **29**, 582-586, 1990.
- Keckhut, P., M.E. Gelman, J.D. Wild, F. Tissot, A.J. Miller, A. Hauchecorne, M.L. Chanin, E.F. Fishbein, J. Gille, J.M. Russell, III, and F.W. Taylor, Semidiurnal and diurnal temperature tides (30-55 km): Climatology and effect on UARS-LIDAR data comparisons, *J. Geophys. Res.*, **101**, 10299-10320, 1996.
- Keckhut, P., A. Hauchecorne, and M.L. Chanin, A critical review of the database acquired for the long-term surveillance of the middle atmosphere by the French Rayleigh lidars, *J. Atmos. and Oceanic Tech.*, **10**, 850-867, 1993.
- Keckhut, P., A. Hauchecorne, and M.L. Chanin, Midlatitude long-term variability of the middle atmosphere: Trends and cyclic and episodic changes, *J. Geophys. Res.*, **100**, 18887-18897, 1995.
- Knutsen, K., and R.A. Copeland, Vibrational relaxation of OH ( $X^2\pi_{1/2}, v=7,8$ ) by  $O_2$ ,  $N_2$ ,  $N_2O$  and  $CO_2$ , (abstract), *Eos, Trans. A.G.U.*, (34) Fall Meeting Suppl., 472, 1993.
- Leovy, C.B., Simple models of thermally driven mesospheric circulations, *J. Atmos. Sci.*, **21**, 327-341, 1964.
- Le Texier H., S. Solomon, and R.R. Garcia, Seasonal variability of the OH Meinel bands, *Planet. Space Sci.*, **35**, 977-989, 1987.
- Lindzen, R.S., Thermally driven diurnal tide in the atmosphere, *Quart. J. R. Meteorol. Soc.*, **93**, 18-42, 1967.
- Lindzen, R.S., Lower atmospheric energy sources for the upper atmosphere, *Meteorol. Monogr.*, **9**, 37-41, 1968.
- Lindzen, R.S., Turbulence and stress due to gravity wave and tidal breakdown, *J. Geophys. Res.*, **86**, 9709-9714, 1981.
- Lindzen, R.S., *Dynamics in Atmospheric Physics*, 310 pp., Cambridge University Press, Cambridge, U.K., 1990.

- Lindzen, R.S., and J.R. Holton, A theory of the quasi-biennial oscillation, *J. Atmos. Sci.*, 25, 1095-1104, 1968.
- Llewellyn, E.J., and B.H. Long, The OH Meinel Bands in the airglow—the radiative lifetime, *Can. J. Phys.*, 56, 581-598, 1978.
- Llewellyn, E.J., B.H. Long, and B.H. Solheim, The quenching of OH\* in the atmosphere, *Planet. Space Sci.*, 26, 525-531, 1987.
- Lowe, R.P., L.M. LeBlanc, and K.L. Gilbert, WINDII/UARS observation of twilight behavior of the hydroxyl airglow at mid-latitude equinox, *J. Atmos. Terr. Phys.*, 58, 1863-1869, 1996.
- Lopez-Moreno, J.J., R. Rodrigo, F. Moreno, M. Lopez-Puertas, and A. Molina, Altitude distribution of vibrationally excited states of atmospheric hydroxyl at levels  $v=2$  to  $v=7$ , *Planet. Space Sci.*, 35, 135-139, 1987.
- Lübken, F.J., and U. von Zahn, Thermal structure of the mesopause region at polar latitudes, *J. Geophys. Res.*, 96, 20841-20857, 1991.
- Lübken, F.J., W. Hillert, G. Lahmacher, U. von Zahn, M. Bittner, D. Offermann, F.J. Schmidlin, A. Hauchecorne, M. Mourier, and P. Czechowsky, Intercomparison of density and temperature profiles obtained by lidar, ionization gauges, falling spheres, datasondes and radiosondes during the DYANA campaign, *J. Atmos. Terr. Phys.*, 56, 1969-1984, 1994.
- Madden R.A., and K. Labitzke, A free Rossby wave in the troposphere and stratosphere during January 1979, *J. Geophys. Res.*, 86, 1247-1254, 1981.
- Makhlouf, U.B., R.H. Picard, and J.R. Winick, Photochemical-dynamical modeling of the measured response of airglow to gravity waves, 1. Basic model for OH airglow, *J. Geophys. Res.*, 100, 11,289-11,311, 1995.
- Manson, A.H., and C.E. Meek, Gravity wave propagation characteristics (60-120 km) as determined by the Saskatoon MF radar (Gravnet) system: 1983-85 at 52°N, 107°W, *J. Atmos. Sci.*, 45, 932-946, 1988.
- Manson, A.H., J.B. Gregory, and D.G. Stephenson, Winds and wave motions to 110 km at mid-latitudes, I, Partial reflection radiowave soundings, 1972-1973, *J. Atmos. Sci.*, 31, 2207-2211, 1974.
- Manson, A.H., C.E. Meek, H. Teitelbaum, F. Vial, R. Schminder, D. Kurschner, M.J. Smith, G.J. Fraser, and R.R. Clark, Climatologies of semi-diurnal and diurnal tides in the middle atmosphere (70-110 km) at middle latitudes (40-55), *J. Atmos. Terr. Phys.*, 51, 579-593, 1989.
- Matsuno, T., A quasi one-dimensional model of the middle atmosphere circulation interacting with internal gravity waves., *J. Meteor. Soc. Japan*, 60, 215-226, 1982.
- McDade, I.C., and E.J. Llewellyn, Kinetic parameters related to sources and sinks of vibrationally excited OH in the nightglow, *J. Geophys. Res.*, 92, 7643-7650, 1987.
- McDade, I.C., E.J. Llewellyn, D.P. Murtagh, and R.G.H. Greer, Eton 5: Simultaneous rocket measurements of OH Meinel  $\Delta v=2$  sequence and (8,3) band emission profiles in the nightglow, *Planet. Space Sci.*, 35, 1137-1147, 1987.
- McLondres, C., and N.A. McFarlane, Interactions between orographic gravity wave drag and forced stationary planetary waves in the winter northern hemisphere middle atmosphere, *J. Atmos. Sci.*, 50, 1966-1990, 1993.

- Measures, R.M., Fundamentals of laser remote sensing, in *Laser Remote Chemical Analysis*, edited by R. M. Measures, pp. 1-84, Wiley, New York, 1988.
- Meek, C.E., I.M. Reid, and A.H. Manson, Observations of mesospheric wind velocities. Part I: Gravity wave horizontal scales and phase velocities from spaced wind observations, *Radio Sci.*, **20**, 1368-1382, 1985.
- Meinel, A.B., OH emission bands in the spectrum of the night sky, *J. Astrophys. J.*, **111**, 555-559, 1950.
- Meriwether, J.W., A review of the photochemistry of selected nightglow emissions from the mesopause, *J. Geophys. Res.*, **94**, 14,629-14,646, 1989.
- Meriwether, J.W., and M.G. Mlynczak, Is chemical heating a major cause of the mesosphere inversion layer?, *J. Geophys. Res.*, **100**, 1379-1387, 1995.
- Meriwether, J.W., P.D. Dao, R.T. McNutt, W. Klemetti, W. Moskowicz, and G. Davidson, Rayleigh lidar observations of mesosphere temperature structure, *J. Geophys. Res.*, **99**, 16,973-16,987, 1994.
- Mies, A.B., Calculated vibrational transition probabilities of OH ( $X^2\Pi$ ), *J. Mol. Spectrosc.*, **53**, 150-188, 1974.
- Mitchell, N.J., L. Thomas, and A.K.P. Marsh, Lidar observations of long-period gravity waves in the stratosphere, *Ann. Geophysicae*, **9**, 588-596, 1991.
- Miyahara, S., and J.M. Forbes, Theory and modeling tide/gravity wave/mean-flow interactions in the mesosphere and lower thermosphere, *Adv. Space Res.*, **12**, 7-16, 1992.
- Mlynczak, M.G., and S. Solomon, A detailed evaluation of the heating efficiency in the middle atmosphere, *J. Geophys. Res.*, **98**, 10,517-10,541, 1993.
- Monson, I.K., The Fabry-Perot interferometer at Bear Lake Observatory—Improvements to the data reduction and applications to OH and O(1D) measurements, M.S. thesis, Utah State Univ., Logan, 1997.
- Murgatroyd, R.J., The structure and dynamics of the stratosphere, in *The Global Circulation Of The Atmosphere*, edited by G.A. Corby, pp. 159-184, Royal Meteorological Society, London, 1969.
- Murphy, R.E., Infrared emission of OH in the fundamental and first overtone bands, *J. Chem. Phys.*, **54**, 4852-4859, 1971.
- Nastrum, G.D., and D.C. Fritts, Sources of mesoscale variability of gravity waves. Part I: Topographic excitation, *J. Atmos. Sci.*, **49**, 101-110, 1992.
- Nedeljkovic, D., A. Hauchecorne, and M.L. Chanin, Rotational Raman lidar to measure the atmospheric temperature from the ground to 30 km, *IEEE Trans. Geosci. Remote Sens.*, **31**, 90-101, 1993.
- Niciejewski, R.J., and T.L. Killeen, Nocturnal observations of the semidiurnal tide at a midlatitude site, *J. Geophys. Res.*, **100**, 25855-25866, 1995.
- Offermann, D., P. Curtis, J.M. Cisneros, H. Lauche, K. Petzoldt, G. Rose, and J. Satrustegui, Atmospheric temperature structure during the Western European Winter Anomaly Campaign 1975/76, *Atmos. Terr. Phys.*, **41**, 1051-1062, 1979.
- Ohoyama, H., T. Kasai, Y. Yoshimura, H. Kimura, and K. Kuwata, Initial distribution of vibration of the OH radicals produced in the  $H+O_3 \rightarrow OH(X^2\Pi)+O_2$  reaction, *Chem. Phys. Lett.*, **118**, 263-271, 1985.

- Philbrick, C.R., and B. Chen, Transmission of gravity waves and planetary waves in the middle atmosphere based on lidar and rocket measurements, *Adv. Space Res.*, **12**, 303-306, 1992.
- Philbrick, C.R., F.J. Schmidlin, K.U. Grossmann, G. Lange, D. Offermann, K.D. Baker, D. Krankowsky, and U. von Zahn, Density and temperature structure over northern Europe, *J. Atmos. Terr. Phys.*, **47**, 159-172, 1985.
- Portmann, R.W., G.E. Thomas, S. Solomon, and R.R. Garcia, The importance of dynamical feedbacks on doubled CO<sub>2</sub>-induced changes in the thermal structure of the mesosphere, *Geophys. Res. Lett.*, **22**, 1733-1736, 1995.
- Reed, R.J., W.J. Campbell, L.A. Rasmussen, and D.G. Rogers, Evidence of downward-propagating annual wind reversal in the equatorial stratosphere, *J. Geophys. Res.*, **66**, 813-818, 1961.
- Rees, D., I. McEhtrier, A. Anuliah, and S. Batten, Upper atmospheric wind and temperature measurements using imaging Fabry-Perot interferometers, in *WITS Handbook*, edited by C.H. Liu, pp. 188-223, Urbana, Ill., 1989.
- Rees, D., R.W. Smith, F. Signernes, K. Henriksen, and M. Harries, Observations of thermospheric wind patterns in the vicinity of the polar cusp from a Doppler imaging system, *Adv. Space Res.*, in press, 1997.
- Reid, I.M., and R.A. Vincent, Measurements of the horizontal scales and phase velocities of short period mesospheric gravity waves at Adelaide, Australia, *J. Atmos. Terr. Phys.*, **49**, 1033-1048, 1987.
- Roble, R.G., Energetics of the mesosphere and thermosphere, the upper mesosphere and lower thermosphere: A review of experiment and theory, *AGU Monograph*, 1-21, 1995.
- Roble, R.G., and E.C. Ridley, A thermosphere-ionosphere-mesosphere-electrodynamics general circulation model (TIME-GCM): Equinox solar cycle minimum simulations (30-500 km), *Geophys. Res. Lett.*, **21**, 417-420, 1994.
- Rodrigo, R., M.J. Lopez-Gonzalez, and J.J. Lopez-Moreno, Variability of the neutral mesospheric and lower thermospheric composition in the diurnal cycle, *Planet. Space Sci.*, **39**, 803-820, 1991.
- Rodrigo, R., J.J. Lopez-Moreno, M. Lopez-Puertas, F. Moreno, and A. Molina, Neutral atmospheric composition between 60 and 220 km: A theoretical model for mid-latitudes, *Planet. Space Sci.*, **37**, 723-743, 1986.
- Salby, M.L., Survey of planetary-scale traveling waves: The state of theory and observations, *Rev. Geophys. Space Phys.*, **22**, 209-236, 1984.
- Schmidlin, F.J., Temperature inversions near 75 km, *Geophys. Res. Lett.*, **3**, 173-176, 1976.
- Schoeberl, M.R., and D.F. Strobel, The zonally averaged circulation of the middle atmosphere, *J. Atmos. Sci.*, **35**, 577-591, 1978.
- Schoeberl, M.R., D.F. Strobel, and J. P. Apruzese, A numerical model of gravity wave breaking and stress in the mesosphere, *J. Geophys. Res.*, **88**, 5249-5256, 1983.
- Sears, R.D., T.D. Wilkerson, V.B. Wickwar, J.M. Maloney, and S.C. Collins, Multi-dimensional power spectral analysis of structure in the stratosphere and mesosphere observed by Rayleigh Scatter lidar, in *Advances in Atmospheric Remote Sensing with Lidar*, edited by A. Ansmann, R. Neuber, P. Rairoux, and U. Wandinger, pp. 561-564, Springer-Verlag, Berlin, Germany, 1997.



- Senft, D.C., G.C. Papen, C.S. Gardner, J.R. Yu, D.A. Krueger, and C.Y. She, Seasonal variations of the thermal structure of the mesopause region at Urbana, IL (40°N, 88°W) and Ft. Collins, CO (41°N, 105°W), *J. Geophys. Res.*, **21**, 821–824, 1994.
- She, C.Y., J.R. Yu, and H. Chen, Observed thermal structure of a mid-latitude mesopause, *Geophys. Res. Lett.*, **20**, 567–570, 1993.
- She, C.Y., J.R. Yu, D.A. Krueger, R. Roble, P. Keckhut, A. Hauchecorne, and M.L. Chanin, Vertical structure of the midlatitude temperature from stratosphere to mesosphere (30–105), *Geophys. Res. Lett.*, **22**, 377–380, 1995.
- Shibata, T., T. Fukuda, and M. Maeda, Density fluctuations in the middle atmosphere over Fukuoka observed by an XeF lidar, *Geophys. Res. Lett.*, **13**, 1121–1124, 1986.
- Singh, U.N., P. Keckhut, T.J. McGee, M.R. Gross, A. Hauchecorne, E.F. Fishbein, J.W. Waters, J.C. Gille, A.E. Roche, and J.M. Russell III, Stratospheric temperature measurements by two collocated NDSC lidars during UARS validation campaign, *J. Geophys. Res.*, **101**, 10287–10297, 1996.
- Smith, A.K., Longitudinal variations in mesospheric winds: Evidence for gravity wave filtering by planetary waves, *J. Atmos. Sci.*, **53**, 1156–1173, 1996.
- Streit, G.E., and H.S. Johnston, Reactions of vibrationally excited OH radical, *J. Chem. Phys.*, **64**, 95–103, 1976.
- Stroud, W.G., W. Nordberg, W.R. Bandeen, F.L. Bartman, and M. Titus, Rocket-grenade observations of atmospheric heating in the Arctic, *J. Geophys. Res.*, **64**, 1342–1343, 1959.
- Swenson, G.R., and S.B. Mende, OH emission and gravity waves (including a breaking wave) in all-sky imagery from Bear Lake, UT, *Geophys. Res. Lett.*, **21**, 2239–2242, 1994.
- Taylor, M.J., and M.A. Hapgood, Identification of a thunderstorm as a source of short period gravity waves in the upper atmospheric nightglow emissions, *Planet. Space Sci.*, **36**, 975–986, 1987.
- Taylor, M.J., E.H. Ryan, T.F. Tuan, and R. Edwards, Evidence of preferential directions for gravity wave propagation due to wind filtering in the middle atmosphere, *J. Geophys. Res.*, **98**, 6047–6057, 1993.
- Teitelbaum, H., F. Vial, A.H. Manson, R. Giraldez, and M. Massebeuf, Non-linear interaction between the diurnal and semidiurnal tides: Terdiurnal and diurnal secondary waves, *J. Atmos. Terr. Phys.*, **51**, 627–634, 1989.
- Tepley, C.A., Neutral winds of the middle atmosphere observed at Arecibo using a Doppler Rayleigh lidar, *J. Geophys. Res.*, **12**, 25,781–25,790, 1994.
- Tepley, C.A., S.I. Sargoytchev, and C.O. Hines, Initial Doppler Rayleigh lidar results from Arecibo, *Geophys. Res. Lett.*, **18**, 167–170, 1991.
- Theon, J.S., and W.S. Smith, Seasonal transitions in the thermal structure of the mesosphere at high latitudes, *J. Atmos. Sci.*, **27**, 173–176, 1970.
- Theon, J.S., W. Nordberg, L.B. Katchen, and J.J. Horvath, Some observations on the thermal behavior of the mesosphere, *J. Atmos. Sci.*, **24**, 428–438, 1967.
- Theon, J.S., W.S. Smith, J.F. Casey, and B.R. Kirkwood, The mean observed structure and circulation of the stratosphere and mesosphere, *NASA Tech. Rep.*, NASA TR-375, Mar, 1972.

- Tohatsu, T., *Compendium of Aeronomy*, 509 pp., Terra Scientific Publishing Company, Tokyo, 1990.
- Tsuda, T., S. Kato, A.H. Manaon, and C.E. Meek, Characteristics of semidiurnal tides observed by the Kyoto meteor radar and Saskatoon medium frequency radar, *J. Geophys. Res.*, **93**, 7027-7036, 1988.
- Tsuda, T., S. Kato, T. Yokoi, T. Inoue, M. Yamamoto, T.E. VanZandt, S. Fukao, and T. Sato, Gravity waves in the mesosphere observed with the middle and upper atmosphere radar, *Radio Sci.*, **26**, 1005-1018, 1990.
- Tsuda, T., Y. Murayama, T. Hakamura, R.A. Vincent, A.H. Manson, C.E. Meek, and R.L. Wilson, Variations of the gravity wave characteristics with height, season and latitude revealed by comparative observations, *J. Atmos. Terr. Phys.*, **51**, 555-568, 1994.
- Turnbull, D.N., and R.P. Lowe, New hydroxyl transition probabilities and their importance in airglow studies, *Planet. Space Sci.*, **37**, 723-738, 1989.
- U.S. Standard Atmosphere, U.S. Government Printing Office, Washington, D.C., 1976.
- Vadnais, C.M., Mesopause winds and OH intensities at mid-latitudes-Fabry-Perot Interferometer observations of the OH emission at 8430A from Bear Lake Observatory, M.S. Thesis, Utah State University, Logan, 1993.
- Veryard, R.G., and R.A. Ebdon, Fluctuations in tropical stratospheric winds, *Meteorol. Mag.*, **90**, 125-143, 1961.
- Vial, F., and J.M. Forbes, Recent progress in tidal modeling, *J. Atmos. Terr. Phys.*, **51**, 663-671, 1989.
- Vincent, R.A., Gravity wave motions in the mesosphere, *J. Atmos. Terr. Phys.*, **46**, 119-128, 1984.
- Vincent R.A., and D.C. Fritts, A climatology of gravity wave motions in the mesopause region at Adelaide, Australia, *J. Atmos. Sci.*, **44**, 748-760, 1987.
- Vincent, R.A., T. Tsuda, and S. Kato, Asymmetries in mesospheric tidal structure, *J. Atmos. Terr. Phys.*, **51**, 609-616, 1989.
- von Zahn, U., and W. Meyer, Mesopause temperatures in polar summer, *J. Geophys. Res.*, **94**, 14,647-14,651, 1989.
- Walterscheid, R.L., Inertio-gravity wave induced accelerations of mean flow having an imposed periodic component: Implications for tidal observations in the meteor region, *J. Geophys. Res.*, **86**, 9698-9706, 1981.
- Walterscheid, R.L., and G. Schubert, Nonlinear evolution of an upward propagating gravity wave: Overturning, convection, transience and turbulence, *J. Atmos. Sci.*, **47**, 101-125, 1990.
- Ward, W.E., and V.I. Formichev, On the role of atomic oxygen in the dynamics and every budget of the mesosphere and lower thermosphere, *Geophys. Res. Lett.*, **12**, 1199-1202, 1993.
- Weinstock, J., Nonlinear theory of gravity waves: Momentum deposition, generalized Rayleigh friction and diffusion, *J. Atmos. Sci.*, **39**, 1698-1710, 1982.
- Weinstock, J., Saturated and unsaturated spectra of gravity waves and scale dependent diffusion, *J. Atmos. Sci.*, **47**, 2211-2225, 1990.

- Westenberg, A.A., N. de Haas, and J.M. Roscoe, Radical reactions in electron spin resonance, *J. Phys. Chem.*, **74**, 3431-3438, 1970.
- Whiteway, J.A., Lidar observations of thermal structure and gravity wave activity in the middle atmosphere, Ph.D. thesis, York University, North York, Ontario, 1994.
- Whiteway, J.A., and A.I. Carswell, Lidar observations of gravity wave activity in the upper stratosphere over Toronto, *J. Geophys. Res.*, **100**, 14,113-14,124, 1995.
- Whiteway, J.A., A.I. Carswell, and W.E. Ward, Mesospheric temperature inversions with overlying nearly adiabatic lapse rate: An indication of a well-mixed turbulent layer, *Geophys. Res. Lett.* **22**, 1201-1204, 1995.
- Wickwar, V.B., K.C. Beissner, T.D. Wilkerson, S.C. Collins, J.M. Maloney, J.W. Meriwether, and X. Gao, Climatology of mesospheric temperature profiles observed with the Consortium Rayleigh-scatter lidar at Logan, Utah, in *Advances in Atmospheric Remote Sensing with Lidar*, edited by A. Ansmann, R. Neuber, P. Rairoux, and U. Wandinger, pp. 557-560, Springer-Verlag, Berlin, 1997a.
- Wickwar, V.B., I.K. Monson, C.M. Vadnais, and D. Rees, Wind climatology at 87 km derived from Fabry-Perot observations of the OH emission above Bear Lake Observatory, *J. Geophys. Res.*, to be submitted, 1997b.
- Wickwar, V.B., T.D. Wilkerson, J.W. Meriwether, and D. Rees, The Consortium Lidar: Results and Facilities Present and Planned, in *Optical Remote Sensing of the Atmosphere*, pp. 171-173, Salt Lake City, Utah, 1995.
- Wild, J.D., M.E. Gelman, A.J. Miller, M.L. Chanin, A. Hauchecorne, P. Keckhut, R. Farley, P.D. Dao, J.W. Meriwether, G.P. Gobbi, F. Congeduti, A. Adriani, I.S. McDermid, T.J. McGee, and E.F. Fishbein, Comparison of stratospheric temperatures from several lidars, using National Meteorological Center and microwave limb sounder data as transfer references, *J. Geophys. Res.*, **100**, 11,105-11,111, 1995.
- Wilson, R., M.L. Chanin, and A. Hauchecorne, Gravity waves in the middle atmosphere observed by Rayleigh lidar. 2. Climatology, *J. Geophys. Res.*, **96**, 5169-5183, 1991.
- Yu, J.R., and C.Y. She, Climatology of a midlatitude mesopause region observed by a lidar at Fort Collins, CO (40.6° N, 105° W), *J. Geophys. Res.*, **100**, 7441-7452, 1995.